4-9-2019

# Bubble Interactions at Multi-Fluid Interfaces

Travis S. Emery
tse8682@rit.edu

## Recommended Citation

Emery, Travis S., "Bubble Interactions at Multi-Fluid Interfaces" (2019). Thesis. Rochester Institute of Technology. Accessed from

R·I·T

# Bubble Interactions at Multi-Fluid Interfaces

by

Travis S. Emery

A dissertation submitted in partial fulfillment of the requirements
for the degree of Doctorate of Philosophy in Microsystems Engineering

Microsystems Engineering Program
Kate Gleason College of Engineering

Rochester Institute of Technology
Rochester, New York
April 9, 2019

# Bubble Interactions at Multi-Fluid Interfaces
by
Travis S. Emery

## Committee Approval:

We, the undersigned committee members, certify that we have advised and/or supervised the candidate on the work described in this dissertation. We further certify that we have reviewed the dissertation manuscript and approve it in partial fulfillment of the requirements of the degree of Doctor of Philosophy in Microsystems Engineering.

Dr. Satish G. Kandlikar Date
James E. Gleason Professor, Mechanical Engineering

Dr. Michael Schertzer Date
Assistant Professor, Mechanical Engineering

Dr. Kathleen Lamkin-Kennard Date
Associate Professor, Mechanical Engineering

Dr. Anju Gupta Date
Assistant Professor, Chemical Engineering

## Certified by:

Dr. Bruce Smith Date
Director, Microsystems Engineering Program

# Abstract

Kate Gleason College of Engineering
Rochester Institute of Technology

**Degree**: Doctor of Philosophy **Program**: Microsystems Engineering

**Authors Name:** Travis S. Emery **Advisors Name:** Dr. Satish G. Kandlikar

**Dissertation Title:** Bubble Interactions at Multi-Fluid Interfaces

Numerous industrial applications and environmental phenomena are centered around bubble interactions at multi-fluid interfaces. These applications range from metallurgical processing to direct contact evaporation and solid shell formation. Environmental phenomena, such as bubble collisions with the sea surface microlayer and the collision of liquid encapsulated bubbles, were also considered as motivators for this work. Although the associated flow dynamics are complex, they play a vital role in governing the related application outcome, be it in terms of mass or heat transfer efficiency, bubble shell production rate, chemical reaction rate, etc. For this reason, a fundamental understanding of the fluid dynamics involved in the bubble interactions are required to aid in optimal system design. In this work, rigorous experimental work was supplemented by in-depth theoretical analysis to unravel the physics behind these bubble interactions.

The focus of the present work is to develop an improved understanding of bubble interactions at liquid-liquid and compound interfaces. Extensive testing has been carried out to identify and classify flow regimes associated with single bubble and bubble stream passage through a liquid-liquid interface. Dimensionless numbers were identified and employed to map these regimes and identify transition criteria. The extension of one identified regime, bubble shell formation, to the field of direct contact evaporation was considered through the development of a numerical model to predict bubble growth in an immiscible liquid droplet. Additional dimensional analysis was carried out for the characterization of bubble collisions at solid and free surfaces. Previously developed numerical models were employed to form the relationship between the appropriate dimensionless groups capable of characterizing such collisions. This relationship was then used to describe a practical method for predicting the radial film size formed during the collision. Finally, three numerical models were developed to predict the bubble motion and the spatiotemporal evolution of the film(s) formed during the collision of a bubble with a liquid-liquid, solid-liquid-liquid, and gas-liquid-liquid interface. These models were validated through additional experiments carried out for this work as well as from data found in literature.

# Acknowledgements

First and foremost, I would like to acknowledge my advisor Dr. Satish Kandlikar. From the moment I began my work in the Thermal Analysis and Microfluidics Laboratory as an undergraduate student, Dr. Kandlikar has guided and pushed me to understand and achieve. He has helped further not only my technical understanding of the subject, but also my ability to present, communicate, and lead. I would also like to thank my committee members – Dr. Michael Schertzer, Dr. Kathleen Lamkin-Kennard, and Dr. Anju Gupta for their continued feedback and support. I would like to thank all my fellow lab members as well – Dr. Pruthvik Raghupathi, Dr. Arvind Jaikumar, Dr. Isaac Perez-Raya, Alyssa Recinella, Aranya Chauhan, Jose Luis Gonzalez Hernandez, and Aniket Rishi for their continued support and efforts to help me learn and improve. Finally, I would like to thank all of my family and friends for always supporting and showing interest in my work. I would most certainly not have made it to where I am today without your unconditional love and encouragement.

# Contents

# List of Figures

# List of Tables

# Nomenclature

| Symbol | Description | Units/Value |
|---|---|---|
| $F_B$ | Buoyancy force | N |
| $F_D$ | Drag force | N |
| $F_H$ | History or Basset force | N |
| $F_A$ | Added mass force | N |
| $F_F$ | Film force | N |
| $Bo$ | Bond number | - |
| $Mo$ | Morton number | - |
| $We$ | Weber number | - |
| $Ca$ | Capillary number | - |
| $Oh$ | Ohnesorge number | - |
| $La$ | Laplace number | - |
| $Ar$ | Archimedes number | - |
| $Re$ | Reynolds number | - |
| $Fr$ | Froude number | - |
| $D$ | Bubble or droplet diameter – subscript $h$ or $v$ for horizontal or vertical | m |
| $R$ | Bubble or droplet radius | m |
| $V$ | Velocity | m/s |
| $g$ | Gravitational acceleration | $m/s^2$ |
| $h$ | Film thickness – subscript for associated layer | m |
| $p$ | Pressure – subscript for associated layer | Pa |
| $r$ | Radial direction | m |

| | | |
|---|---|---|
| $z$ | Axial direction | m |
| $t$ | Time | s |
| $V_r$ | Radial velocity | m/s |
| $V_z$ | Axial velocity | m/s |
| $p_0$ | Nominal bulk pressure | Pa |
| $R_F$ | Film radius | m |
| $\Delta p$ | Excess film pressure | Pa |
| $V_g^*$ | Bubble volume required for passage | $m^3$ |
| $z^*$ | Dimensionless bubble displacement | - |
| $h^*$ | Dimensionless film thickness | - |
| $t^*$ | Dimensionless time | - |
| $S_i$ | Spreading coefficient – subscript *A*, *B*, *G* for dispersed, continuous, or gas phase respectively | N/m |
| $Nu$ | Nusselt number | - |
| $Pe$ | Peclet number | - |
| $Ja$ | Jakob number | - |
| $V_T$ | Terminal velocity | m/s |
| $C_D$ | Drag coefficient | - |
| $y$ | Vertical bubble position | m |
| $\Delta t$ | Time between frames | s |
| SO | Silicone oil | - |
| $a$ | Drop apex radius of curvature | m |
| $x^*$ | Dimensionless drop profile x coordinate | - |
| $y^*$ | Dimensionless drop profile y coordinate | - |

| | | |
|---|---|---|
| $C_m$ | Added mass coefficient | - |
| $KE$ | Kinetic energy | J |
| $SE$ | Excess surface energy | J |
| $R_F^*$ | Dimensionless film radius | - |
| $\Delta p^*$ | Dimensionless excess film pressure | - |
| $V_s$ | Superficial velocity | m/s |
| $f$ | Frequency | $s^{-1}$ |
| $Fr^*$ | Modified Froude number | - |
| $S$ | Top liquid height | m |
| $R_1$ | Liquid-vapor interface location | m |
| $R_2$ | Liquid-liquid interface location | m |
| $k$ | Thermal conductivity – subscript denotes associated liquid | W/m·K |
| $T_{sat}$ | Saturation temperature | °C |
| $v$ | radial velocity | m/s |
| $T$ | Liquid temperature – subscript denotes associated liquid | °C |
| $h_{fg}$ | Latent heat of vaporization | J/kg |
| $C_{p,1}$ | Specific heat of volatile liquid | J/kg·K |
| $\bar{R}_1$ | Dimensionless liquid-vapor interface location | - |
| $\bar{R}_2$ | Dimensionless liquid-liquid interface location | - |
| $\bar{r}$ | Dimensionless radial coordinate | - |
| $\bar{T}$ | Dimensionless liquid temperature – subscript denotes associated liquid | - |
| $R_{1,0}$ | Initial vapor core radius | m |
| $R_{2,0}$ | Initial drop radius | m |

| | | |
|---|---|---|
| $\bar{R}_{1,0}$ | Dimensionless initial vapor core radius | - |
| $\bar{R}_{2,0}$ | Dimensionless initial drop radius | - |
| $T_0$ | Initial subcooled temperature | °C |
| $T_S$ | Required superheat for bubble nucleation | °C |
| $T_\infty$ | Bulk liquid temperature | °C |
| $\bar{T}_s$ | Dimensionless superheat required for bubble nucleation | - |
| $\Delta T$ | Liquid superheat | °C |
| $\overline{h_0}$ | Dimensionless initial shell thickness | - |
| $L$ | Distance between needle or capillary and interface | m |
| $\Delta C_D^*$ | Normalized drag coefficient | - |
| $z_S$ | Free surface deformation | m |
| $r_m$ | Outer radial boundary | m |
| $V_{imp}$ | Impact velocity | m/s |
| $z_I$ | Liquid-liquid interface deformation | m |
| $z_b$ | Bubble surface deformation | m |
| $h_{00}$ | Initial distance between top of bubble and interface | m |
| $F_I$ | Interface force | N |
| $H_1$ | Top film thickness at axis of symmetry | m |
| $H_2$ | Bottom film thickness at axis of symmetry | m |
| $h_{1,0}$ | Initial top film thickness | m |
| $h_{2,00}$ | Initial distance between top of bubble and interface | m |
| $F_S$ | Surface force | N |

## Greek Letters

| | | |
|---|---|---|
| $\rho$ | Density – subscript denotes associated liquid or vapor | kg/m$^3$ |
| $\mu$ | Viscosity – subscript denotes associated liquid | Pa·s |
| $\sigma$ | Surface tension – subscript denotes associated liquid | N/m |
| $\sigma_I$ | Interfacial tension | N/m |
| $\Pi$ | Disjoining pressure | Pa |
| $\theta$ | Opening angle | ° |
| $\varphi$ | Tangent angle to drop profile | ° |
| $\omega$ | Shape factor | - |
| $\Gamma$ | Normalized density difference | - |
| $\alpha$ | Thermal diffusivity – subscript denotes associated liquid | m$^2$/s |
| $\varepsilon$ | Normalized vapor density ratio, $\varepsilon=1-\rho_{v}/\rho_1$ | - |
| $\eta$ | Dimensionless bubble growth coordinate | - |
| $\tau$ | Dimensionless time | - |
| $\gamma$ | Thermal diffusivity ratio | - |
| $\zeta$ | Thermal conductivity ratio | - |
| $\psi$ | Normalized distance between bubble and solid surface | - |
| $\chi$ | Bubble aspect ratio | - |
| $\tau_{v,T}$ | Normal viscous stress | Pa |
| $\bar{\sigma}$ | $1/\bar{\sigma} = (1/\sigma_I + 1/\sigma_B)$ | N/m |
| $\lambda_I$ | $\lambda_I = \sqrt{\sigma_I/\Delta\rho g}$ | m |
| $\lambda_T$ | $\lambda_T = \sqrt{\sigma_T/\rho_T g}$ | m |
| $\gamma_E$ | Euler constant | - |
| $\sigma'$ | $1/\sigma' = (1/\sigma_I + 1/\sigma_T)$ | N/m |

## Chapter 1

# 1 Introduction

The motion of bubbles in a liquid medium has captured the attention of scientists and researchers for centuries. Leonardo da Vinci was perhaps the first to scientifically investigate and report on the failure of large bubbles to follow a rectilinear rise path; this finding was later dubbed Leonardo's paradox [1]. It wasn't until several centuries after his death that the mystery was solved, and the phenomenon was determined to be a result of wake instabilities. In the early 19th century, Thomas Young introduced the concept of surface tension in his qualitative studies on the shape of fluid-fluid interfaces under capillary forces [2]. A year later, Pierre-Simon Laplace gave Young's qualitative theory a mathematical description, and the well-known Young-Laplace equation was derived [3]. Later that same century, Osborne Reynolds analyzed fluid flow in thin films, which resulted in the lubrication equations that are still used extensively today [4]. In more recent years, technological advances have allowed us to explore many of the underlying physics associated with bubble motion and bubble interactions with other surfaces in a liquid medium. Despite the centuries worth of research, many complexities associated with bubble interactions still remain a mystery. The focus of this dissertation is to broach these topics and develop an improved understanding of bubble interactions at multi-fluid interfaces.

### 1.1 The Bubble Collision Process

A brief overview of a bubble's collision with a liquid-liquid interface is presented in this section. Consider first, two immiscible liquids of different densities in stratified layers with the heavier liquid being the bottom layer as shown in Figure 1(a). When a bubble is introduced into the bottom liquid, the density difference between the gas within the bubble

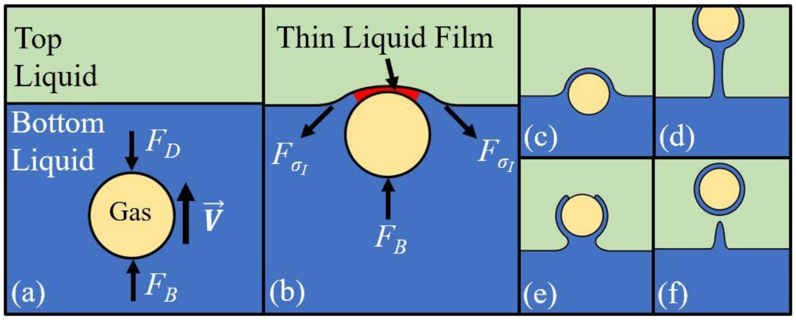

**Figure 1.** *(a) Bubble rise and (b) impact with a liquid-liquid interface with (c)-(f) possible collision outcomes.*

and the surrounding liquid induces a constant buoyancy force ($F_B$) causing it to rise. The bubble will accelerate upwards until the growing drag force ($F_D$) balances out the buoyancy force. During its acceleration, the drag force requires some time to establish itself; this results in a history force ($F_H$), also known as the Basset force [5]. This history force can be neglected when the bubble surface is considered mobile but must be taken into account for immobile bubble surface conditions [6]. Additionally, when the bubble undergoes any sort of acceleration, the surrounding liquid must also accelerate with it, giving rise to an added mass force ($F_A$). Eventually, the bubble will impact the horizontal interface between the liquid layers. When the bubble collides with the interface, interfacial tension resists the bubble motion and a thin liquid film is formed between the bubble and the interface, as shown in Figure 1(b). The pressure in this film increases during the impact and imparts a film force ($F_F$) onto the bubble. If the film is very thin, surface forces due to van der Waals and electrical double layer interactions also become important. Typically, a film thickness of ~100 nm or less is required before these surface forces need to be taken into account [7]. For bubble collisions with very low Reynolds numbers (Re$\ll$1), such film thicknesses are routinely achieved during the collisions, and these forces take on an important role in the film thinning process [8]. However, during dynamic (Re$\gg$1) bubble collisions, the film thickness is on the order of micrometers, and therefore, these surface forces can be neglected [9]. At this point in the collision process, there are a number of different variations. The bubble may become trapped at the interface, Figure 1(c), or pass through the interface with some volume of the bottom liquid entrained around and/or behind the bubble, Figure 1(d)-(f). A similar process is seen in bubble-free surface collisions in which the outcome is determined based on two competing processes: (i) the thinning of the liquid between the bubble and interface, and (ii) the expense of the kinetic energy to increase the free energy of the system via an increase in bubble surface area due to deformation [10]. For bubble passage through a liquid-liquid interface, more significant degrees of interface deformation are commonly seen; thus, the kinetic to free surface energy transfer would also stem from increased interfacial area between the liquids. The thinning rate of the liquid column entrained behind the bubble also plays a significant role in determining the outcome.

Thin film formation is also seen with bubble and droplet collisions with a free surface, a solid surface, or another bubble or droplet, as well as solid particle collisions with a liquid-liquid interface or free surface. Some of these scenarios are shown in Figure 2 [11]. In any of these cases, the hydrodynamics of the liquid film play a dominant role in dictating the collision process. Lubrication theory is customarily used to define the thinning rate of

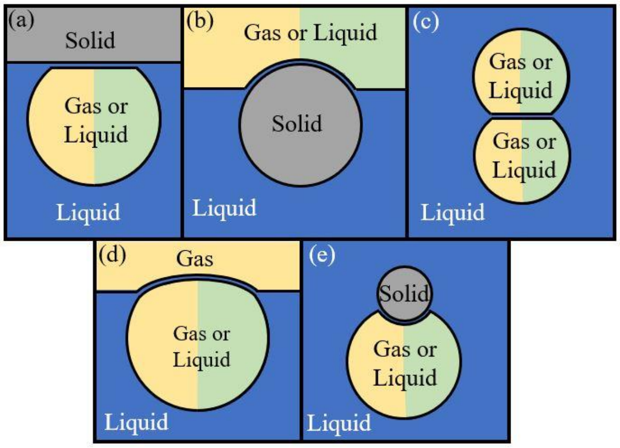

**Figure 2.** *Formation of thin liquid films in various scenarios. Redrawn from [11].*

the film regardless of its formation method. As such, a significant amount of research has focused on details of the thinning process. A more in-depth review of the related theory is discussed in Section 2.1.

The interaction of a stream of bubbles with a liquid-liquid interface adds significant complexity to the process compared to single bubble interactions. In addition to liquid properties, bubble size, and bubble velocity, the frequency with which the bubbles impact the interface becomes a significant parameter. As will be discussed in Section 4.1.2, the variation in possible outcomes for bubble streams also increases. The general outline of the collision process begins in a manner similar to single bubble passage with a continuous stream of bubbles rising through the bottom liquid. In this scenario, however, the collision outcome of each bubble will be dependent on the collision outcome of the preceding bubble(s). At very low frequency, the preceding bubble may have already passed through the interface, and the process would be the same as single bubble passage. At intermediate frequencies, multiple bubbles may reach the interface simultaneously and pass through as a group. At yet higher frequencies, columns of the bottom liquid may begin to be formed. In these scenarios, multiple thin liquid films may exist between the bubbles and the interface as well as between the bubbles themselves if they are in contact. This configuration has received significantly less research focus compared to single bubble passage, and as a result, the exact criteria for the formation of these flow patterns has not been previously explored.

A new focus area recently introduced to this field encompasses bubble collisions at so-called “compound interfaces”. A compound interface is classified here by the presence of a thin layer of a secondary liquid above the bulk liquid. On the top side of the thin layer may be a solid surface or a free surface, as shown in Figure 3(a) and (b). These compound interfaces will be referred to as solid-liquid-liquid and gas-liquid-liquid interfaces throughout the dissertation. The forces acting on the bubble during its collision with a compound interface would remain the same as compared to a liquid-liquid interface collision. In such a system, two thin liquid films would be formed during the collision: one made up of the bulk liquid and the other made up of the secondary liquid. These systems have received very little research exposure but have wide spread implications, as discussed in Section 1.3.4.

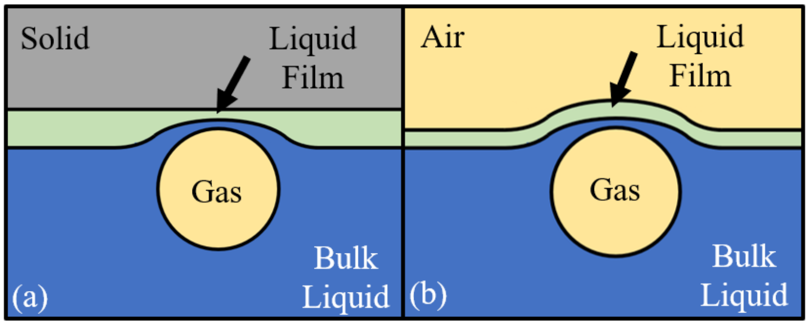

**Figure 3.** *Bubble collision at two types of compound interfaces: (a) solid-liquid-liquid, and (b) gas-liquid-liquid.*

## 1.2 Relevant Dimensionless Numbers

Dimensionless numbers provide a powerful tool in elucidating the dominant underlying mechanisms in complex processes. The prominent forces during bubble collisions with a liquid-liquid interface include buoyancy, viscous forces, surface tension, and inertia. Comparing the relative magnitude of these forces leads to several dimensionless numbers, which are shown in Table 1 along with other relevant dimensionless numbers commonly used in fluid mechanics. Since the system currently being studied involves two liquids, the dimensionless numbers must specify which liquid properties are being used. These are herein defined as the “bottom” or “top” dimensionless numbers with bottom referring to the properties of the denser liquid and top referring to the properties of the less dense liquid.

Additionally, the interfacial tension, a crucial parameter required to define the system, needs to be included in these dimensionless numbers. To this extent, “interfacial” dimensionless numbers are defined as those using interfacial tension instead of the associated liquid surface tension. For example, the “bottom Bond number” would employ the bottom liquid density and surface tension, while the “bottom interfacial Bond number” would utilize the bottom liquid density and interfacial tension. All quantities in Table 1 are defined in this manner.

**Table 1.** *Relevant dimensionless numbers and their associated meaning.*

| **Name** | **General Definition** | **Physical Meaning** | **Modified Dimensionless Numbers for a Two-liquid System** | | | |
|---|---|---|---|---|---|---|
| | | | **Top** | **Bottom** | **Top Interfacial** | **Bottom Interfacial** |
| Bond Number | $Bo = \frac{\rho g D^2}{\sigma}$ | Buoyancy vs. surface tension force | $Bo_\mathrm{T} = \frac{\rho_\mathrm{T} g D^2}{\sigma_T}$ | $Bo_\mathrm{B} = \frac{\rho_B g D^2}{\sigma_B}$ | $Bo_{\mathrm{I,T}} = \frac{\rho_\mathrm{T} g D^2}{\sigma_I}$ | $Bo_{\mathrm{I},B} = \frac{\rho_B g D^2}{\sigma_I}$ |
| Morton Number | $Mo = \frac{g\mu^4}{\rho\sigma^3}$ | Characterize bubble shape | $Mo_\mathrm{T} = \frac{g\mu_T^4}{\rho_\mathrm{T}\sigma_T^3}$ | $Mo_B = \frac{g\mu_B^4}{\rho_\mathrm{B}\sigma_B^3}$ | $Mo_{\mathrm{I,T}} = \frac{g\mu_T^4}{\rho_\mathrm{T}\sigma_I^3}$ | $Mo_{\mathrm{I},B} = \frac{g\mu_B^4}{\rho_\mathrm{B}\sigma_I^3}$ |
| Weber Number | $We = \frac{\rho V^2 D}{\sigma}$ | Inertia vs. surface tension force | $We_\mathrm{T} = \frac{\rho_\mathrm{T} V^2 D}{\sigma_T}$ | $We_B = \frac{\rho_\mathrm{B} V^2 D}{\sigma_B}$ | $We_{\mathrm{I,T}} = \frac{\rho_\mathrm{T} V^2 D}{\sigma_I}$ | $We_{\mathrm{I},B} = \frac{\rho_\mathrm{B} V^2 D}{\sigma_I}$ |
| Capillary Number | $Ca = \frac{\mu V}{\sigma}$ | Viscous vs. surface tension force | $Ca_T = \frac{\mu_T V}{\sigma_T}$ | $Ca_B = \frac{\mu_B V}{\sigma_B}$ | $Ca_{I,T} = \frac{\mu_T V}{\sigma_I}$ | $Ca_{I,B} = \frac{\mu_B V}{\sigma_I}$ |
| Ohnesorge Number | $Oh = \frac{\mu}{\sqrt{\rho\sigma D}}$ | Viscous vs. inertial & surface tension force | $Oh_T = \frac{\mu_T}{\sqrt{\rho_T\sigma_T D}}$ | $Oh_B = \frac{\mu_B}{\sqrt{\rho_B\sigma_B D}}$ | $Oh_{I,T} = \frac{\mu_T}{\sqrt{\rho_T\sigma_I D}}$ | $Oh_{I,B} = \frac{\mu_B}{\sqrt{\rho_B\sigma_I D}}$ |
| Laplace Number | $La = \frac{\rho\sigma D}{\mu^2}$ | Surface tension & inertia vs. viscous force | $La_T = \frac{\rho_T\sigma_T D}{\mu_T^2}$ | $La_B = \frac{\rho_B\sigma_B D}{\mu_B^2}$ | $La_{I,T} = \frac{\rho_T\sigma_I D}{\mu_T^2}$ | $La_B = \frac{\rho_B\sigma_I D}{\mu_B^2}$ |
| Archimedes Number | $Ar = \frac{\rho\sqrt{gD^3}}{\mu}$ | Buoyancy vs. viscous force | $Ar_T = \frac{\rho_T\sqrt{gD^3}}{\mu_T}$ | $Ar_B = \frac{\rho_B\sqrt{gD^3}}{\mu_B}$ | - | - |
| Reynolds Number | $Re = \frac{\rho V D}{\mu}$ | Inertial vs. viscous force | $Re_T = \frac{\rho_T V D}{\mu_T}$ | $Re_B = \frac{\rho_B V D}{\mu_B}$ | - | - |
| Froude Number | $Fr = \frac{V}{\sqrt{gD}}$ | Inertial vs. gravity force | - | - | - | - |

## 1.3 Applications

Bubble interactions with a liquid-liquid interface have been studied due to their relevance in numerous industrial applications such as metallurgy [12–16], direct contact evaporation [17], nuclear reactor safety [18], and liquid-liquid extraction [19,20], as well as environmental phenomena such as the ascent of plumes through the Earth’s mantle [21]. In such applications, mass or heat transfer between stratified liquid layers is often the primary goal. In order to improve the efficiency of the mass or heat transfer processes across the interface, it is desirable to increase the effective contact area between the liquids. A relatively simple method commonly employed is the bubbling of gas through the stratified liquid layers. Another application of bubble passage through a liquid-liquid interface is for the production of spherical shells [22], as discussed in further detail in Section 1.3.2. In any of these applications, the outcome of the bubble collision dictates the efficiency of the process. Compound interfaces are reminiscent of numerous systems found in nature, as well as double emulsion collisions, as outlined in Section 1.3.4. There are a number of parameters that can affect these systems, including the properties of the two liquids, specifically the densities, viscosities, and surface tensions, as well as the bubble size, shape, and impact velocity.

### *1.3.1 Metallurgical Relevance*

A significant amount of previous work on bubble passage through a liquid-liquid interface has been performed in association with its relevance to metallurgical processing such as secondary refining, copper conversion, and gas stirred ladling [12–16,23–29]. In such processes, molten metal and molten slag form two stratified liquid layers. A chemical reaction takes place at the interface to induce various results such as decarburization, dephosphorization, and desiliconization [16]. Mixing of the two liquids is required to increase the efficiency of the chemical process. Due to the high temperatures, this is commonly done through gas injection, as shown in Figure 4. The entrainment of molten metal across the interface increases the effective contact surface area over which the chemical reaction may occur [29]. Therefore, the behavior of the gas bubbles as they pass through the liquid-liquid interface is directly associated with the overall reaction rate [16].

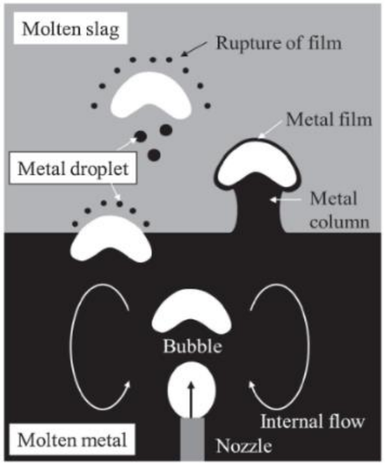

**Figure 4.** *Bubble passage through molten metal and slag commonly seen in metallurgy [16].*

### *1.3.2 Applications of Spherical Shells*

One possible outcome of a bubble collision with a liquid-liquid interface is the formation of a shell of the lower liquid around the bubble as it leaves the interface [22,30–35]. Solidification of this shell as it continues to rise through the top liquid enables the production of spherical metallic shells that can contain various gases. Kawano et al. [22] have demonstrated the feasibility of generating these shell using the system shown in Figure 5. As described by Lee et al. [36], the applications of these bubble shells is widespread. Aluminum shells would burn more smoothly than flakes or powders when utilized in an oxidizer as a high-performance solid fuel. Metallic shells filled with a paraffin which melts near body temperature could be used as insulation in space garments for extravehicular activity. Other potential uses include shock-absorbing armor plates, pharmaceuticals, catalytic reagents, and fire retardants. Although these shells have previously been made using annular nozzles, the apparatus required for solidification of the shells is very large [22]. Instead, the use of a simple system in which the shells are formed via bubble passage through a liquid-liquid interface could simplify this production process.

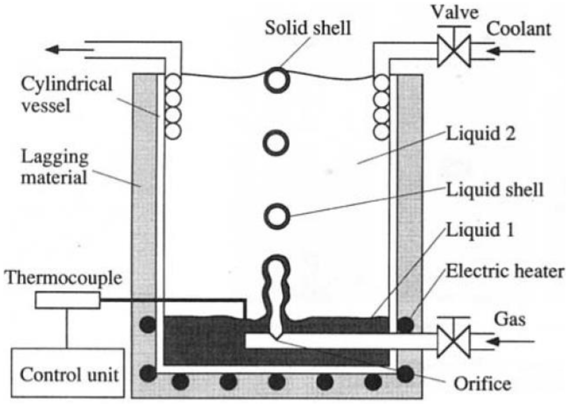

**Figure 5.** *Apparatus used by Kawano et al. [22] for production of solid spherical shells.*

### *1.3.3 Direct Contact Evaporation*

A specific motivation behind the present work is the application of the bubble collision process to direct contact evaporation. In surface type heat exchangers, such as the commonly used shell and tube type, heat is transferred through a metallic barrier present between two liquids. The mere presence of this barrier introduces a number of issues. The solid barrier lowers the heat transfer rate, and is exposed to fouling, corrosion, and thermal stresses [37]. Some of these issues may be overcome with the use of specialized materials or additives, but their use further raises the material costs associated with these heat exchangers. The operational cost for these systems is high due to continuous maintenance and the associated fouling and corrosion as well [37]. Direct contact heat exchangers eliminate the need for a metallic barrier by bringing the two liquid streams into direct physical contact. This increases the associated heat transfer coefficients and reduces material and operational costs [37]. However, the system does require the two liquids to be at the same pressure, and they must be immiscible [37]. These systems have broad industrial applications such as water desalination, solar energy applications, and power production from low-grade energy resources, such as geothermal energy. While each of these applications hold substantial worth of their own, their combined importance further motivates research efforts in the field of direct contact evaporation.

A setup commonly employed for direct contact heat transfer is the spray column evaporator. In these systems, droplets of a volatile lighter liquid are typically injected into the bottom of a container while a heavier bulk liquid is introduced from the top to create a counter-current spray column, such as that shown in Figure 6 [38]. Evaporation of the droplets results in a net cooling effect on the bulk liquid. To induce evaporation of the volatile liquid droplets, the bulk liquid must be at a temperature above the saturation temperature of the volatile liquid. The excess temperature above the saturation temperature is commonly referred to as the superheat [38]. In pure liquid, the degree of superheat required to induce nucleation can be significant [39]. A number of analytical and experimental studies have been carried out investigating various aspects of these systems,

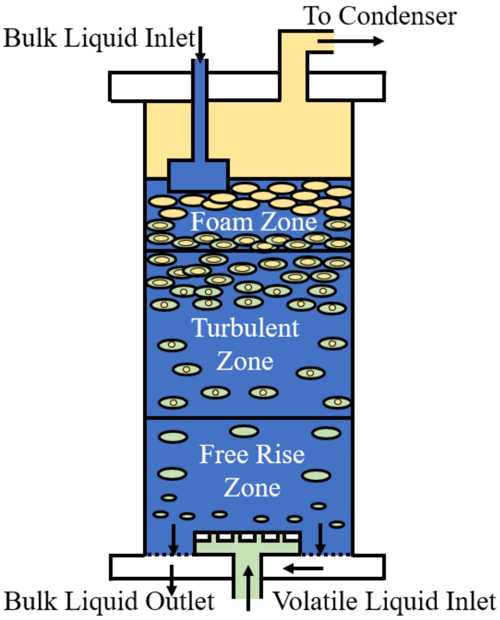

**Figure 6.** *Schematic of typical spray column evaporator. Redrawn from [38].*

such as the influence of initial droplet size, liquid flow rates, and column height [38,40,41]. Some theoretical models for bubble growth have also been proposed, as discussed in Section 2.3.

Although current direct contact evaporators typically inject droplets of a volatile liquid into an immiscible bulk liquid [31,42], the use of pre-nucleated droplets have been hypothesized to further improve the heat transfer performance. The present work on bubble passage through a liquid-liquid interface presents one method of producing such pre-nucleated droplets, as shown in Figure 1(f). Since the vapor core would already be established, the degree of superheat required to induce boiling would be very small, thus improving the efficiency of the direct contact evaporation systems. However, due in part to the relatively limited understanding currently available for the formation of these bubble shells via bubble passage through a liquid-liquid interface, this method has not yet been implemented for this purpose.

### *1.3.4 Applications of Compound Interfaces*

Recently, bubble bursting at an air/oil/water-with-surfactant compound interface was utilized as a means of dispersing sub-micrometer oil droplets into the water to create nanoemulsions, as shown in Figure 7 [43,44]. These functional nanoemulsions are of interest to a number of different applications such as drug delivery, material science, functional foods, and nutraceuticals. This simple technique offers a low-cost and energy-efficient platform to produce nanoemulsions that was not previously available. Furthermore, this technique is scalable and has the ability to produce nanoemulsions in large volumes. Another interest area related to compound interfaces is the sea surface microlayer. The atmosphere/ocean interface is covered by an organic film made up of lipids, proteins, and hydrocarbons [45]. Therefore, when a bubble collides with the ocean surface, it actually interacts with a compound interface made up of the ocean water and this microlayer. Lastly, the collision of liquid-encapsulated bubbles (the same as those previously mentioned for spherical shell production and direct contact evaporation) with other bubbles or interfaces is considered. Most bubbles formed in nature are, in fact, coated with an organic oil layer roughly 1-100 μm thick [46]. When these encapsulated bubbles collide, a compound interface is formed which will significantly alter the film drainage dynamics as compared to the collision of bare bubbles.

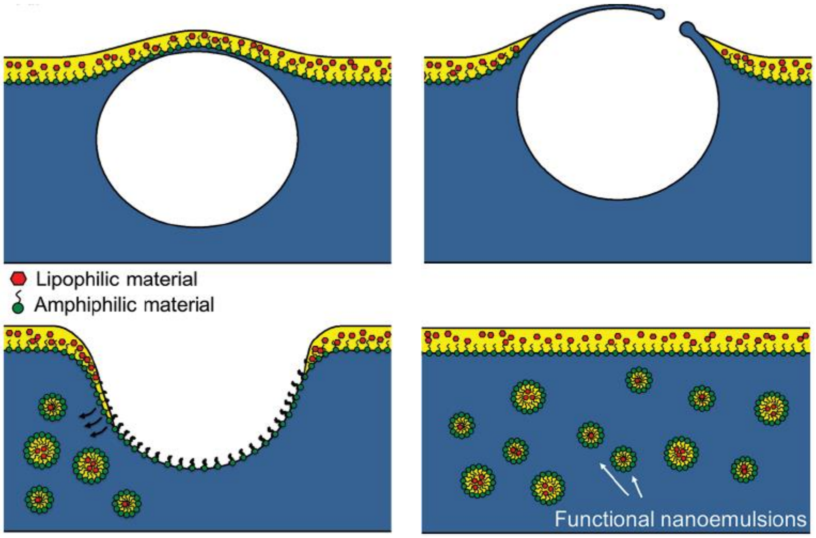

**Figure 7.** *Schematic of bubble bursting at a compound interface to generate functional nanoemulsions [44].*

## 1.4 Dissertation Structure

The dissertation is structured as follows:

*<u>Chapter 1: Introduction</u>* – An overview of the bubble collision process is given along with the dimensionless numbers used to describe such systems and relevant applications.

*<u>Chapter 2: Background</u>* – In this section, relevant literature related to bubble collisions and direct contact heat transfer is reviewed. This includes thin liquid film hydrodynamics, bubble passage through a liquid-liquid interface, and immiscible bubble growth.

*Chapter 3: Approach* – Details of the experimental setup are described here. The procedure during testing as well as the analysis is also presented.

*Chapter 4: Results and Discussion* – The results are divided into four main section: (i) flow regimes and transition criteria during bubble passage through a liquid-liquid interface, (ii) bubble growth in an immiscible liquid droplet, (iii) dimensionless characterization of bubble collisions, and (iv) modeling bubble collisions at liquid-liquid and compound interfaces.

*Chapter 5: Summary and Future Recommendation* – This section highlights the key contributions made by this work. Recommendations for extensions of this work in the future are also presented.

*Chapter 6: References* – Sources used throughout the dissertation are listed.

*Chapter 7: Appendix* – Additional information regarding Matlab code written for the dissertation is given.

# Chapter 2

# 2 Background

## 2.1 Theory of Thin Liquid Film Hydrodynamics

The drainage and thinning of the liquid film formed between a bubble and an interface during collision plays a crucial role in dictating the collision process. A significant focal point of previous research has concentrated on deriving theory to describe important characteristics of the film, such as the thinning rate, radial film size, and critical rupture thickness. The most general case may be thought of as two fluid drops colliding under an applied external force in a surrounding liquid medium as shown in Figure 8 [47]. It is typically assumed that the film is axisymmetric about the vertical axis of the bubble and the pressure in the film does not vary across its thickness. This enables the film thickness and pressure to be written as functions of only radial location, *r*, and time, *t*. The augmented Young-Laplace equation is used to define the pressure buildup within the film, while the Stokes-Reynolds equation, defined from lubrication theory, is applied to describe the thinning rate. The specific solution to this set of equations will vary depending on the boundary conditions applied. The theory is applicable to both bubble and droplet collisions.

The augmented Young-Laplace equation may be derived either through a balance of normal forces against surface tension forces on a surface element of a bubble, or by

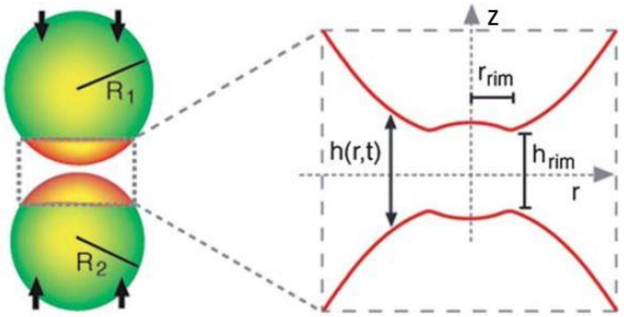

**Figure 8.** *Schematic of bubble or drop collision [47].*

minimizing the Helmholtz surface free energy of the system [47,48]. Although the lengthy derivation is not included in full, the linearized equation for the general case of two bubbles colliding is given as:

$$\frac{1}{2}\frac{\bar{\sigma}}{r}\frac{\partial}{\partial r}\left(r\frac{\partial h}{\partial r}\right) = \frac{2\bar{\sigma}}{\bar{R}} - \Pi - p \tag{1}$$

$$\text{where} \quad \frac{1}{\bar{R}} = \frac{1}{2}\left(\frac{1}{R_1} + \frac{1}{R_2}\right) \quad \text{and} \quad \frac{1}{\bar{\sigma}} = \frac{1}{2}\left(\frac{1}{\sigma_1} + \frac{1}{\sigma_2}\right)$$

where $\sigma$ is the surface tension, $R$ is the bubble radius with subscripts 1 or 2 corresponding to the respective bubble (see Figure 8), $h$ is the film thickness, $\Pi$ is the disjoining pressure, and $p$ is the hydrodynamic pressure in the film. The disjoining pressure is defined using DLVO theory, developed by Derjaguin and Landau [49], and Verwey and Overbeek [50], which incorporates the effects of van der Waals forces and electrostatic double layer interactions. These forces only become relevant when the film has reached very small thicknesses, ~100 nm, which are much thinner than those typically seen in dynamic bubble collisions, ~5 μm, until just before film rupture [7,9,51–53]. As such, they will not be a focal point of the present background review.

It is typically assumed that since the film thickness is much less than the radial size of the film, the application of Reynolds lubrication theory is appropriate [4]. Through dimensional analysis, it can be shown that the pressure variation across the film thickness is negligibly small, and the radial velocity is dominant. With the previous axisymmetric assumption, the Stokes equation describing the radial film flow may be written as:

$$\frac{\partial p}{\partial r} = \mu\frac{\partial^2 V_r}{\partial z^2} \tag{2}$$

where $\mu$ is the viscosity of the liquid in the film, and $V_r$ is the radial velocity. The continuity equation can also be written in cylindrical coordinates as:

$$\frac{1}{r}\frac{\partial}{\partial r}(rV_r) + \frac{\partial V_z}{\partial z} = 0 \tag{3}$$

where $V_z$ is the axial velocity. Equation 2 may be integrated twice with respect to $z$ and the appropriate boundary conditions must be applied to obtain the radial velocity profile. Substituting this profile into the continuity equation and integrating from $z=0$ to $h$ yields the film thinning rate. If tangentially immobile interfaces are assumed, the thinning rate may be written as:

$$\frac{\partial h}{\partial t} = \frac{1}{12\mu r}\frac{\partial}{\partial r}\left(rh^3\frac{\partial p}{\partial r}\right) \tag{4}$$

If one of the surface is instead assumed to have a zero shear stress condition, the 12 in the denominator of should be replaced with a 3. This equation, along with the Young-Laplace equation, gives a complete description of the spatial and temporal evolution of the thin liquid film.

A number of flat film models, which assume film thickness to be only a function of time, have also been derived to reach a simple closed form solution for the film thinning rate. Much of these stem from the work of Reynolds [4], who considered the approach of two flat parallel plates. Scheludko [54] was the first to apply this to the thinning of microscopic circular films. Equation 4 is integrated twice in the radial dimension to yield a function for the pressure. Assuming immobile surfaces, this is given as:

$$p = p_0 - \frac{3\mu r^2}{h^3}\frac{dh}{dt} \tag{5}$$

where $p_0$ is the pressure at the film's rim. The film force is then equated to the force pressing the surfaces of the film together:

$$\pi R_F^2 \Delta p = \int_0^{R_F} 2\pi r(p - p_0)dr = -\frac{3\pi\mu R_F^4}{2h^3}\frac{dh}{dt} \tag{6}$$

where $R_F$ is the radial film size, and $\Delta p=2\sigma/R-\Pi$ is the excess pressure in the film. The final thinning rate equation is thus given as:

$$-\frac{dh}{dt}=\frac{2h^3\Delta p}{3\mu R_F^2} \tag{7}$$

While this does present a simple closed form solution, the model makes several restricting assumptions: (i) viscosity in the film is equal to that in the bulk, (ii) negligible evaporation, (iii) flow between parallel flat surfaces, and (iv) tangentially immobile surfaces [52]. A number of increasingly complex theoretical extensions have been made to include the effect of thickness non-homogeneities and the tangential mobility of the surfaces [52,55–57]. However, it has been noted that even these more complex models fail to reach quantitative agreement with experimental results [47,48].

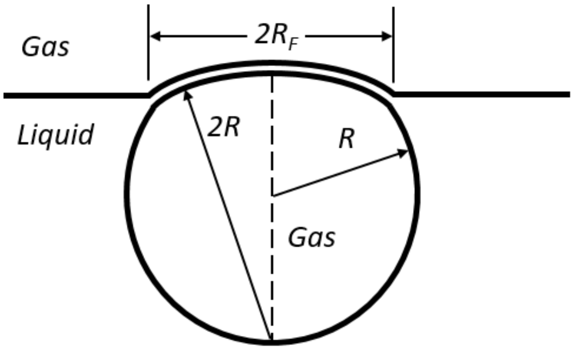

**Figure 9.** *Bubble resting at a deformable interface. Redrawn from [60].*

These flat film models also require a known radial film size, $R_F$, as demonstrated by Equation 7. Nicolson [58] considered a single bubble at rest on a horizontal surface consisting of two parts, as shown in Figure 9, which was later given theoretical justification by Chappelear [59]. Princen [60] used this model to predict the film radius, $R_F$, as a function of the bubble size and fluid properties. Although buoyancy had originally been considered the driving force to induce film drainage, this was later generalized as a driving force, $F$, by Ivanov et al. [11,61]. Quite simply, this model consists of a force balance in the vertical direction between the driving force and film pressure. The following equation is obtained for film radius of a bubble at a deformable interface:

$$R_F^2 = \frac{FR}{\pi\sigma} \tag{8}$$

For a bubble at a solid surface, the right side is multiplied by 0.5. More recently, Zawala et al. [62] used Equation 8 to predict the film radius for dynamic bubble collisions with a free surface. They estimate the driving force using the bubble kinetic energy and the change in vertical bubble diameter. Unfortunately, this method predicted film radii that were over two times the bubble radius in some cases. As noted by the authors, the numerical values should be treated with caution, but the important trends seen relating film size and bubble kinetics remain valid.

## 2.2 Bubble Passage through a Liquid-Liquid Interface

A number of studies have focused on fluid dynamics of single bubble passage through a liquid-liquid interface. Some researchers have focused on formation and characterization of bubble shells [22,30–35,63], while others only consider an entrained volume in the form of droplets created behind the rising bubble [12–15,20,64]. Their efforts were mainly empirical or numerical, with limited theoretical work. The few theoretical works are presented here first. Greene et al. [12,13] developed a static model to predict bubble volume required for its passage through the interface, $V_g{}^*$, by equating the minimum buoyancy force experienced by the bubble to the maximum interfacial tension force. The critical volume required for bubble passage was given by:

$$V_g^* = \left(\frac{3.9\sigma_I}{g\left(\rho_T - \rho_g\right)}\right)^{\frac{3}{2}} \tag{9}$$

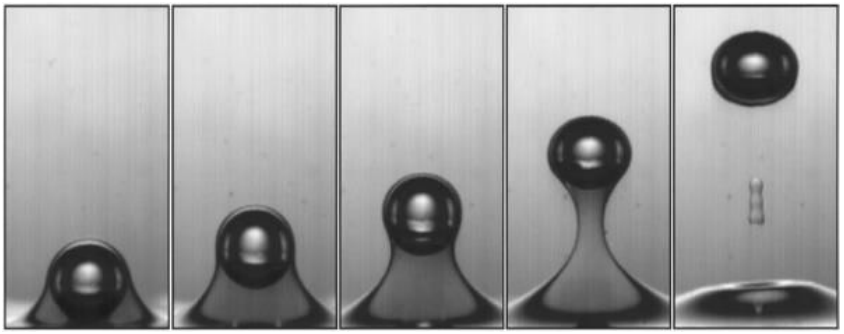

**Figure 10.** *Bubble shell formation during passage of a bubble through an ink-water and kerosene interface [35].*

where $\sigma_I$ is the interfacial tension, $g$ is the gravitational constant, $\rho_T$ is the density of the top liquid, and $\rho_g$ is the density of the gas. Additional criteria were also derived to predict the minimum volume required to induce entrainment of the bottom liquid. Perhaps the most extensive theoretical analysis was carried out by Hashimoto and Kawano [31] to predict the formation of bubbles shells during bubble passage, as shown in Figure 10. Four forces are used to model the bubble trajectory: buoyancy, drag, added mass, and a rebound (i.e. film) force. Using bubble radius, $R$, and $\sqrt{R/g}$ as representative length and time, an equation for dimensionless bubble displacement, $z*$, as a function of dimensionless time, $t^*$, is derived by equating the sum of these four forces to zero:

$$\frac{d^2z^*}{dt^{*2}} = 2 - 3\alpha\,\frac{(2+h^*-z^*)(h^*+z^*)}{(1+h^*)^3} - \frac{2}{\beta}\frac{dz^*}{dt^*}\frac{f}{1+(f+1)h^*}\left(1-\left(\frac{1-z^*}{1+h^*}\right)^3\right) - \frac{6f}{\gamma}\frac{dz^*}{dt^*} \quad (10)$$

where $f$ is a scaling factor between 1-3 depending on Reynolds number, $h^*$ is dimensionless film thickness, $\alpha=\sigma_I/(R^2\rho_B g)$, $\beta=\rho_B(R^3g)^{1/2}/\mu_B$, and $\gamma=\rho_B(R^3g)^{1/2}/\mu_T$ are dimensionless numbers in which $\rho_B$ is the bottom liquid density, $R$ is bubble radius, $\mu_T$ and $\mu_B$ are the top and bottom liquid viscosity respectively, and all other quantities are as defined in the previous paragraph. The first dimensionless number is the inverse of the bottom interfacial

Bond number, and the second two are variations of the Archimedes number. Flow around the bubble is expressed using the Hadamard-Rybczynski solution for flow past a bubble. Using this solution and the assumption that the film has a concentric spherical shape and uniform thickness, a dimensionless expression for film thinning rate, $dh^*/dt^*$, is give as:

$$\frac{dh^*}{dt^*} = \frac{-\frac{f}{2}\frac{dz^*}{dt^*}(2 - z^*)(h^* + z^*)h^* - h^*\frac{dz^*}{dt^*}}{2h^* + z^*} \tag{11}$$

Equations 10 and 11 are solved simultaneously to give the bubble movement and film thickness as a function of time. An assumed rupture thickness of 10 μm is used to determine shell formation criteria. If the film does not reach this thickness before the bubble stops once, it is assumed to be shell formation. Comparison is made to experimental data, but only based on whether the bubble stops at the interface once or passes through the interface. Subsequent theoretical studies have also been conducted on the drag coefficient, equations of motion, and small-amplitude oscillations of these bubble shells [32–34]. Closely related, the passage of solid spheres through a liquid-liquid interface have also been considered [65,66]. Lastly, theoretical models for metallurgical applications have been developed to derive mass transfer coefficients across the liquid-liquid interface based on diffusivity, gas flow rate, and container diameter [14,24–26].

A number of experimental studies have focused on liquid entrainment associated with bubble passage through a liquid-liquid interface [12–15,67,68]. Greene et al. [12] explored the entrainment that occurred as a result of this process with nine different fluid combinations made from water, silicone oil, R11, bromoform, hexane, acetone, and glycerine [12,13]. His results indicated that entrainment volume decreased significantly with increasing density of the lower liquid or decreasing density of the upper liquid [13]. Interfacial tension was shown to have relatively little effect on entrainment volume but did affect the onset of entrainment. The entrainment volume increased significantly when the viscosity of the lower fluid decreased but was not nearly as sensitive to changes in the viscosity of the upper fluid. Reiter and Schwerdtfeger experimented with water, cylcohexane, mercury, and silicone oil combinations [14,15]. The residence time of the bubble at the interface, the height of the column formed under the bubble, and characteristics of drops formed in the upper phase were documented and correlated with dimensionless parameters.

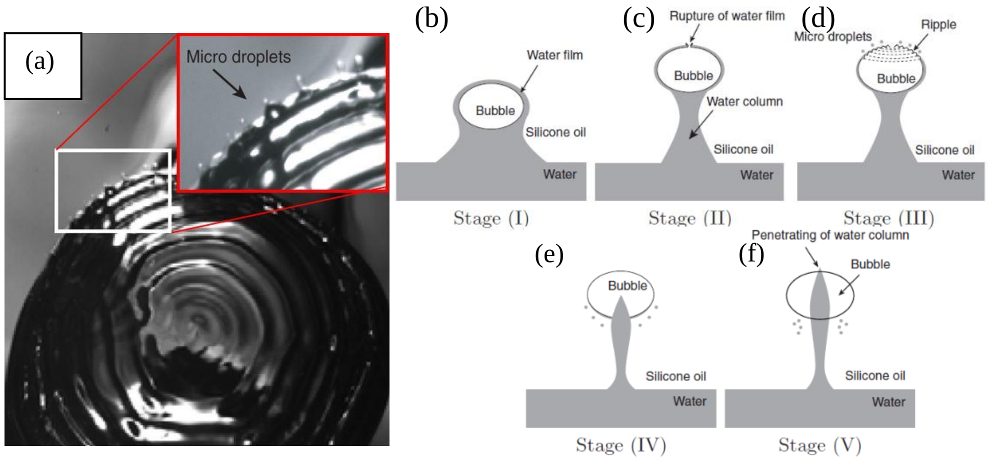

**Figure 11.** *(a) Ripples and microdroplets formed during film rupture and (b)-(f) stages of film rupture during bubble passage through an interface [69].*

Additional experimental studies have also been carried out to understand other fluidic phenomena associated with bubble passage through a liquid-liquid interface [17,18,20,30,64,69]. Uemura et al. [69] focus on an interesting phenomenon that occurs during film rupture as a bubble passes through a water-oil interface. After film rupture, the film retracts around the bubble and forms concentric ripples around the rupture point, which can be seen in Figure 11(a). These ripples then break out into microdroplets as the film continues to retract around the bubble. The various stages of this process were classified into the stages shown in Figure 11(b)-(f). Dietrich et al. [20] employed varying viscosity silicone oils and varying solutions of Emkarox with a PIV system to study the effects of bubble size and upper fluid viscosity. Velocity fields around the bubble revealed the circulation patterns seen in both the upper liquid and lower liquid column below the bubble as it passed through the interface. Singh et al. [17] found that for bubbles with $190<Re<750$ and Weber number, $We<0.0125Re$, the rising bubble would bounce at the liquid-liquid interface prior to passing through. Perhaps the most extensive study of bubble passage through a liquid-liquid interface, Bonhomme et al. [18] experimented with water or a glycerin-water mixture as the lower liquid and silicone oils with varying viscosities as the upper liquid. They compare their results with numerical simulations as well. To describe their results, six dimensionless parameters are employed. They map their results based on two of these dimensionless parameters: the bottom Bond number and bottom Archimedes number. One such plot is shown in Figure 12(a). As described in Section 1.2, the Bond number compares the buoyancy force to capillary effects, while the Archimedes number can be thought of as a Reynolds number based on gravitational velocity. Very small bubbles with low Bond numbers (~3) are seen to remain trapped at the interface for extended periods of time. As the Bond number increases, interfacial tension is overcome by buoyancy and the bubble is able to pass through the interface without coming to a complete stop. As the Bond number reaches ~30, the bubble begins to take on a cap form as it rises. For these larger Bond number bubbles, if the Archimedes number is also very high (~8000 in these experiments) then the bubble takes on a toroidal shape. Agreement with a numerical model that employed a volume of fluid (VOF) approach based on the Navier-Stokes equation was also attained. The numerical simulations are able to capture all of these except the very low Bond number bubbles that remain trapped at the interface. Images taken during their experiment with Newtonian fluids are shown in Figure 12(b), while numerical simulation results are shown in Figure 12(c).

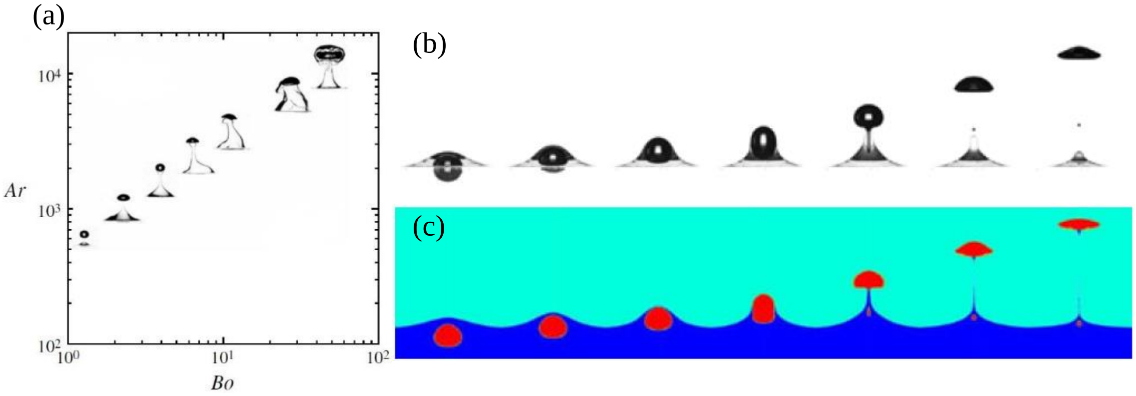

**Figure 12.** *(a) Dimensionless mapping of bubble passage through a liquid-liquid interface, (b) experimental and (c) computational results for bubble passage through a liquid-liquid interface with Bo=13.3 and Ar=4.15 [18].*

A range of numerical simulations have also been presented to model bubble passage through a liquid-liquid interface [16,19,70]. Manga and Stone [70] explored the passage of bubbles, drops, and rigid spheres through a fluid-fluid interface. They discuss several key features of the process, including the influence of viscosity ratio and Bond number on drop and interface deformation and drainage rate of the film between the drop and interface. As seen in Reiter and Schwerdtfeger [15], decreasing the ratio of upper to lower liquid viscosity increased the volume of entrained fluid. A particle simulation was developed by Natsui et al. [16] that was capable of accurately predicting change in bubble height and shape during its passage through a liquid-liquid interface; however, the thin film rupture predictions were not reliable. Singh and Bart [19] used the VOF method to perform a parametric study. They found the height of the column formed beneath the bubble reduces with increased interfacial tension. The bubble passage process is also quickened when the viscosity of the lower liquid is decreased or the density of the lower liquid is increased.

Any study on the passage of bubble streams through a liquid-liquid interface has been almost entirely forgone. A small mention of it is, however, made by Hashimoto and Kawano [31]. They state that when several gas bubbles reached the interface, they grouped together and passed through the interface, forming a compound column of the lower liquid with the bubbles inside. Once a certain height was reached, the column broke down and an encapsulated drop with multiple bubbles at its core was formed. Duangsuwan et al. [63] injected a stream of nitrogen bubble through a sunflower oil-methanol interface in an attempt to make continuous bubble shells. While possible, they found that the stabilization of the film around the bubble after its formation was difficult to maintain.

## 2.3 Bubble Growth in Direct Contact Evaporation

One of the applications of interest related to the current work is direct contact evaporation. Heat transfer in two-phase direct contact systems has been studied for both evaporation and freezing configurations. In the case of evaporation systems, single droplets evaporating in spray column configurations (described in Section 1.3.3) is the main focus area. Significant analytical studies have been carried out to enable the prediction of heat transfer and bubble growth rate during the evaporation of a single liquid drop in an immiscible superheated bulk liquid. The first question that needs to be addressed is the location of the nucleating bubble and the nature of the liquid shell surrounding the bubble. Johnson and Sadhal [42] and Mori [71] studied interaction between a bubble and a dispersed liquid phase in an immiscible liquid medium and proposed a spreading coefficient, $S_i$, to predict bubble engulfment. The spreading coefficient is given by:

$$S_i = \sigma_{jk} - \left(\sigma_{ij} + \sigma_{ik}\right) \qquad (i \neq j \neq k = A, B, G) \tag{12}$$

where $A$, $B$, and $G$ denote the dispersed, continuous, and gas phases respectively. Based on the spreading coefficient, a two-phase droplet can take one of four configurations, as shown in Figure 13 [71]. Avedisian and Andres [72] studied bubble nucleation in a superheated liquid-liquid emulsion, specifically a hydrocarbon-water emulsion. They suggested that nucleation takes place at the liquid-liquid interface and the bubble remains within the hydrocarbon phase.

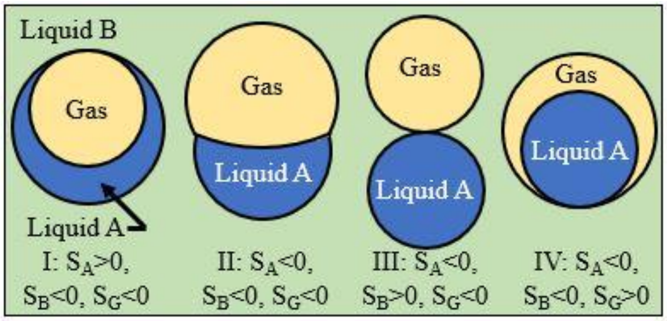

**Figure 13.** *Possible configurations of liquid-gas two phase bubbles. Redrawn from [71].*

Bubble growth models found in literature can be classified into two main categories based on the assumed geometry: (i) models that assume the nucleating bubble is partially covered by the evaporating liquid while the rest of the bubble is in direct contact with the bulk liquid, and (ii) models that consider the bubble to be completely engulfed by the evaporating liquid.

A seminal work on heat transfer in single droplet systems was conducted by Sideman and Taitel [73]. The authors considered that a segment of the bubble is exposed to the bulk liquid and the evaporating liquid covers the rest, forming a crescent shape around the bubble. The net heat transfer coefficient expressed in terms of Nusselt number, $Nu$, was found to be proportional to the initial volume of the droplet and was expressed as a function of the bubble opening angle, $\theta$, and Peclet number, $Pe$:

$$Nu = [(3\cos\theta - \cos^3\theta + 2)/\pi]^{0.5} Pe^{0.5} \tag{13}$$

As the bubble grows, the volatile liquid shell becomes thinner and reduces the conduction resistance across the shell. However, the model predicts very high heat transfer coefficients during initial phases of bubble growth due to large liquid-liquid interface area. Tochitani et al. [74,75] proposed a rigid sphere model where the liquid-liquid interface area was assumed to remain constant up to a vaporization ratio of 10% and reduced upon further evaporation. Raina and Grover [76] introduced the effect of viscous shear on the spreading of the dispersed phase over the bubble interface. Comparison between these models and experimental data is shown in Figure 14. Contrary to Sideman and Taitel [73], a regression analysis carried out by Battya et al. [77] showed that the Nusselt number is influenced by the liquid temperature difference through Jakob number, *Ja*:

$$Nu = 0.64 Pe^{0.5} Ja^{-0.35} \tag{14}$$

Haustein et al. [78] studied bubble growth in a two-phase droplet at high superheats through sudden depressurization. They proposed a simplified model of bubble growth where a liquid shell is present around the bubble until 30% evaporation, after which the shell is assumed to rupture. Their droplet configuration is similar to that described by Sideman and Taitel [73]. They identified three characteristic times during bubble growth relating conduction heat transfer, convection heat transfer, and the shell rupture.

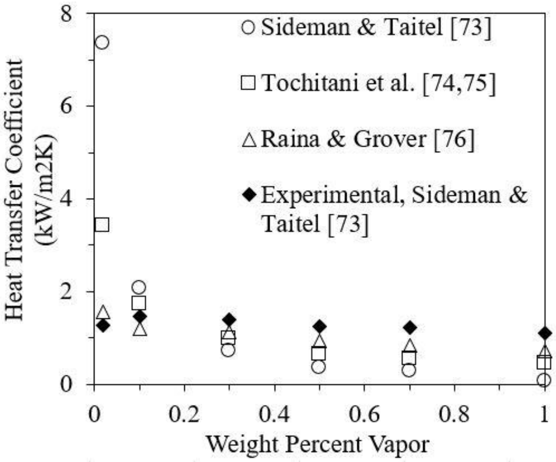

**Figure 14.** *Comparison of instantaneous heat transfer coefficients using various models.*

Avedisian and Suresh [79] developed a numerical model to predict bubble growth rate when a bubble nucleates in a superheated droplet surrounded by an immiscible, superheated bulk liquid. The initial temperature of both liquids is assumed to be the same.

The continuity, momentum, and energy conservation equations were solved to obtain the bubble growth rates. It was seen that until the thermal boundary layer at the liquid-vapor interface reaches the droplet boundary (liquid-liquid interface), bubble growth is similar to the well-studied bubble growth in an infinite superheated liquid. As the thermal boundary layer reaches the liquid-liquid interface, the cooling of the bulk liquid also influences the bubble growth rate. If the thermal conductivity of the bulk liquid is greater than the evaporating liquid, an increase in bubble growth rate is observed, and the growth rate slows down if the thermal conductivity of the bulk liquid is lower. Similarly, it was seen that the bubble growth rate increases as the thermal mass of the bulk liquid increases. For each of the results presented, the bubble growth rate was seen to be similar in the initial stages of bubble growth and diverged only after the bubble diameter was over half the final diameter. More recently, Roesle and Kulacki [80] also developed a one-dimensional radial model to simulate boiling of small drops as well as the oscillations of the resulting bubble. They employ the momentum and energy conservation equations to model the growth and assume an initial uniform superheat throughout the droplet. Similar to Avedisian and Suresh [79], they find that the initial bubble growth is similar to bubble growth in an infinite medium, and later stages of bubble growth are highly dependent on the surrounding liquid properties. They further found these effects to be more pronounced in larger droplets. The magnitude of the oscillations occurring after complete evaporation are also seen to increase with increasing thermal conductivity, density, and specific heat of the bulk liquid.

## 2.4 Research Needs

Bubble interactions at multi-fluid interfaces play an important role in numerous industrial applications. The outcomes of these interactions are directly related to the process efficiency in these applications. This efficiency could be in terms of the mass or heat transfer coefficient (Section 1.3.1 and 1.3.3), shell production rate (Section 1.3.2), emulsion production rate (Section 1.3.4), or another similar efficiency measure. Therefore, it is important to understand the related underlying physics to improve system performance. Nonetheless, bubble interactions with a liquid-liquid interface have received significantly less research focus than similar processes such as bubble collisions with a free surface [62,81,82] or a solid surface [53,83]. In the works that have been reported thus far, the findings are mostly qualitative in nature. Although there have been some grid-based simulations of single bubble passage, accurately capturing both bubble movement and film thinning is problematic since variations in length scales requires adaptive grids spanning six orders of magnitude [47]. Thus, a research gap exists in the theoretical understanding of the underlying phenomenon involved in this process. The formation of bubble shells is of particular interest due to their long list of possible uses. Even less explored yet is the interaction of a bubble stream with a liquid-liquid interface. The majority of previous work on bubble interactions at a liquid-liquid interface has focused solely on single bubble passage. Very little is known about bubble stream passage, and thus, its potential remains a mystery. Both qualitative and quantitative studies on bubble stream passage are needed to identify possible flow patterns, related physics, and potential applications. The collision of bubbles with compound interfaces are a very new extension of this field that have only recently, within the past 5 year, begun to be explored. Similar to bubble streams, very few efforts have been made to develop an in-depth understanding of this process.

The application of bubble passage through a liquid-liquid interface has not extended far into the heat transfer field outside of the metallurgical applications. However, direct contact evaporation is another area that could benefit from its employment. Specifically, the formation of bubble shells is of particular interest as it would enable evaporation to occur at very low superheats due to the pre-existing vapor core, thus increasing the associated heat transfer coefficients. To this extent, the heat transfer process related to bubble growth in direct contact evaporation is of significant interest and worthy of further exploration.

# 3 Experimental Details

This chapter will outline the four experimental setups used to capture bubble interactions with multi-fluid interfaces. The first was used to capture single bubble and bubble stream passage through a liquid-liquid interface. Next, the setup used to capture immiscible bubble growth is described. Following this, the interferometry technique employed to characterize bubble-solid surface collisions is outlined. Finally, the setup used to capture bubble collisions at liquid-liquid and compound interfaces is detailed. The cleaning process and video analysis used to capture bubble size, motion, and growth is also described along with the pertinent liquid properties.

## 3.1 Bubble Passage Setup

The experimental setup developed for capturing single bubble and bubble stream passage through a liquid-liquid interface is shown in Figure 15(a). The system consisted of a 50 mm long piece of square aluminum tube with an inner width and height of 127 mm, and a wall thickness of 12.7 mm. Borosilicate glass windows were laterally compressed to both ends of the square tube using aluminum compression plates with silicone gaskets on either side of the glass plate to ensure a leak free system and reduce localized stress on the glass. Ten M10 screws were used to maintain pressure on the glass. A 12 mm hole was drilled in the bottom of the housing container, and an additional air injection component was added to the setup which is shown in Figure 15(b). This consisted of a 40 mm × 40 mm × 20 mm aluminum block with a central through hole and 1/8-inch NPT threads machined on either side for a needle and compression fitting. Four M4 screws secured the aluminum block to the housing container with a gasket between the aluminum block and housing container to ensure no leakage occurred. Compressed air was fed from a tank to the inlet using 1/4-inch plastic tubing and the flow rate was controlled using the pressure regulator on the tank and a needle valve. Four different needles (5, 8, 13, and 16 gauge) were used to generate bubbles varying from 2-6 mm in diameter. All experiments were conducted at 22°C.

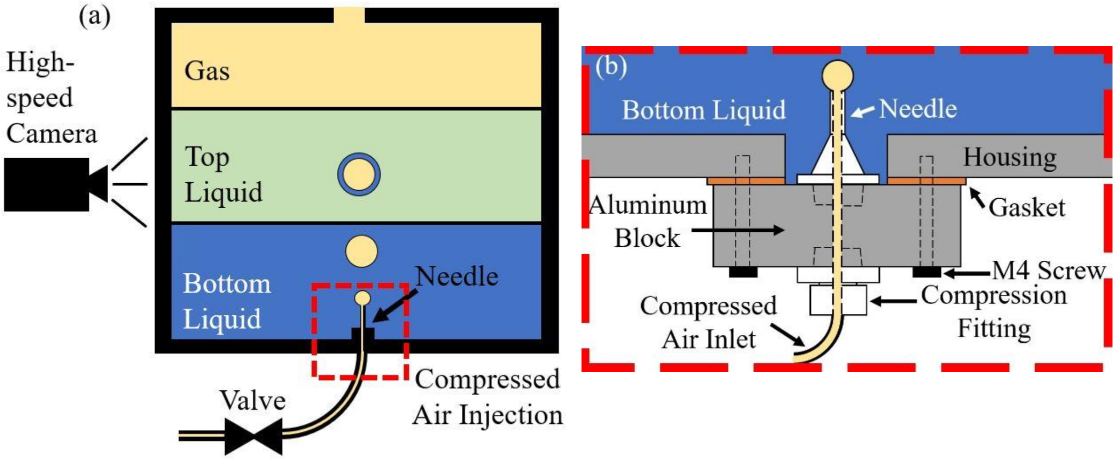

**Figure 15**. *(a) Schematic of experimental setup used for bubble passage through a liquid-liquid interface, and (b) expanded view of needle holder.*

Water, ethanol, the fluorocarbon refrigerant PP1, and three different viscosity silicone oils (10, 20, and 100 cSt) were used to create six liquid-liquid interface systems. The liquid combinations were chosen to cover a broad range of interfacial tensions, viscosity ratios, and density differences. The pertinent liquid properties are described later in Section 3.7. The experimental procedure consisted of attaching the needle holder with the desired needle size, adding first the bottom liquid and then the top liquid to the container, and then starting the air flow. The bubble size, impact velocity, and frequency were captured using video analysis as described in Section 3.6. Bubbles ranging from 2-6 mm in diameter, impact velocities from 5-55 cm/s, and frequencies from 5-40 bubbles/s were tested. The top liquid layer varied in height between 30-65 mm.

## 3.2 Immiscible Bubble Growth Setup

Experimental tests focused on analyzing boiling in an immiscible droplet were conducted in the same housing used for the bubble passage experiments. A 200-Watt auxiliary cartridge heater was incorporated on the side of the container to heat the bulk liquid, and a K-type thermocouple was used to measure the bulk liquid temperature. The setup is shown in Figure 16. FC-72 was used as the evaporating liquid and water was used as the bulk liquid for all experiments. All experiments were run at atmospheric pressure. Once the bulk liquid reached a constant temperature throughout, a micropipette was used to introduce a droplet of FC-72 into the bulk liquid through a hole in the top of the setup. High-speed videos of the evaporation were captured to analyze the bubble growth process. Although a clear boundary of the vapor core was not discernible, the growth rate of the liquid-liquid interface was captured and recorded.

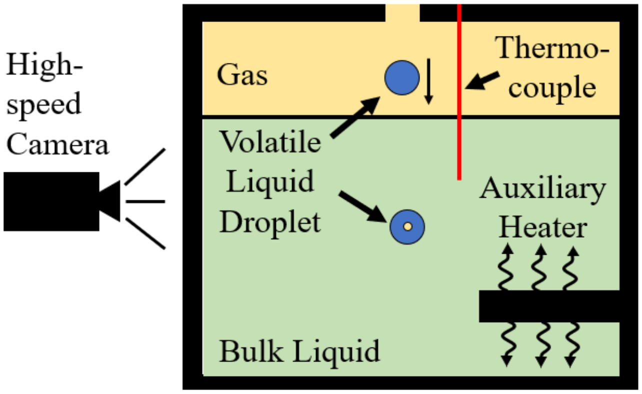

**Figure 16.** *Experimental setup used to measure bubble growth in an immiscible droplet.*

## 3.3 Interferometry Setup

The experimental setup used to characterize bubble collisions with a solid surface is shown in Figure 17. A rectangular polycarbonate column with an inner cross section of 5.1 cm by 3.8 cm and a height of 12.7 cm was used as the primary housing. All experiments were carried out at atmospheric pressure and room temperature, 22°C, with deionized water. A custom, 3D printed mount was placed at the top of the container to hold a Corning pre-cleaned 1 mm thick glass micro slide and to maintain the position of the needle below the glass surface. A 32-gauge needle with an inner diameter of 0.108 mm connected to a 1 ml syringe was used to generate bubbles. A solenoid valve controlled with LabVIEW was employed to regulate air flow and form single bubbles of radius 0.95 mm at the needle tip. The distance between the needle tip and glass surface was varied between 33 mm and 2.6 mm to alter the velocity of the bubble when impacting the glass surface.

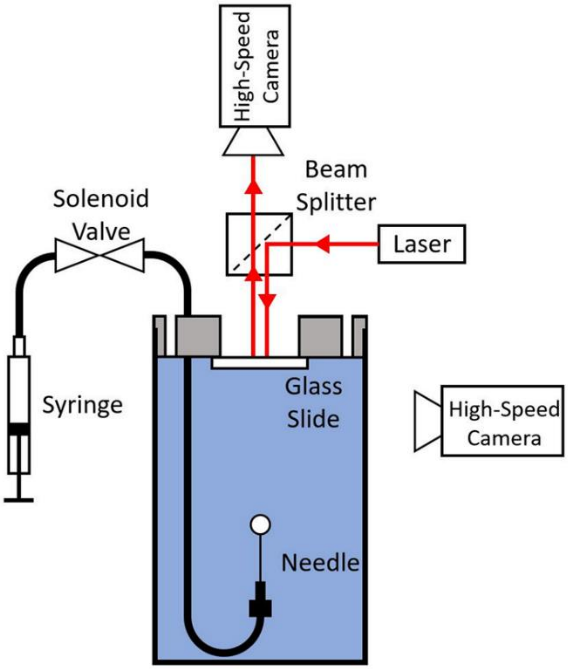

**Figure 17.** *Schematic of experimental setup used to capture bubble collisions with a solid surface.*

During experiments, a small displacement in the syringe was used to generate the pressure needed for bubble formation. The solenoid valve was then opened for a short interval to form a single bubble at the needle tip. The bubble size and trajectory were determined from a side profile of the collision captured with a high-speed camera. As will be discusses in detail in Section 4.3, a primary goal of these experiments was to capture the radial size of the film formed on impact. In order to do so, an interferometry system was employed. A 130-mW laser with a 15 mm beam diameter and 660 nm output wavelength was aimed towards a 50:50 non-polarizing beam splitter to direct the light towards the glass slide. When the bubble collided with the glass slides, variations in the film thickness generated interference patterns which were captured using a second high-speed camera. This technique was first developed by Hendrix et al. [9] to capture the film thickness profile. In the present experiments, the outer edge location of the interference patterns was measured to determine the film radius.

### 3.4 Liquid-Liquid and Compound Interface Collision Setup

The experimental setup used to capture bubble collisions with liquid-liquid and compound interfaces is shown in Figure 18. The primary housing consisted of a rectangular polycarbonate column with an inner cross section of 5 cm by 5 cm, and height of 15 cm. A glass capillary tube with an inner diameter of 0.05 mm was placed at the bottom of the container to generate single bubbles of radius 0.65 mm. A Cole-Parmer Masterflex L/S peristaltic pump was used to control air flow to the capillary. In this testing, water was always used as the bottom liquid and 1, 5, or 10 cSt silicone oil was used as the top liquid. In order to attain various film thicknesses, a prescribed volume of the top liquid was carefully added to the container as determined by the cross-sectional area of the container multiplied by the desired film thickness. The influence of the meniscus formed at the container edge was neglected due to the large cross-sectional area of the container. Film thicknesses of 0.25, 0.50, and 1.00 mm were tested as compound interfaces. For solid-liquid-liquid compound interfaces, a solid polypropylene surface was additionally placed above the top liquid. Polypropylene was chosen due to its oleophilic and hydrophobic properties, which promoted the stability of the oil layer formed between the water and the solid surface. For liquid-liquid interface collisions, the top liquid layer thickness was increased to ~10 mm, a value much larger than the expected interface deformation.

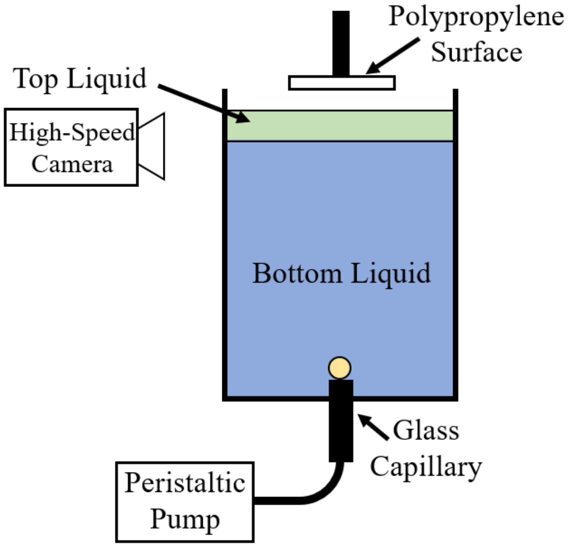

**Figure 18.** *Experimental setup used to capture bubble collisions with liquid-liquid and compound interfaces.*

The experimental procedure went as follows: after cleaning, the container was filled with water to produce the desired distance between the capillary and interface. The specific volume of the top liquid was then carefully added to form the desired top layer thickness. The polypropylene surface was then lowered into place if testing for the solid-liquid-liquid interface. The peristaltic pump was then actuated to form a single bubble. The bubble collision at the interface was captured using a high-speed camera. Video analysis was then used to determine the bubble trajectory and velocity.

## 3.5 System Cleaning

Between experiments, the system containers were thoroughly washed using hot water and dish soap to remove any contaminants or leftover liquid. Once clean, the container was rinsed several times with hot water and was then placed in a hot water bath for several hours. The container was rinsed several more times with hot water to remove any remaining contaminants. The system cleanliness can significantly alter the behavior of the bubble in any of the systems described in Sections 3.1-3.4. Specifically, the bubble surface mobility is very sensitive to system contamination levels. For a "clean" bubble, the surface is fully mobile while a "contaminated" bubble has an immobile surface. These surface conditions are reflected in the bubble terminal velocity in that clean bubbles have significantly higher terminal velocities compared to contaminated bubbles due to their respective surface conditions. A theoretical terminal velocity can be determined by equating the buoyancy and drag forces to yield $V_T^2=8Rg/3C_D$, where $R$ is the bubble radius, $g$ is the gravitational constant, and $C_D$ is the drag coefficient. The drag coefficient may be found for a clean or contaminated bubble using the theory compiled by Loth [84], which is described in Section 4.3.3. As an example, a 0.65 mm radius bubble has a terminal velocity of 34.0 cm/s if it is clean and just 14.2 cm/s if it is contaminated. The terminal velocity reduces very quickly once the contaminant concentration reaches a critical threshold, and intermediate terminal velocities can only be attained with very precise control of the surface-active substance concentration [85]. In the results described in this dissertation, the bubble terminal velocity coincided with that theoretically predicted for a clean bubble. As such, it was concluded that the bubbles rose with mobile surface conditions and the cleaning process was sufficient.

### 3.6 Video Analysis

All of the experiments conducted here rely on video analysis to characterize the given process. High-speed videos were captured using either a Photron FASTCAM 1024 PCI camera or a Keyence VW-6000 camera at 1000 or 3000 fps. From these videos, bubble or droplet size, trajectory, velocity, and frequency were measured as needed. Calibration for converting pixels to mm was made prior to recording using an object of known size, such as the capillary tube or needle outer diameter as shown in Figure 19(a). The equivalent diameter, $D$, and radius, $R$, was calculated as $D=2R=(D_h^2 D_v)^{1/3}$, where $D_h$ and $D_v$ are the horizontal and vertical bubble diameters, as shown in Figure 19(b). This equivalent diameter, or radius, was used in all subsequent calculations requiring bubble size. For bubble passage and bubble collision testing, horizontal and vertical bubble diameter measurements were taken prior to bubble interaction with the interface. The bubble trajectory was determined by tracking the location of the bubble center or side. This was done using the Photron FASTCAM Analysis software or manually. The instantaneous bubble velocity was then determined from the trajectory data using a second-order central finite difference scheme given as:

$$V_i = \frac{y_{i+1} - y_{i-1}}{2\Delta t} \tag{15}$$

where $y$ refers to the vertical position of the bubble as shown in Figures 19(b) and (c), the subscript of $V$ and $y$ refers to the corresponding frame or time, and $\Delta t$ is the time between frames. For bubble streams, the frequency of the bubbles is calculated by counting the number of bubbles passing through a horizontal line over a measured period of time.

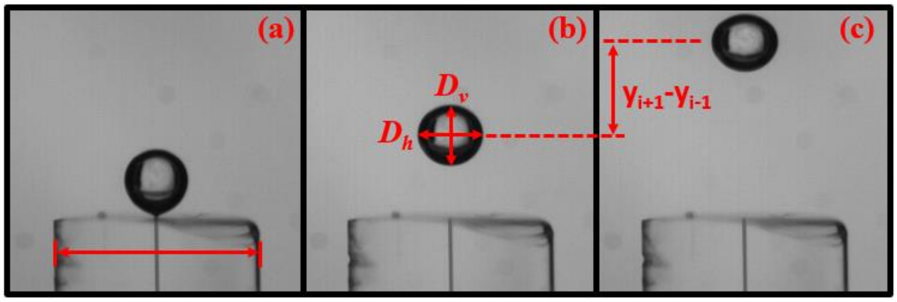

**Figure 19.** *(a) 4 mm outer diameter capillary used for spatial calibration, (b) horizontal and vertical bubble diameter measurement, (b)-(c) bubble displacement used in velocity calculation.*

## 3.7 Liquid Properties

The liquid properties used for experimental validation of the diabatic studies have been listed in Section 4.2.3 for readability purposes. Considering only the adiabatic studies, there are three primary liquid properties that govern the behavior of the systems considered here: density (ρ), viscosity (μ), and surface tension (σ). The experiments conducted here employed liquid combinations made up from eight different liquids: water, five different silicone oils (SO) with viscosities ranging from 1-100 cSt, ethanol, and the refrigerant PP1. The pertinent properties for each of these liquids are listed in Table 2. The properties of the silicone oils and PP1 were taken as specified by the manufacturers [86–89] while the properties of water and ethanol are found in literature [90].

**Table 2.** *Properties of experimental liquids at 25°C.*

| Liquid | Density, ρ (kg/m$^3$) | Viscosity, μ (mPa·s) | Surface tension, σ (mN/m) |
|---|---|---|---|
| Water | 1000 | 1.00 | 72.0 |
| SO-1 | 818 | 0.82 | 17.4 |
| SO-5 | 918 | 4.59 | 19.7 |
| SO-10 | 935 | 9.35 | 20.1 |
| SO-20 | 950 | 19.0 | 20.6 |
| SO-100 | 966 | 96.6 | 20.9 |
| Ethanol | 789 | 1.20 | 22.0 |
| PP1 | 1682 | 0.66 | 11.1 |

When considering a two-liquid system, there are also properties specific to the liquid combination which can have a significant impact on the bubble-interface interaction. These include the interfacial tension ($\sigma_I$), viscosity ratio, and the density difference of the two liquids. These properties have been listed in Table 3 for all the liquid combinations used in experiments here. While the viscosity ratio and density difference can simply be found based on the information in Table 2, the interfacial tension cannot. As such, experiments were carried out to measure the interfacial tension of each liquid combination using the

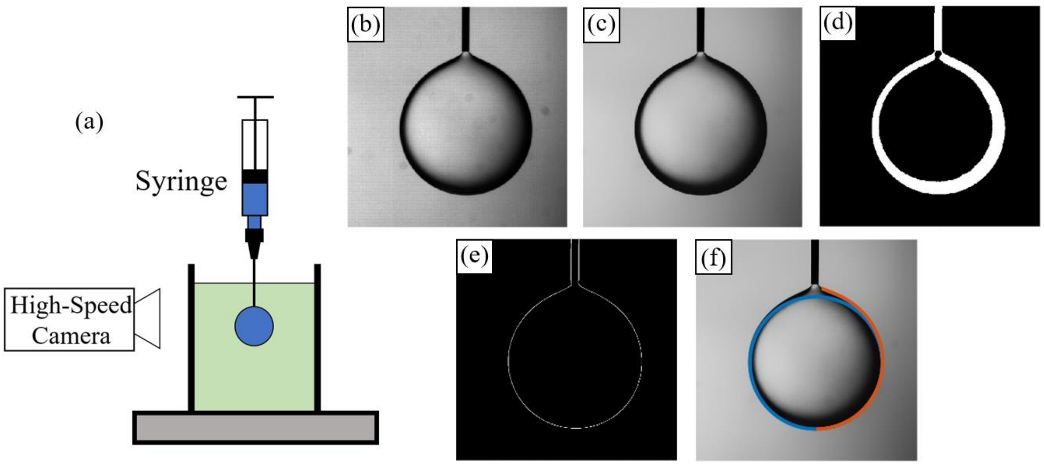

**Figure 20.** *(a) Experimental setup and (b)-(f) pendant drop image processing used to determine interfacial tension.*

setup depicted in Figure 20(a). The setup consisted of a 14 mm × 14 mm × 38 mm square quartz tube. The tube was filled with the less dense liquid first. Then a syringe with a 30-gauge needle was used to inject a droplet of the heavier liquid. A high-speed camera was used to capture snapshots of the pendant drop. Image processing was then performed in Matlab to get the experimental drop profile. This process consisted of applying a bilateral Gaussian filter to the image [91], binarizing the image and filling the holes, and then using a Canny edge detector to determine the location of the droplet boundaries as outlined in Figures 20(b)-(e). Once the experimental drop profile was found, a theoretical profile was fit to the experimental profile to determine the interfacial tension value as shown in Figure 20(f). The shape of axisymmetric pendant drops is governed by the Young-Laplace equation which can be written in the following dimensionless form [92]:

$$\begin{gathered} \frac{d\varphi}{dS^*} = 2 - \omega y^* - \frac{\sin\varphi}{x^*} \\ \frac{dx^*}{dS^*} = \cos\varphi \\ \frac{dy^*}{dS^*} = \sin\varphi \\ at\ S^* = 0 : \varphi = 0, x^* = 0, y^* = 0 \end{gathered} \tag{16}$$

where $\omega=\Delta\rho g a^2/\sigma_I$ is the shape factor, $a$ is the radius of curvature at the drop apex, $\varphi$ is tangent angle of the profile, $S^*$ is the dimensionless arc length, and $x^*$ and $y^*$ are the dimensionless coordinates of the profile where the origin is located at the drop apex. To dimensionalize the coordinates, the respective values are multiplied by $a$. Equation 16 was solved in Matlab for a wide range of $\omega$ and $a$ values to yield the associated theoretical drop profiles. The correct values were determined by minimizing the error between the theoretical and experimental profile which was calculated as:

$$e=\sum_{i=1}^{N}\sqrt{\left(x_{i,th}-x_{i,exp}\right)^2+\left(y_{i,th}-y_{i,exp}\right)^2} \tag{17}$$

The $\omega$ and $a$ values associated with the minimum error were then used to estimate the interfacial tension as $\sigma_I=\Delta\rho g a^2/\omega$. The Matlab code written for this analysis is presented in Section 7.1 of the appendix. Roughly 200 images were analyzed in this way for each liquid combinations. The average interfacial tension values from all images for each respective liquid combination are reported in Table 3.

**Table 3.** *Experimental liquid combinations and properties.*

| # | Bottom Liquid | Top Liquid | Interfacial Tension, $\sigma_I$ (mN/m) | Viscosity Ratio ($\mu_T$ / $\mu_B$) | Density Difference, $\rho_B$ -$\rho_T$ (kg/m$^3$) |
|---|---|---|---|---|---|
| 1 | Water | SO-1 | 50 | 0.82 | 182 |
| 2 | Water | SO-5 | 51 | 4.59 | 82 |
| 3 | Water | SO-10 | 48 | 9.35 | 65 |
| 4 | Water | SO-20 | 43 | 19.0 | 50 |
| 5 | Water | SO-100 | 52 | 96.6 | 34 |
| 6 | SO-20 | Ethanol | 0.3 | 0.063 | 161 |
| 7 | SO-100 | Ethanol | 0.8 | 0.012 | 177 |
| 8 | PP1 | Water | 42 | 1.52 | 682 |

Chapter 4

# 4 Results and Discussion

## 4.1 Flow Regimes and Transition Criteria During the Passage of Bubbles through a Liquid-Liquid Interface

The passage of a single bubble or a continuous stream of bubbles through a liquid-liquid interface can result in a number of different outcomes. For single bubbles, the outcome is dependent on the properties of the two liquids, and the size and impact velocity of the bubble. In addition to these parameters, bubble stream flow patterns are dependent on the frequency with which the bubbles are impacting the interface. For a single bubble passing through a liquid-liquid interface, possible outcomes identified in previous studies include bubbles becoming trapped at the interface [18], bubbles passing through with an encasing shell of the lower liquid [15,22,30–35], and bubbles breaking through the interface [12–20,64,69]. The passage of a stream of bubbles has received significantly less focus than single bubble passage. In one of the few works mentioning bubble streams, the outcome was classified into two regimes: bubble stream penetration with no entrainment, and bubble stream penetration with entrainment [63]. While these previous works have identified the possible outcomes to some extent, there is currently no full identification and classification of all the possible outcomes. To this extent, an experimental study was carried out to identify the flow regimes that are possible for the passage of single bubbles and bubble streams through a liquid-liquid interface and to provide a qualitative description of each regime. Relevant dimensionless numbers are then identified to approximate the transition between each of these regimes.

Three different viscosity silicone oils (10, 20, and 100 cSt), water, ethanol, and the fluorocarbon refrigerant PP1 were used to create six liquid-liquid interface systems. The liquid combinations were chosen to cover a broad range of interfacial tensions, viscosity ratios, and density differences. The pertinent liquid properties are discussed in Section 3.7 and shown in Table 2, and the six liquid combinations and their associated interfacial tensions, viscosity ratios, and density differences are shown in Table 3 as combinations 3-8. Bubbles with diameters ranging from 2-6 mm, impact velocities from 5-55 cm/s, and frequencies from 5-40 bubbles/s were tested to identify all possible regimes.

### *4.1.1 Single Bubble Regimes*

In experimental testing, four flow patterns were identified in association with a single bubble passing through a liquid-liquid interface: (i) the bubble becomes trapped at the interface, (ii) the bubble passes through the interface with a shell of the lower liquid around it, (iii) the bubble passes through and forms a long tail of the lower liquid in the upper liquid, and (iv) the bubble breaks through the interface. These are shown schematically in Figure 21. These are similar to the outcomes identified in previous studies with the addition of the long tail formation.

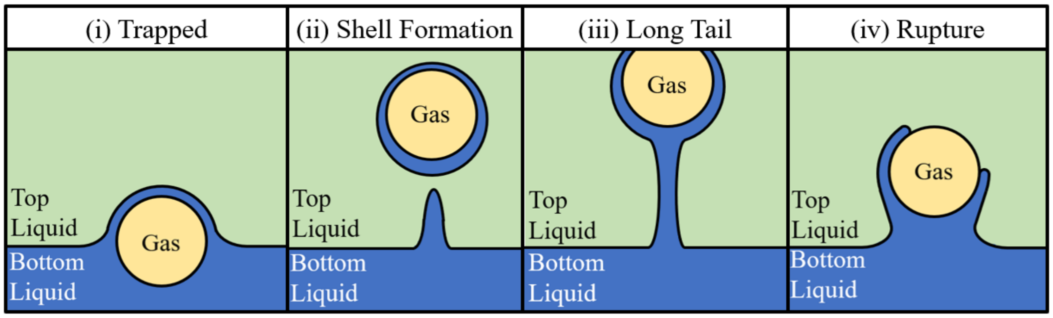

**Figure 21.** *Flow patterns seen with single bubble passage through a liquid-liquid interface.*

*Trapped bubbles:* When a small bubble approached the interface in experiments, it was often seen that the bubble would not pass through the liquid-liquid interface but instead became trapped since the small magnitude of the buoyancy force was unable to overcome the interfacial tension. The bubble velocity would also go negative in some cases as the interface relaxed. A similar phenomenon is seen with bubble impacting a free surface where they can bounce several times at the interface prior to coalescing [62,93]. It is during this rebound cycle that the bubble velocity goes negative and the bubble moves against the buoyancy force. In the present experiments, however, the bubble displayed much more damped motion, so although the bubble rebounded slightly, it remained close to the interface. The bubble then remained trapped at the interface for some duration of time that could vary between milliseconds to minutes depending on the liquid combination and bubble size. During this residence time at the interface, the thin liquid film between the bubble and interface is squeezed by the buoyancy force acting on the bubble and the interfacial tension opposing the buoyancy. The rate at which the film thins is governed by the liquid properties and magnitude of these forces as customarily described by lubrication theory. Eventually, the film reaches a critical thickness and ruptures, allowing the bubble to pass through the interface and continue its rise through the upper liquid. A depiction of this process is shown in Figure 22 with a 3.3 mm diameter bubble trapped at the interface of water and silicone oil 20. This regime was seen only with the higher interfacial tension systems of water and silicone oil or PP1 and water. A trapped bubble is thus classified as one whose velocity and acceleration both go to zero at the same instance. Both the velocity and acceleration requirements are needed to define this regime since the bubble velocity may also go to zero in the case of a bubble that "bounces" at the interface prior to passing through [17]. Bouncing bubbles exhibit a momentary zero velocity due to a change in the bubble's direction of motion, but their acceleration is not zero at that instant and thus may be classified in one of the other three regimes. A basic criterion for predicting this regime has been previously derived by Greene et al. [12] by assuming the buoyancy force experienced by the bubble when located in top liquid, i.e. the minimum buoyancy force, must exceed the maximum possible interfacial tension force in order for the bubble to pass through. Although all of the experiments resulting in trapped bubbles adhered to this criterion, there were certain bubbles that passed through the interface when this model predicted entrapment. A possible reason behind this discrepancy is the fact that the model proposed by Greene et al. [12] is a static model and does not take inertial effects into account.

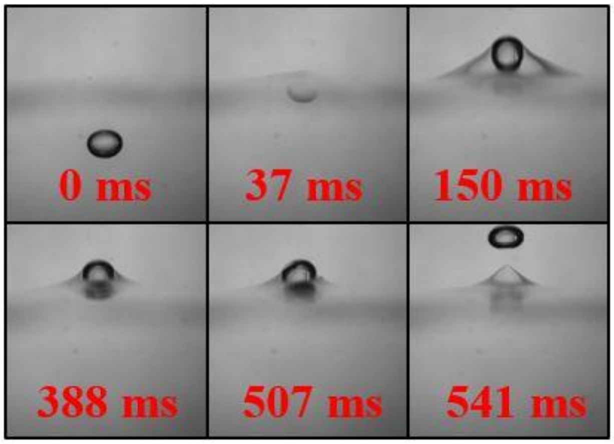

**Figure 22.** *Trapped 3.3 mm diameter bubble seen with water (bottom) and silicone oil 20 (top).*

<u>*Shell formation:*</u> The next regime identified was the formation of a liquid shell around the bubble as it passed through the liquid-liquid interface. This is depicted schematically and pictorially with images captured during experiments with water and silicone oil 100 in Figure 23. The bubble slowed upon reaching the interface, and a thin liquid film was formed between the bubble and interface. As the bubble continued to rise through the interface, the film simultaneously thinned and stretched around the bubble. Once the bubble reached a certain height above the interface, the column of the lower liquid beneath the bubble necked and eventually ruptured, allowing the bubble to continue upward through the top liquid with a film of the lower liquid surrounding it. Hashimoto and Kawano [31] derived an analytical model to predict conditions under which this regime occurs. In the present context, however, this model may only define the transition between

shell formation and rupture. The criterion for shell formation used in the model is just that the film does not reach a critical rupture thickness during its collision, and as such, trapped bubbles would also satisfy this condition.

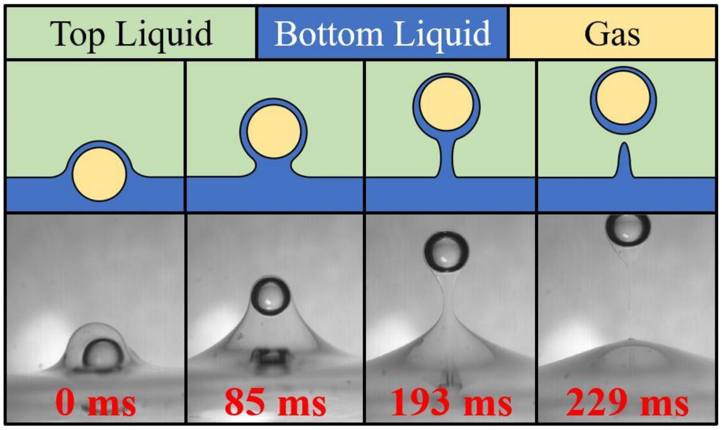

**Figure 23.** *Bubble shell formation shown schematically and experimentally with water (bottom) and silicone oil 100 (top).*

*Long tail formation:* Under very low interfacial tension conditions, such as those seen with any silicone oil and ethanol combination, bubbles would pass through the interface with very little change in their velocity. As the bubble passed through the interface, the lower liquid would encompass the bubble and form a long tail of the lower liquid behind it. The bubble would continue to rise, and the tail would thin but maintain a connection between the bubble shell and interface until the bubble was well out of frame. An example of this regime captured in experiment is shown in Figure 24. The reason for this type of behavior can be attributed to the interfacial tension, relative viscosity, and density difference of the liquid combination. The low interfacial tension requires only a very small amount of buoyancy force to enable bubble passage. Thus, even very small bubbles would be able to pass through the interface, as was seen in experiments. This regime is further associated with relatively high bottom liquid viscosity in comparison to the top liquid. This high viscosity slows the drainage from the film surrounding the bubble, thereby retarding shell rupture and allowing the shell and column to be maintained even after the bubble has moved a significant distance past the interface. Finally, similar liquid densities would further promote this formation since the relative gravitational force on the tail would not be significant and would, therefore, reduce its drainage rate. All of these conditions are satisfied with the silicone oil–ethanol combinations, and for this reason, all bubbles produced this formation regardless of bubble size or impact velocity.

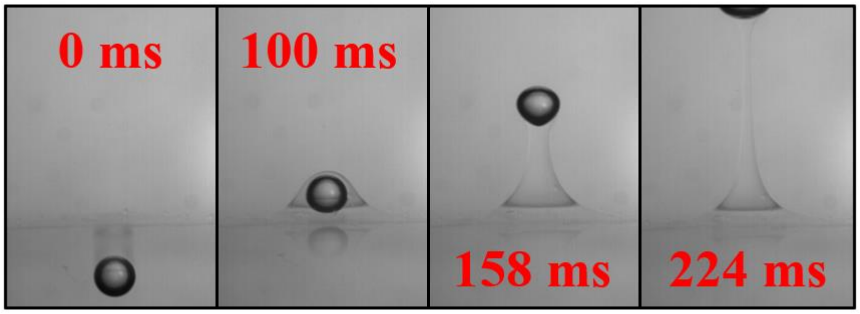

**Figure 24.** *Long tail formation for 2.3 mm diameter bubble passing through silicone oil 100 (bottom) – ethanol (top) interface.*

*Shell rupture:* The final regime seen in experiments was shell rupture. The initial flow behavior in this regime is very similar to that seen in shell formation. The bubble deformed the interface, forming a shell around the bubble with a column of the bottom liquid entrained beneath it. The bubble continued to rise, but instead of the column rupturing as seen in shell formation, the thin liquid film above of the bubble ruptured instead. The film then retracted around the bubble back into the column. As a result, a penetrating column of liquid coming up through the bottom of the bubble was often seen at the end of the retraction. An example of shell rupture seen with a 4.3 mm diameter bubble passing from water to silicone oil 20 is shown in Figure 25 along with a schematic of the rupture process. This process is very similar to that outlined by Uemura et al. [69], who additionally noted the formation of concentric ripples and microdroplets as the film retracted. The reason for this is believed to be surface instabilities as a result of the difference in interfacial and surface tension seen on either side of the film as it retracted. While a number of models have been developed to predict thin film rupture under static conditions [94], the inclusion of dynamic bubble motion effects has not yet been considered.

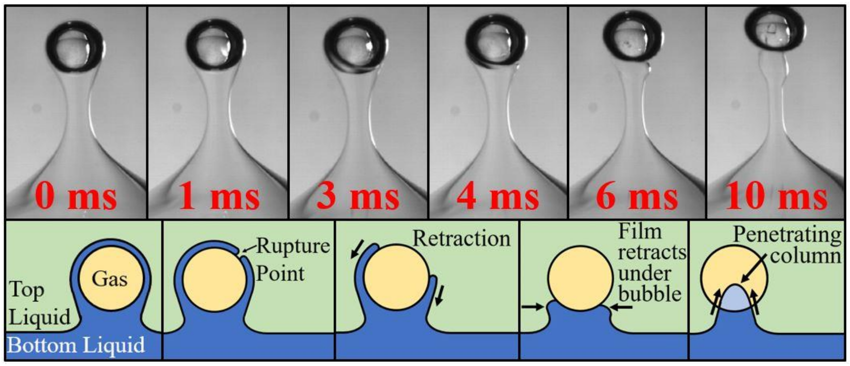

**Figure 25.** *Shell rupture as seen in experiments and a schematic illustration of the rupture process.*

With the flow regimes identified, dimensionless numbers capable of characterizing the regimes were then investigated. Two key competing processes of the collision were considered: (i) the deformation of the liquid-liquid interface, and (ii) the thinning of the liquid film around the bubble. Trapped bubbles experience low interface deformation and low thinning rates. Bubble shells are associated with intermediate-to-high interface deformation with low film drainage rates. The long tail formation was seen with very high interface deformation and very low film drainage rates. The rupture scenario was seen with intermediate-to-high interface deformation and high drainage rates. Thus, two dimensionless numbers capable of characterizing these two processes are investigated for the purpose of mapping these flow regimes.

To characterize interface deformation, a comparison between the kinetic energy associated with the rising bubble and the energy required to produce additional interfacial area was used. Prior to impacting the interface, the kinetic energy of a rising bubble can be calculated as:

$$KE = \frac{1}{2} C_m \rho_B \frac{1}{6} \pi D^3 V^2 \tag{18}$$

where $C_m$ is the added mass coefficient, $\rho_B$ is the bottom liquid density, $D$ is the undeformed bubble diameter, and $V$ is the bubble velocity [62]. The value of $C_m$ varies depending upon the degree of bubble deformation [95]. For an undeformed bubble whose vertical and horizontal diameters are equal, $C_m=0.5$. For deformed bubbles, this value can be found using the ratio of horizontal to vertical bubble diameter and the expression from Tsao and Koch [96]. In order to estimate the additional surface energy required, the static model for an undeformed bubble at a liquid-liquid interface from Greene et al. [12] is used. Neglecting the shell thickness, the excess surface energy associated with the deformed interface in this model can be give as:

$$SE = \pi D^2 \sigma_I \tag{19}$$

where $\sigma_I$ is the interfacial tension. Setting the kinetic and surface energy equal to one another, the following dimensionless relationship is obtained:

$$We_{I,B} = \frac{\rho_B V^2 D}{\sigma_I} = C \tag{20}$$

where $We_{I,B}$ is the Weber number using the bottom liquid density and interfacial tension, and $C$ is some constant. The value of $C$ for the bottom interfacial Weber number is indicative of the kinetic energy required to induce the interface deformation necessary for bubble passage. It is dependent on how much of the kinetic energy is transferred to interface deformation; this energy may additionally be expended on bubble shape deformation or pressure buildup in the thin liquid film ahead of the bubble. In a study from Zawala et al. [93], roughly 20% of the bubble kinetic energy is shown to be transferred to bubble deformation. Additionally, higher $C_m$ values, which are typically seen at higher velocities where bubble deformation is more significant, would reduce this value further. However, this specific value for the bottom interfacial Weber number is not particularly important outside of delineating between bubbles that are trapped or pass through the interface. More relevant to the present work is the ability of the bottom interfacial Weber number to characterize interface deformation and its applicability in flow regime mapping.

Characterization of the film drainage is performed by first considering the well-known flat film drainage rate equation from Scheludko [54], which is based on Reynolds' [4] model for drainage between rigid parallel plates as outlined in Section 2.1. Although the film drainage in the present work will not adhere perfectly to this model due to its curvature and mobile interfaces, it is still appropriate as a first order approximation for identifying characteristic dimensionless numbers. The drainage rate equation is given as:

$$-\frac{dh}{dt}=\frac{2h^3\Delta p}{3\mu_B R_F^2} \tag{21}$$

where $h$ is film thickness, $\Delta p$ is the excess pressure in the film, $\mu_B$ is the bottom liquid viscosity, and $R_F$ is the radial film size. The following parameters are introduced to nondimensionalize this equation:

$$h^*=\frac{h}{D} \qquad t^*=\frac{tV}{D} \qquad R_F^*=\frac{R_F}{D} \qquad \Delta p^*=\frac{\Delta p\mu_B^2}{\rho_B\sigma_B} \tag{22}$$

where $\sigma_B$ is the bottom liquid surface tension. Substituting these parameters into Equation 21 reduces to the following:

$$-\frac{dh^*}{dt^*}=\frac{\rho_B D\sigma_B^2}{V\mu_B^3}\frac{2h^{*3}\Delta p^*}{3R_F^{*2}}=\frac{La_B}{Ca_B}\frac{2h^{*3}\Delta p^*}{3R_F^{*2}} \tag{23}$$

where $La_B=\rho_B\sigma_B D/\mu_B^2$ and $Ca_B=\mu_B V/\sigma_B$ are the Laplace and Capillary numbers, respectively, using the bottom liquid properties. From this, it can be seen that the ratio of Laplace to Capillary number will give insight into the film drainage rate and enable its characterization.

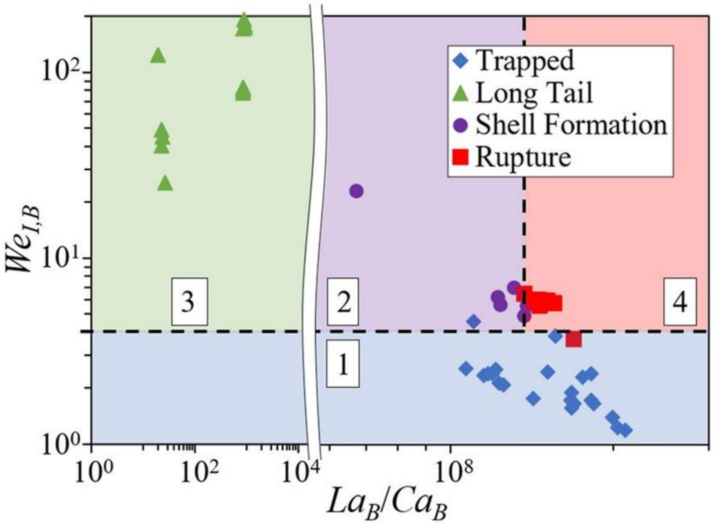

**Figure 26.** *Dimensionless plot for single bubble passage through a liquid-liquid interface.*

Using the dimensionless parameters for interface deformation, $We_{I,B}$, and film thinning, $La_B/Ca_B$, the experimental results are plotted in Figure 26. The abscissa represents film thinning while the ordinate represents interface deformation. The long tail region, region 3 designated in green, occurs at significantly lower drainage rates and high degrees of deformation. The other regions occur at higher $La_B/Ca_B$ ratios. Under a critical bottom interfacial Weber number of ~4, shown with the horizontal dashed line, the trapped formation is shown by region 1 in blue. Below this value, the bubbles are unable overcome the interfacial tension and pass through the interface. Above this value, the map is split into the final two regimes as divided by the vertical dashed line at $La_B/Ca_B=1.37\cdot10^8$. At lower $La_B/Ca_B$ ratios, i.e. lower film drainage, shell formation is seen, as shown with region 2 in purple. At higher $La_B/Ca_B$ ratios, i.e. higher film drainage, the rupture regime is seen, as shown by region 4 in red.

### *4.1.2 Bubble Stream Regimes*

Flow regimes seen with bubble streams displayed a wider variety than those seen with single bubbles. The experimental results have been grouped into six regimes: (i) single bubble equivalent, (ii) partial column formation, (iii) bubble cluster formation, (iv) stable column formation, (v) unstable column formation, and (vi) churn flow. A schematic of each of these is shown in Figure 27. The single bubble equivalent regime occurs when bubble frequency is very low. Under this condition, the leading bubble has already departed from the interface, and the interface has returned to its undisturbed position by the time the following bubble reaches the interface. The outcome of this is regime will be one of the four regimes defined for single bubble passage through a liquid-liquid interface. This regime is not specific to any liquid properties or bubble size; however, these parameters will dictate the frequency range over which this regime can occur.

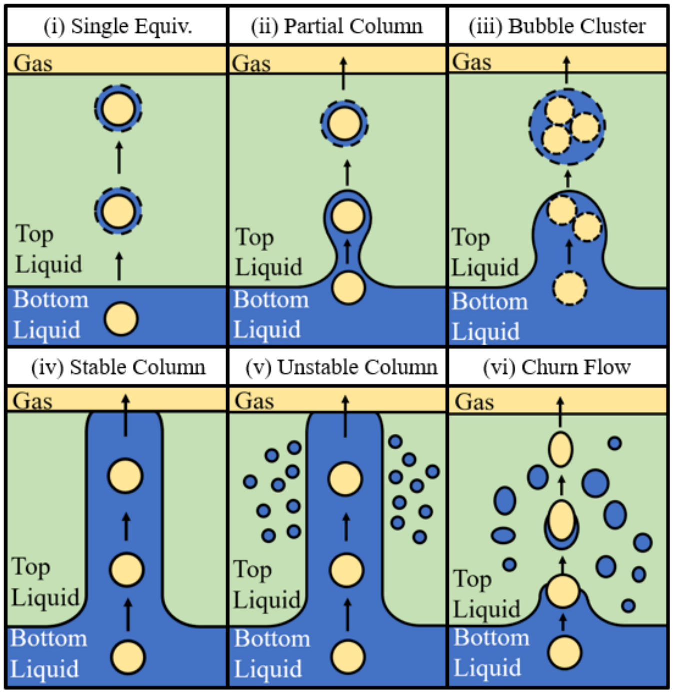

**Figure 27.** *Flow regimes seen with bubbles streams passing through a liquid-liquid interface.*

*Partial column and bubble cluster:* When bubble frequency was increased beyond the single bubble equivalent regime range, two possible configurations were seen next: partial column formation or bubble cluster formation. In partial column formation, the leading bubble would impact and significantly deform the interface. Immediately after the leading bubble departed, the trailing bubble would reach the interface and maintain a partial column of the lower liquid entrained in the upper liquid. The departing bubble may or may not have a shell around it as it leaves the interface. Interface deformation is maintained over time, and it does not return to its undisturbed position. This regime was seen with silicone oil and ethanol combinations as well as with the water and silicone oil combinations. For this regime to occur, the buoyancy force of a single bubble would need to be able to overcome the interfacial tension. Additionally, the lower liquid density should not differ greatly from that of the upper liquid in order to reduce the necking rate in the column below the bubble. If these conditions were not met or if bubble frequency was further increased, the bubble cluster regime was reached instead. In this regime, multiple bubbles would group at the interface prior to passage of the leading bubble. The bubbles may or may not coalesce into a single larger bubble depending on the surface tension of the lower liquid. This was seen with intermediate bubble frequencies with water and silicone oil combinations, and at low to intermediate frequencies with PP1 and water. With water and silicone oil, the bubbles would not coalesce but would become encompassed in a single droplet of the lower liquid. A similar process has been observed with solid particles [97]. Due to the lower surface tension of PP1 and the high interfacial tension in the water-PP1 system, multiple bubbles would coalesce at the interface to form a single larger bubble. Bubbles would continue to coalesce until the buoyancy force of the larger bubble was able to overcome the interfacial tension. The partial column and two examples of the bubble cluster formation are shown in Figure 28.

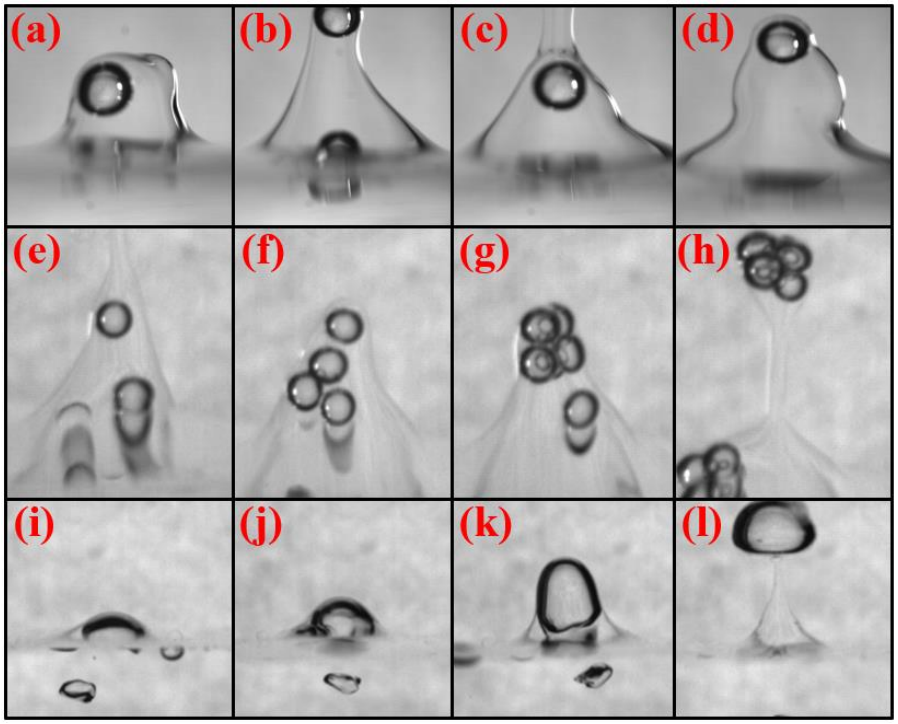

**Figure 28.** *(a)-(d) Partial column formation seen with water and silicone oil 20, (e)-(h) bubble cluster formation without coalescence seen with water and silicone oil 10, and (i)-(l) bubble cluster formation with coalescence seen with PP1 and water.*

*Stable or unstable columns and churn flow:* As bubble frequency was further increased beyond that of the partial column and bubble cluster regimes, the column grew in height until it reached the free surface. Under these conditions, a stable column of the bottom liquid was formed in the top liquid. An illustration of this formation process is shown in Figure 29(a)-(d) and (g)-(j). This regime was only seen with the water-silicone oil combinations. Silicone oil-ethanol combinations instead produced unstable columns as shown in Figure 29(e) and (k). In this regime, a column was formed but the outer liquid-liquid boundary of the column did not remain well-defined. Instead, droplets were seen to break away from the liquid-liquid boundary and create a dispersion of the lower liquid in the upper liquid. Unstable columns were also seen with water-silicone oil combinations when the bubble frequency was further increased after a stable column was formed. Further increases in bubble frequency resulted in a chaotic flow with no distinct geometric feature, as shown in Figure 29(f) and (l). PP1 and water did not show any column formation, but instead transitioned from bubble cluster formation directly to churn flow. The properties of the liquids, specifically the interfacial tension, density difference, and viscosity ratio were seen to be key factors which dictated the column formation and stability. The Kelvin-Helmholtz instability is one that arises when two fluids are in relative motion [98]. The instability occurs at the interface of the two fluids as a result of discontinuity in the tangential liquid velocity on either side of the interface. It is well known that interfacial tension will suppress Kelvin-Helmholtz instabilities to some extent [98]. Classically, this stability is defined for horizontal flows. However, in the case of liquid columns as described here, the vertical fluid flow at the outer boundary of the column presents a similar situation. Although not identical, the influence of interfacial tension acts similarly in regard to influencing instabilities at the outer column boundary. As a result, larger interfacial

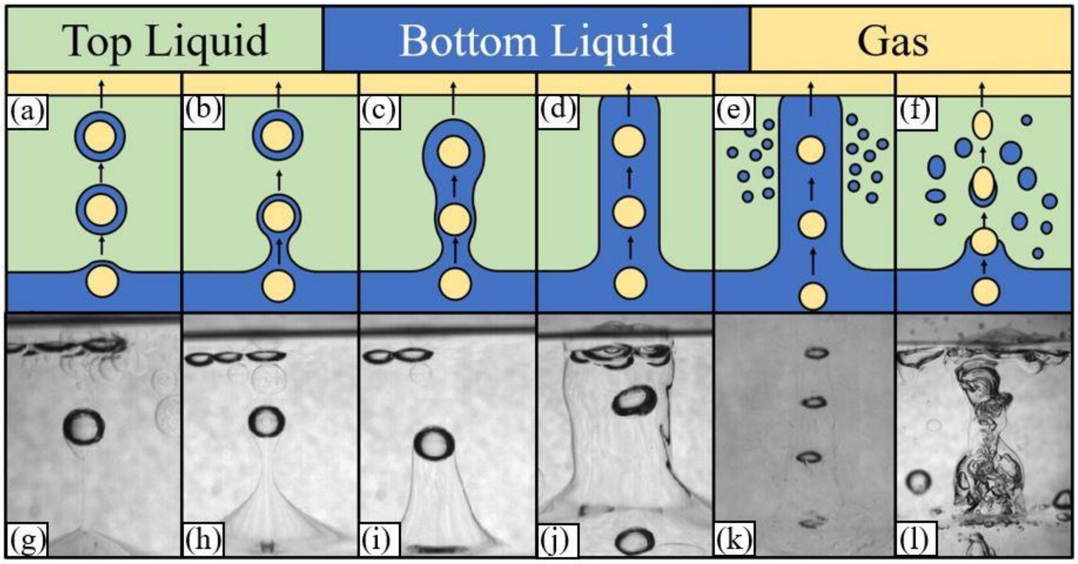

**Figure 29.** *Formation of a stable bubble column shown (a)-(d) schematically and (g)-(j) experimentally with water and silicone oil 10, unstable column formation shown (e) schematically and (k) as seen with silicone oil 20 and ethanol, and churn flow shown (f) schematically and (l) as seen with PP1 and water.*

tensions would aid in column stability. This is part of the reason why the silicone oil-ethanol combinations (low interfacial tensions) only formed unstable columns while the water-silicone oil combinations (high interfacial tensions) formed stable columns. However, as can be noted from the PP1-water combination, a high-interfacial tension is not the only requirement for stable column formation. With this liquid combination, the large difference in liquid density prevented any sort of stable column formation, even with the large interfacial tension. Any of the bottom liquid that was entrained behind the bubble as it passed through the interface drained back into the lower liquid bath very quickly, and thus, even the formation of short columns was hampered. The viscosity ratio was seen to play a role in dictating the width of the liquid column. For bubbles of similar size, velocity, and frequency, the column width generally increased with the lower liquid viscosity.

As with the single bubble regimes, physical characteristics of the bubble stream passage are identified which are able to yield dimensionless numbers to map the various flow regimes. In these regimes, bubble frequency has been accounted for by employing the superficial velocity, $V_s$, instead of the bubble velocity. This is given as:

$$V_s = \frac{\frac{\pi}{6}D^3 f}{\frac{\pi}{4}D^2} = \frac{2}{3}Df \tag{24}$$

where $f$ is the bubble frequency and $D$ is the undeformed bubble diameter. The first dimensionless number is derived through a comparison of the inertia carried by the bubble stream to the gravitational forces acting on the bottom liquid as it is carried over into the top liquid layer. From this, a modified Froude number is defined:

$$Fr^* = \frac{V_s}{\sqrt{gS\Gamma}} \tag{25}$$

where $\Gamma=(\rho_B-\rho_T)/\rho_B$ is the density difference between the two liquids normalized by the bottom liquid density, and the characteristic length is chosen to be the height of the top liquid layer, $S$. This height is chosen so the ratio represents the inertia of the bubble stream compared to the weight of a liquid column spanning the entire upper liquid layer. The modified Froude number has been shown previously to be proportional to the carryover volume in stratified liquid systems [99]. A higher $Fr^*$ indicates that a bubble stream is able to entrain a larger volume of liquid, and thus, increases the likelihood of a column being formed. As previously discussed, however, a bubble stream may not necessarily form a stable column even if it is able to carry over a sufficient volume of the lower liquid. Therefore, the second dimensionless number is used as a means to characterize the stability of the liquid-liquid interface during bubble stream passage. The bottom interfacial Weber number, as described by Equation 20, is employed to do so. Again, the superficial velocity is used in place of the bubble velocity to account for bubble frequency. For bubble streams, a high $We_{I,B}$ would indicate that the inertia of the bubbles induces a significant velocity gradient at the liquid-liquid interface which the interfacial tension is unable to suppress. Thus, instabilities would be generated at higher $We_{I,B}$ values. Furthermore, at lower frequencies when the column is not yet formed, this dimensionless number will still be indicative of the interface deformation, which will aid in delineating between the flow regimes seen at lower frequencies.

The experimental results are mapped with $Fr^*$ and $We_{I,B}$ for bubble streams as shown in Figure 30. The liquid-liquid interface stability tends to separate the regimes into upper and lower regions with the divide occurring at $We_{I,B}=40(Fr^*)^2$, as shown with the diagonal dashed line. Below this line, the interfacial tension tends to be higher and the liquid-liquid interface is better defined. Above the line, instabilities are likely to occur at the interface. In the lower Froude number region, the single bubble equivalent and partial column regimes are seen. When $We_{I,B}$ is also lower, i.e. the interface is more stable, the single bubble equivalent regime is seen, as shown by region 1 in green. At higher $We_{I,B}$ values, the interface is less stable and remains deformed longer and instead a partial column is formed, as shown by region 2 in red. As $Fr^*$ is increased, a transition to the bubble cluster regime, shown by region 3 in orange, is seen at lower $We_{I,B}$ numbers. This transition is observed when the Froude number is ~0.07. At higher $We_{I,B}$ values, the bubbles are able to pass through the interface more easily and, thus, do not cluster at the interface, and instead remain in the partial column regime. Once $Fr^*$ is high enough, the liquid carryover generated by the bubble stream is enough to form a column. At lower $We_{I,B}$ values, a stable column (region 4 in purple) is formed since the interfacial tension is able to suppress instabilities. This transition occurs when the Froude number is ~0.4. At higher $We_{I,B}$ values, the flow instead transitions to unstable columns (region 5 in blue) at a Froude number of ~0.15 due to the reduced interface stability. The last region of churn flow (region 6 in gray)

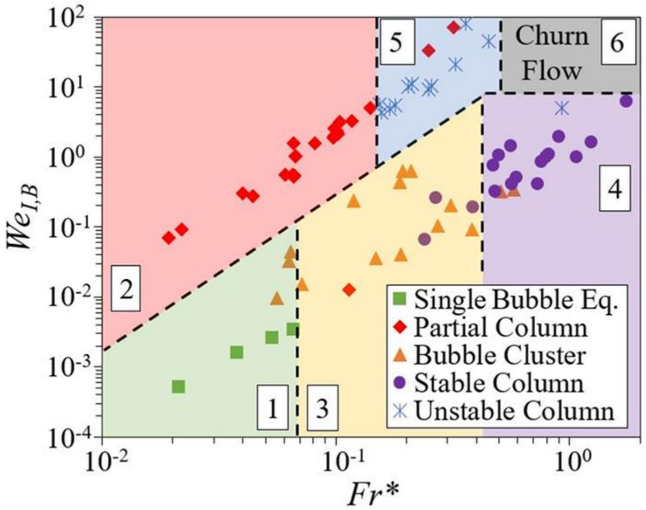

**Figure 30.** *Dimensionless flow map for bubble stream passage through a liquid-liquid interface.*

is seen at Froude numbers greater than ~0.5 and Weber numbers greater than ~8. The flow here was unfortunately too chaotic to obtain experimental measurements through video analysis.

## 4.2 Bubble Growth in an Immiscible Liquid Droplet

While there are a variety of chemical and biological applications where bubble passage through a liquid-liquid interface is relevant, its application for heat dissipation in direct contact evaporators was considered here. Customarily in this application, a droplet of an immiscible, volatile liquid is dispersed into another non-volatile liquid which is at a temperature greater than the saturation temperature of the volatile liquid. Under a sufficient superheat, nucleation occurs in the droplet followed by bubble growth within the droplet. A numerical bubble growth model for two phase droplets in an immiscible liquid was developed by solving the mass and energy conservation equations. The change in the bubble growth rate by solving the momentum conservation equation is shown to be minimal and has, therefore, been neglected. The growth rate of the vapor core due to evaporation of the liquid shell as heat is transferred from the hot bath is computed. The growth rate of the bubble is seen to be significantly different from the growth of a vapor bubble in a uniformly heated bath or the growth rate of a nucleating bubble on a heater surface.

### *4.2.1 Proposed Model*

The proposed geometry of the two-phase droplet in a bulk liquid and the relevant properties are shown in Figure 31. The evaporating liquid in the droplet is referred to as liquid 1, and the bulk liquid is referred to as liquid 2. The location of the liquid-vapor interface and the liquid-liquid interface are denoted by $R_1$ and $R_2$ respectively.

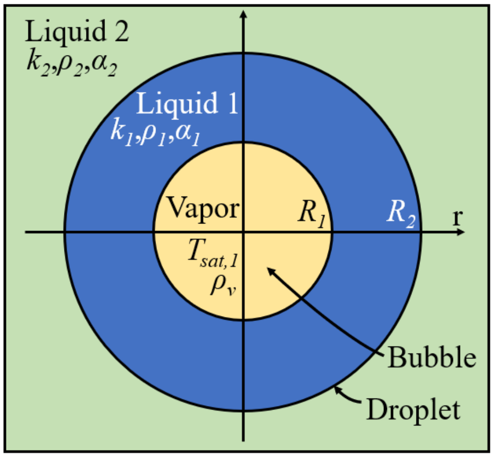

**Figure 31.** *Concentric model for bubble growth in an immiscible droplet.*

In addition to the assumptions commonly made to develop bubble growth models in infinite media, such as liquids being incompressible, saturation temperature of the evaporating liquid being constant throughout the bubble growth cycle, and properties of the liquids being constant, the current model employs two important assumptions: (i) the bubble grows from the center of the evaporating liquid droplet (liquid 1) and evaporation induced instabilities and oscillations are ignored, and (ii) there is no angular variation in the domain or the fluid temperatures (a 1D radial model is sufficient to describe the system). The effect of an eccentrically located bubble in the droplet is negligible since the thickness of the evaporating liquid rapidly decreases as the bubble begins to grow and effectively becomes a uniformly thin film around the bubble. The use of this geometry allows the implementation of the transient one-dimensional energy equation to describe the temperature profile in the droplet and bulk liquid as a function of radial location and time. A previous model proposed by Avedisian and Suresh [79], which employed this same geometry, simultaneously solved the continuity, energy, and momentum equations. The current model is instead obtained by solving only the continuity and energy equations. This significantly simplifies the model while maintaining its accuracy. The initial conditions before bubble growth begins are also modified by considering the temperature profile as a result of radial conduction within the two-phase droplet. These changes significantly impact the bubble growth profile and can provide a more realistic representation when a liquid droplet is introduced in another immiscible liquid. The continuity and energy equations in 1D radial coordinates are given by:

$$\frac{1}{r^2}\frac{\partial}{\partial r}(r^2 v) = 0 \tag{26}$$

$$\frac{\partial T_i}{\partial t} + v\frac{\partial T_i}{\partial r} = \alpha_i \frac{1}{r^2}\frac{\partial}{\partial r}\left(r^2 \frac{\partial T_i}{\partial r}\right) \tag{27}$$

where $i=1$ or $2$ denotes liquid 1 or 2, $v$ is the radial velocity, and $\alpha$ is the thermal diffusivity. Through conservation of mass, the radial velocity of the surrounding liquid, including the liquid-liquid interface and bulk liquid, may be written as a function of the liquid-vapor interface movement:

$$v(r,t) = \varepsilon \frac{R_1^2}{r^2}\frac{dR_1}{dt} \tag{28}$$

where $\varepsilon=1-\rho_v/\rho_1$, and $\rho_v$ and $\rho_1$ are the vapor and liquid density of liquid 1 respectively. A heat balance across the liquid-vapor interface yields the bubble growth rate as:

$$\frac{dR_1}{dt} = \frac{k_1}{\rho_v h_{fg}}\frac{\partial T_1}{\partial r}(R_1,t) \tag{29}$$

where $k_1$ and $h_{fg}$ are the thermal conductivity and latent heat of vaporization of liquid 1. An initial vapor core size, $R_{1,0}$, is assumed to be a known value. The boundary conditions during bubble growth are as follows:

$$\begin{gathered} T_1(R_1,t) = T_{sat,1} \qquad T_1(R_2,t) = T_2(R_2,t) \\ k_1\frac{\partial T_1}{\partial r}(R_2,t) = k_2\frac{\partial T_2}{\partial r}(R_2,t) \qquad T_2(\infty,t) = T_\infty \end{gathered} \tag{30}$$

where $T_{sat,1}$ is the saturation temperature of liquid 1, and $T_\infty$ is the bulk liquid temperature far from the droplet.

The primary challenge in solving this type of problem stems from the moving boundary conditions for the temperature profile at the liquid-vapor and liquid-liquid interfaces. To overcome this, a coordinate transformation known as the Landau immobilization is used to pin the boundary conditions to a single dimensionless location [79,100]. This transformation is shown in Figure 32 and expressed as:

$$\eta = \frac{r - R_1(t)}{R_2(t) - R_1(t)} \tag{31}$$

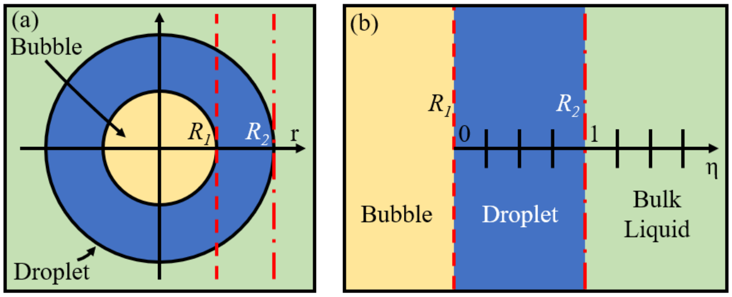

**Figure 32.** *Coordinate transformation to immobilize boundary conditions.*

This technique fixes the liquid-vapor interface at *η*=0 and the liquid-liquid interface at *η*=1, thereby normalizing the effect of thinning of the evaporating liquid domain. Additionally, the following dimensionless quantities are introduced:

$$\bar{R}_i = \frac{R_i}{R_{2,0}} \qquad \bar{r} = \eta(\overline{R_2} - \overline{R_1}) + \overline{R_1} \qquad \bar{T}_i = \frac{T_i - T_{sat,1}}{T_\infty - T_{sat,1}}$$
$$\tau = \frac{t\alpha_1}{R_{2,0}^2} \qquad \gamma = \frac{\alpha_2}{\alpha_1} \qquad \zeta = \frac{k_2}{k_1} \qquad Ja = \frac{\rho_1 C_{p,1}\left(T_\infty - T_{sat,1}\right)}{\rho_v h_{fg}} \tag{32}$$

where $R_{2,0}$ is the initial droplet radius, $C_{p,1}$ is the specific heat of liquid 1, *Ja* is the Jakob number of liquid 1, and all other variables are as previously defined. Using the coordinate transformation and these dimensionless quantities, the energy equation may be written as:

$$(\overline{R_2} - \overline{R_1})\bar{r}^2 \frac{\partial \bar{T}_i}{\partial \tau} + \frac{\partial \bar{T}_i}{\partial \eta}\frac{\partial \overline{R_1}}{\partial \tau}\left\{\left[\frac{\bar{r}^3\left(\overline{R_2}^2 - \varepsilon\overline{R_1}^2\right) - \bar{r}^2\left(\overline{R_2}^3 - \varepsilon\overline{R_1}^3\right)}{\overline{R_2}^2(\overline{R_2} - \overline{R_1})}\right] + \varepsilon\overline{R_1}^2\right\}$$
$$= \beta_i \frac{\partial}{\partial \eta}\left(\frac{\bar{r}^2}{\overline{R_2} - \overline{R_1}}\frac{\partial \bar{T}_l}{\partial \eta}\right) \tag{33}$$

$$\beta_1 = 1 \tag{34}$$

$$\beta_2 = \gamma \tag{35}$$

Equation 30 is transformed to give the dimensionless boundary conditions as:

$$\begin{array}{ll} \overline{T_1}(0,\tau) = 0 & \overline{T_1}(1,\tau) = \overline{T_2}(1,\tau) \\ \dfrac{\partial \overline{T_1}}{\partial \eta}(1,\tau) = \zeta \dfrac{\partial \overline{T_2}}{\partial \eta}(1,\tau) & \overline{T_2}(\infty,\tau) = 1 \end{array} \tag{36}$$

The liquid-vapor interface heat balance, Equation 29, becomes:

$$\frac{\partial \overline{R_1}}{\partial \tau} = \frac{Ja}{\overline{R_2} - \overline{R_1}} \frac{\partial \overline{T_1}}{\partial \eta}(0,\tau) \tag{37}$$

Using Equation 28, the liquid-liquid interface movement may be written as:

$$\frac{\partial \overline{R_2}}{\partial \tau} = \varepsilon \frac{\overline{R_1}^2}{\overline{R_2}^2} \frac{\partial \overline{R_1}}{\partial \tau} = \varepsilon \frac{\overline{R_1}^2}{\overline{R_2}^2} \frac{Ja}{\overline{R_2} - \overline{R_1}} \frac{\partial \overline{T_1}}{\partial \eta}(0,\tau) \tag{38}$$

The initial conditions for these are simply $\overline{R_{1,0}}=R_{1,0}/R_{2,0}$ and $\overline{R_{2,0}}=1$ for the liquid-vapor and liquid-liquid interfaces, respectively.

The heat transfer model outlined here consists of a system of dependent partial and ordinary differential equations. In order to solve this system, Equations 33, 37, and 38 were discretized in the $\eta$ domain using second order derivative approximations. Thus, the problem is reduced to a system of dependent ordinary differential equations which were solved simultaneously using ode15s in Matlab with the boundary conditions as described. The initial temperature conditions are discussed in detail in Section 4.2.2. The Matlab code written for this model is presented in Section 7.2 of the appendix. The solution yields the temporal evolution of the temperature profile in the droplet and surrounding liquid, the bubble growth rate, and the movement of the liquid-liquid interface. The simulation was stopped when the thickness of the evaporating liquid shell reached 1 μm.

### *4.2.2 Initial Temperature Profile*

The initial temperature profile in the droplet and the bulk liquid prior to the onset of bubble growth is determined by solving the 1D radial heat conduction equation, i.e. Equation 27 with $v=0$. It is assumed that the droplet is introduced into the bulk liquid at a constant subcooled temperature, $T_0$, and must undergo an initial heating period prior to the onset of bubble growth. An axisymmetric condition is applied at the center of the droplet such that the first spatial derivative of the temperature profile is equal to zero. The temperature far away from the liquid-liquid interface in the bulk is assumed to remain constant. The liquid-liquid interface boundary condition is determined by the degree of convective heat transfer at this boundary. If the density difference between the two liquids is low, the rate of droplet rise/drop will be negligible, and conduction will be the principle mode of heat transfer. In such a case, the liquid-liquid interface temperature can de determine through the heat conduction equation. Alternatively, if the density difference between the two liquids is high, the contribution of convective heat transfer is greater, and the liquid-liquid interface can be assumed to be constant at bulk temperature. The two cases represent the lower and upper limits, respectively, of temperature at the liquid-liquid interface. For the current work, FC-72 is used as the evaporating liquid, and water is used as the bulk liquid. Since the specific weight of FC-72 is 1.68, it sinks rapidly when introduced in water. Therefore, the temperature at the liquid-liquid interface is assumed to be constant at bulk temperature during the wait time.

Bubble growth is taken to begin when the temperature at the droplet center reaches a certain degree of superheat above the saturation temperature of liquid 1, $T_s=T_{r=0}-T_{sat,1}$. This differs from the initial conditions in the model proposed by Avedisian and Suresh [79], in which a uniform superheat throughout the droplet, the same as that in the surrounding liquid, is assumed. In the present context, this is the same as setting $T_s=T_\infty-T_{sat,1}$. The value of this superheat is dependent on the experimental conditions. If a subcooled droplet is suddenly exposed to the bulk liquid, it is likely that nucleation and boiling will begin before the entire droplet reaches the bulk liquid temperature. A counter to this can be seen in the experiments of Haustein et al. [78], in which the droplet is introduced into a pressurized system. At the elevated pressure, the bulk liquid does not exceed the corresponding saturation temperature of the droplet. The droplet is able to reach a uniform temperature the same as the bulk liquid, and the system is then rapidly depressurized to initiate the boiling process. In such a system, the initial droplet temperature is likely much closer to being uniformly superheated when boiling begins.

The bubble nucleation and its location within the droplet has been studied by many researchers [72,101]. Nucleation is believed to occur at, or near, the liquid-liquid interface since the liquid near the interface is at a higher temperature compared to further inside the droplet. The initial nucleated bubble is a mixture of the vapor of the evaporating liquid and condensed gasses and, therefore, can remain within the droplet even if it is surrounded by subcooled liquid during the initial heating period. Any eccentricities in the initial location of the vapor bubble become insignificant as the bubble begins to grow. This is because the large difference between the liquid and vapor densities leads to rapid growth of the bubble with a small amount of the liquid evaporating and, as a result, the evaporating liquid becomes a thin film surrounding the vapor bubble. For the present model, it is assumed that a small vapor bubble, $R_{1,0}=10^{-2}$ mm, appears at the droplet center when it reaches the prescribed superheat. Alternatively, if the droplet has a preexisting vapor core, this value could also be used for $R_{1,0}$.

The heat conduction equation, i.e. Equation 33 with $\partial\overline{R_1}/\partial\tau=0$, is solved to determine the initial temperature profile using the partial differential equation solver in Matlab, pdepe. The model is stopped once the temperature at the center of the drop reaches the prescribed superheat, $T_s$. The initial temperature profile for boiling is then taken to be the temperature profile found between $R_{1,0}$ and the far field boundary at this time. Figure 33 shows a typical evolution of the temperature profile in a 0.5 mm radius FC-72 droplet initially at 22°C surrounded by water at 75°C. In this example, $T_s$=5°C so the simulation is run until the temperature at the center of the droplet reaches 5°C above the saturation

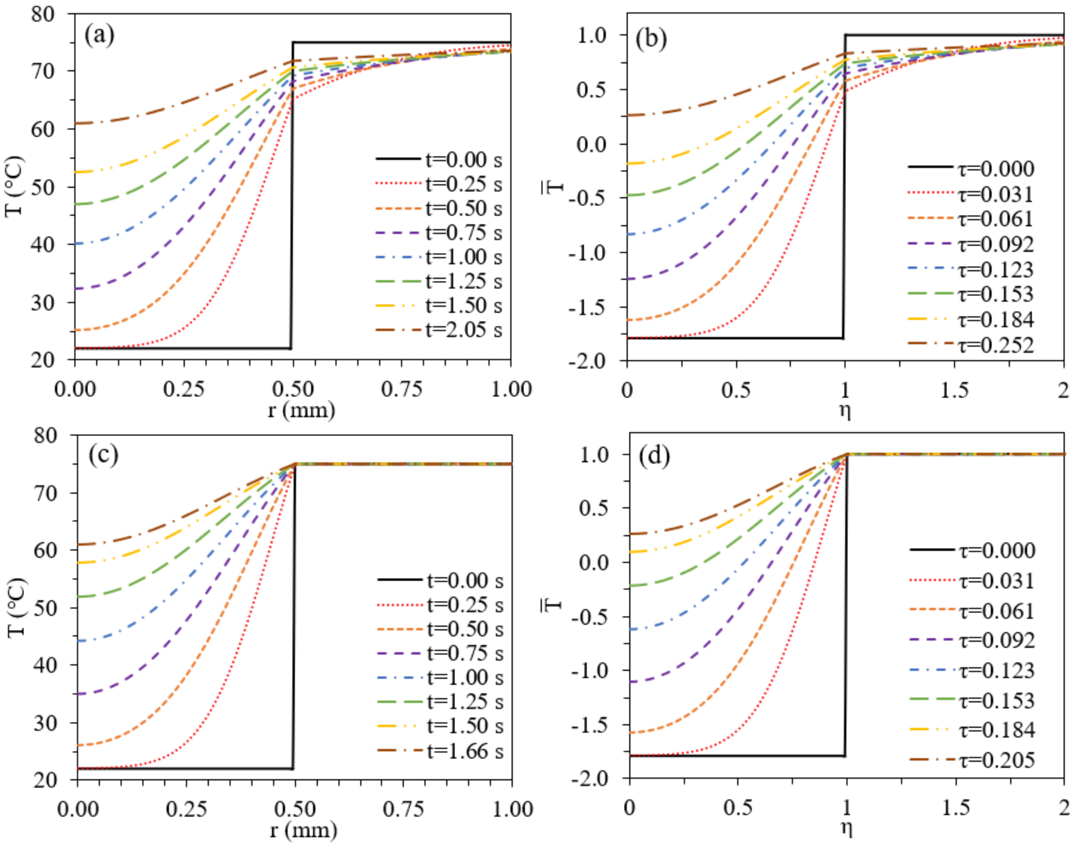

**Figure 33.** *Temperature profile in dimensional and dimensionless coordinate systems for (a)-(b) variable liquid-liquid interface temperature and (c)-(d) constant liquid-liquid interface temperature.*

temperature of FC-72. If the liquid-liquid interface temperature is transient, it takes 2.05 s for this criterion to be met while it takes only 1.66 s if the liquid-liquid interface temperature remains constant.

### *4.2.3 Results*

<u>*Effect of ignoring momentum conservation equation:*</u> The current work significantly simplified the bubble growth model by assuming that the effect of pressure difference driven bubble growth is negligible, i.e. not using the momentum equation. To justify this, the results using the current simplified model are compared with those presented by Avedisian and Suresh [79]. Figure 34 shows the dimensionless representation of bubble growth for an n-octane droplet in glycerine. The degree of superheat is represented by the Jakob's number, which is fixed at 10. The droplet is assumed to initially be at a constant superheat, as was done in the previous model. A comparison between results using both models showing the influence of ζ (thermal conductivity ratio) and γ (thermal mass ratio) are shown in Figure 34(a) and (b), respectively. The plots show the dimensionless bubble growth over time for variations in these two ratios. The growth rate from the current model closely matches the growth rate reported by Avedisian and Suresh. The inertia-controlled regime of bubble growth is dominant up to $\tau$ of $10^{-6}$ [79], which is less than 1% of the total bubble growth time and, therefore, can be ignored.

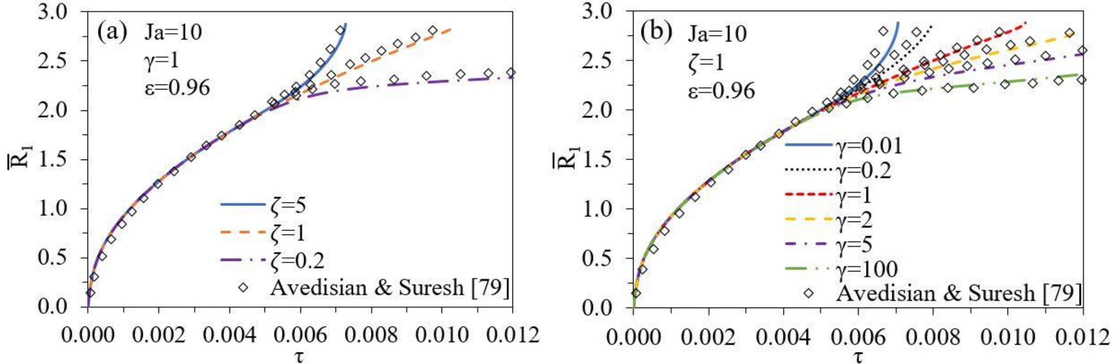

**Figure 34.** *Comparison of (a) ζ effect and (b) γ effect on bubble growth using the current model and previous described by Avedisian and Suresh [79].*

*Effect of initial temperature profile:* Variations in the initial temperature profile in the droplet have a substantial effect on bubble growth rate. For the same liquid combination, $T_s$ (the superheat reached at the droplet center prior to nucleation) is the primary parameter which controls this profile. To demonstrate the effect of $T_s$, simulations were run for a 0.5 mm radius FC-72 droplet initially at 22°C immersed in water at 76°C. The initial temperature profiles and subsequent bubble growths were found for various values of $T_s$. Figure 35(a) shows different initial temperature profiles with varying values of $\overline{T}_s = T_s/(T_\infty - T_{sat,1})$, while 35(b) depicts how this initial temperature profile affects the subsequent bubble growth rate. In the case of a uniformly superheated droplet ($\overline{T}_s$=1), like that considered by Avedisian and Suresh [79], the growth rate is highest in the initial period of bubble growth since superheated liquid is present at the liquid-vapor interface. As the temperature gradient at the liquid-vapor interface decreases, the bubble growth rate also decreases before finally increasing due to the thinning of the evaporating liquid layer. As $\overline{T}_s$ is decreased, the initial period of explosive bubble growth is also reduced. In the case where no superheat is required for nucleation, i.e. $\overline{T}_s$=0, the bubble growth rate is initially low since the temperature gradient at the liquid-vapor interface is very small. The growth rate steadily

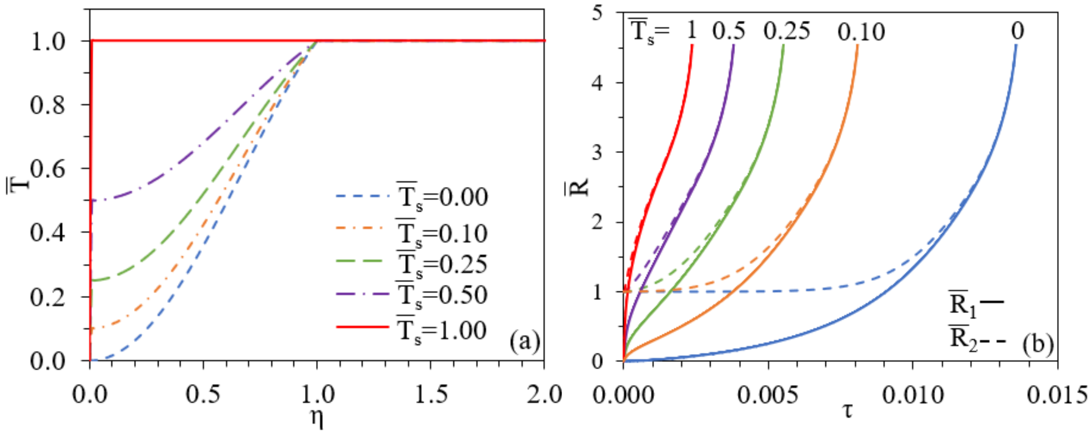

**Figure 35.** *Impact of* $\overline{T}_s$ *on (a) dimensionless initial temperature profile, and (b) dimensionless bubble growth.*

increases as the temperature gradient increases due to conduction and the thinning of the evaporating liquid shell. Additionally, it can be seen that the time for complete evaporation assuming uniformly superheated liquid is about 80% lower than the predicted growth time using no required initial superheat. This is because the average temperature of the droplet prior to bubble growth is lower in the latter, and there is no initial explosive bubble growth.

*Experimental validation:* The experimental setup discussed in Section 3.2 was used to experimentally capture bubble growth in an FC-72 droplet in a bath of heated water. The FC-72 droplet was introduced at a temperature of 22°C into water at two different temperatures of 90°C and 72°C. This represents a superheat of 34°C and 26°C, respectively, relative to the properties of FC-72. Figure 36(a) shows bubble growth within an FC-72 droplet where the surrounding water temperature was 90°C. The first frame is the droplet just at the onset of bubble growth, and the last frame shows the droplet after complete evaporation. The growth of the vapor is rapid compared to the velocity of the droplet in the bulk liquid and, therefore, the entire bubble growth process occurs with relatively small vertical displacement of the bubble. Upon complete evaporation of the droplet, the bubble rises up through the liquid. Since the liquid-vapor interface cannot be visualized, the liquid-liquid interface ($R_2$) was tracked to compare with the droplet radius predicted by the current model. The relevant liquid properties in Table 4 were used to model the bubble growth in present experiments as well as those found in literature. Since the specific weight of FC-72 is 1.68, it sinks when introduced in water. Therefore, the temperature at the liquid-liquid interface is assumed to be constant at the bulk temperature during the initial heating period. The value of $T_s$ ($\overline{T_s}$) was set to 3.7°C (0.11) and 9°C (0.56) when modeling experiments conducted with bulk water temperature at 90°C and 72°C,

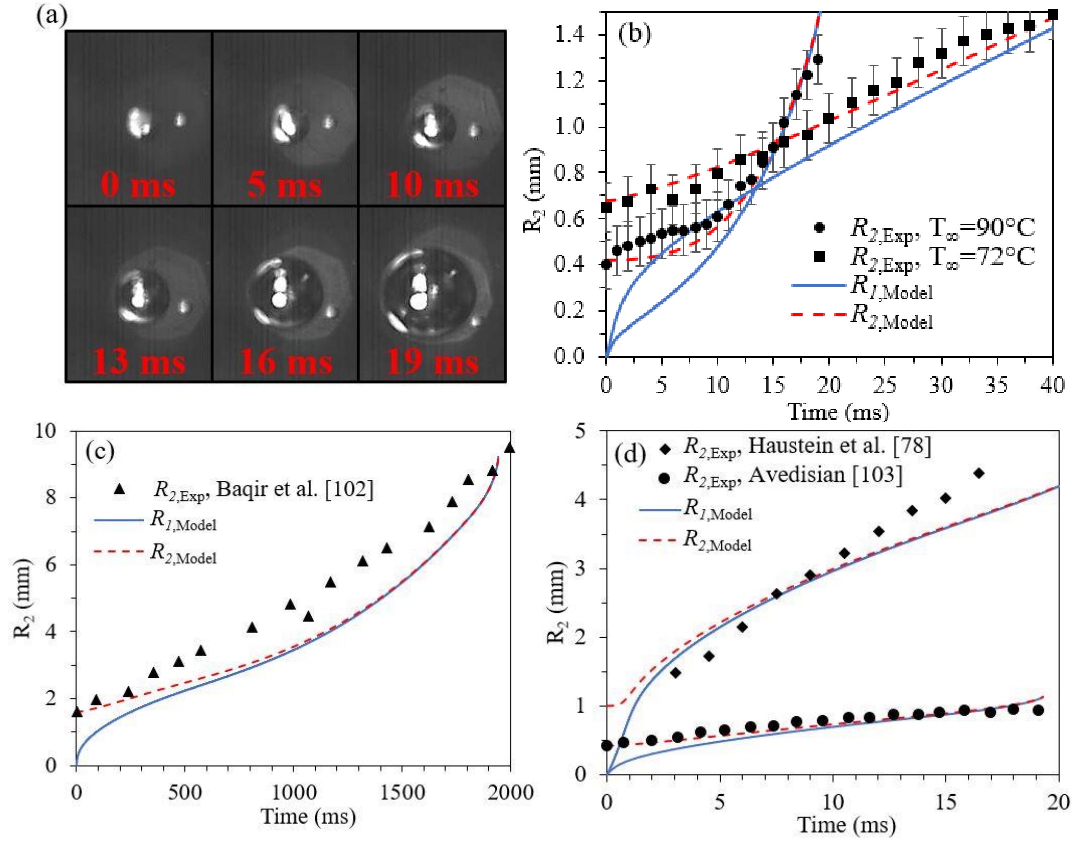

**Figure 36.** *(a) High speed visualization of bubble growth within an FC-72 droplet at a superheat of 34°C and experimental versus predicted bubble growth for (b) current experiments and (c and d) experiments found in literature.*

respectively. Figure 36(b) shows the present experimentally determined droplet radius and the predicted droplet diameter using the current model. It can be seen that the current model closely matches the experimentally observed growth rates. A comparison to several experiments found in literature is also shown in Figure 36(c) and (d). Baqir et al. [102] employed n-pentane drops in water, Haustein et al. [78] used propane in water, and Avedisian [103] implemented n-octane droplets in glycerine. A constant liquid-liquid interface temperature was also assumed for these when determining the initial temperature profile. The value of $T_s$ ($\overline{T}_s$) used for each was 4°C (1.00), 72°C (1.00), and 35°C (0.87), respectively. Once again, the model is able to predict the bubble growth with reasonable accuracy.

**Table 4.** *Liquid properties used in immiscible bubble growth model.*

| Property | Water | FC-72 | n-Pentane | Propane | n-Octane | Glycerine |
|---|---|---|---|---|---|---|
| $T_{sat}$ (°C) | - | 56 | 36 | -42 | 212 | - |
| $\rho_l$ (kg/m$^3$) | 980 | 1594 | 610 | 483 | 516 | 944 |
| $\rho_v$(kg/m$^3$) | - | 13.0 | 3.0 | 1.8 | 25.1 | - |
| $k$ (W/m·K) | 0.591 | 0.054 | 0.107 | 0.019 | 0.076 | 0.353 |
| $C_p$ (J/kg·K) | 4180 | 1101 | 2340 | 1707 | 3104 | 4998 |
| α (mm$^2$/s) | 0.144 | 0.031 | 0.075 | 0.023 | 0.047 | 0.075 |
| $h_{fg}$ (kJ/kg) | - | 88 | 358 | 428 | 229 | - |

*Parametric study:* Having validated the proposed model, a study is carried out to identify the influence of superheat to which the droplet is subjected, fluid properties, and initial droplet configuration on bubble growth. Unless otherwise noted, the properties of liquid 1 and liquid 2 were taken to be that of FC-72 and water, respectively, $R_{1,0}$ was set to $10^{-2}$ mm, the liquid-liquid interface temperature was assumed constant at the bulk liquid temperature during the initial heating period, and $T_s$ was set to zero for the purpose of the parametric study. Figure 37 shows the effect of the degree of superheat on bubble growth rate. A droplet subjected to a superheat of 5°C takes ~450 ms to evaporate, while a droplet subjected to a superheat of 40°C fully evaporates in ~50 ms. The difference in growth rate is greatest in the initial phase of bubble growth when the temperature gradient at the liquid vapor interface is low. As the bubble grows, the growth rates become less dependent on the superheat.

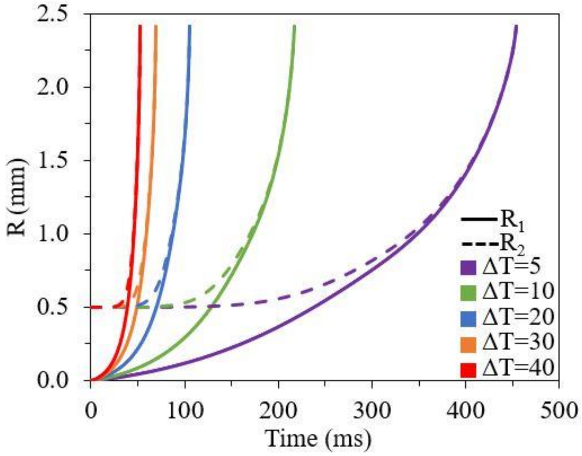

**Figure 37.** *Effect of liquid superheat on bubble growth.*

Another parameter that affects the growth rate of a bubble in a two-phase droplet for a given liquid combination is the initial distance between the liquid-vapor interface and the liquid-liquid interface, i.e. the initial thickness of the evaporating liquid shell. While the growth time is expected to increase as the volume of the evaporating liquid in the droplet increases, the effect of varying initial shell thickness on bubble growth rate for a constant volume of evaporating liquid (liquid 1) provides interesting insight. The initial thickness of the shell is characterized by the dimensionless term $\overline{h_0}=(R_{2,0}-R_{1,0})/R_{2,0}$. Figure 38 shows the dimensionless plot of bubble radius over time corresponding to various $\overline{h_0}$ values. As the dimensionless shell thickness decreases from 1 to 0.8, the time taken to reach complete evaporation is seen to increase. As the dimensionless shell thickness is further decreased, the time to complete evaporation then decreases dramatically. Since both the liquid-liquid and liquid-vapor contact area are changing, this behavior may be a result of changing surface area to liquid volume ratio.

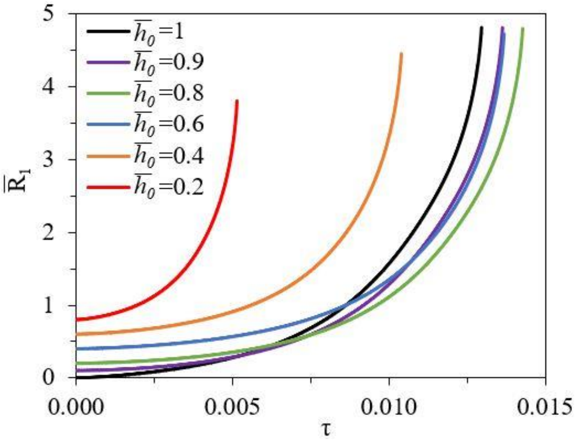

**Figure 38.** *Influence of initial shell thickness on dimensionless bubble growth.*

The properties of the evaporating liquid (liquid 1) and the bulk liquid (liquid 2) also have a significant effect on the bubble growth rate. One of the key parameters that affects bubble growth rate is the thermal conductivity of the two liquids and is characterized by the dimensionless term ζ, which is the ratio of the thermal conductivity of the bulk liquid to the evaporating liquid. Figure 39 shows the dimensionless bubble growth over time for different ζ values. A ζ value of 10.4 corresponds to the thermal conductivity ratio of water and FC-72. In the initial phase of bubble growth, the thermal conductivity ratio does not have any impact on the bubble growth rate since the thermal boundary layer is within the droplet (liquid 1). As the bubble continues to grow, the thermal boundary layer grows into the bulk liquid and can result in significant variation in bubble growth rate. The temperature gradient at the liquid-liquid interface is a function of ζ. When ζ>1 the temperature gradient in the bulk liquid (liquid 2) is lower than the evaporating liquid (liquid 1). As a result, the temperature at the liquid-liquid interface remains higher when ζ>1 which, in turn, results in a higher temperature gradient in the droplet (liquid 1). However, when the thermal conductivity of the bulk liquid is lower than the evaporating liquid, i.e. ζ<1, the growth rate of the bubble reduces since the temperature at the liquid-liquid interface also reduces sharply. These trends are not significantly influenced by variations in the initial temperature profile.

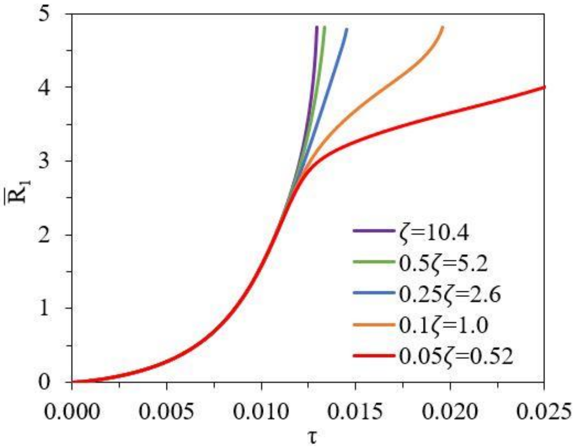

**Figure 39.** *Influence of ζ on immiscible bubble growth.*

Finally, the effect of the thermal mass (product of density and specific heat) ratio of the two liquids was investigated. This was done by using a constant value of ζ while varying the thermal diffusivity ratio, γ. A γ value of 4.7 corresponds to that of water and FC-72.

Figure 40 shows the effect of thermal mass for the two initial heating conditions: (a) constant liquid-liquid interface temperature and (b) variable liquid-liquid interface temperature, respectively. When the liquid-liquid interface is maintained at a constant temperature, the effect of thermal mass variation is small. As the thermal mass ratio increases (lower thermal diffusivity ratio), the temperature of the interface remains higher, and therefore, the growth rate is higher. When the thermal mass of the bulk liquid is lower than the evaporating liquid, the reduction in interfacial temperature is larger, and hence, the bubble growth rate reduces at larger diameters. The role of the thermal mass on bubble growth rate is more pronounced when the liquid-liquid interface temperature is variable during the initial heating period. Under this condition, the temperature of the liquid-liquid interface at the onset of bubble growth is significantly affected by γ. As a result, the temperature gradient within the droplet in the initial stages of bubble growth varies considerably, affecting the growth rate from the initial stages of bubble growth. When γ<1, the temperature of the interface reduces well below the bulk temperature and hence the bubble growth rate is lower. For γ>1, the reduction in the liquid-liquid interface temperature is small, and the bubble growth rates are similar to those seen in Figure 40(a).

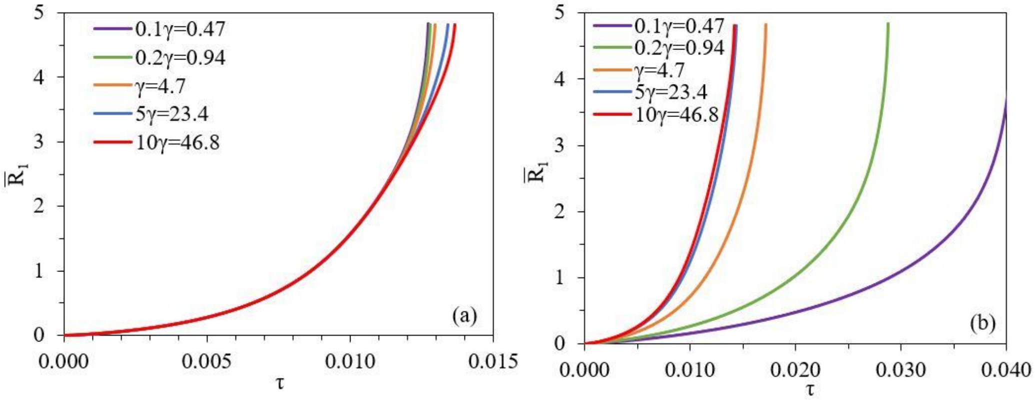

**Figure 40.** *Influence of γ on bubble growth when the liquid-liquid interface during initial heating is (a) constant and (b) variable.*

## 4.3 Dimensionless Characterization of Bubble Collisions

As with bubble collisions at a liquid-liquid interface, bubble collisions with a free or solid surface induce the formation of a thin liquid film between the bubble and the surface. This film is not uniform in thickness but instead takes on an axisymmetric dimpled shape, as shown in Figure 41, with the maximum film thickness being at the axis of symmetry and the minimum film thickness bring some distance away from this axis at what is referred to here as the film radius. The film drainage rate is influenced by a number of factors such as bubble size and impact velocity [62,104,105], liquid viscosity [106], surfactants [85,107–109], and radial film size [52,55,57]. Manev et al. [57] determined that film thickness non-homogeneities appear at film radii larger than a certain transition radius beyond which the thinning rate is inversely proportional to the film radius to the power of 4/5, and below this radius the thinning rate is inversely proportional to the film radius squared. Under either condition, film radius is instrumental in determining the film thinning rate, and thus, is a key parameter in characterizing the collision process. Zawala and Malysa [62] predicted film radius for a free surface collision using the bubble kinetic energy. However, these predicted values were over two times the actual bubble radius in some cases. Currently,

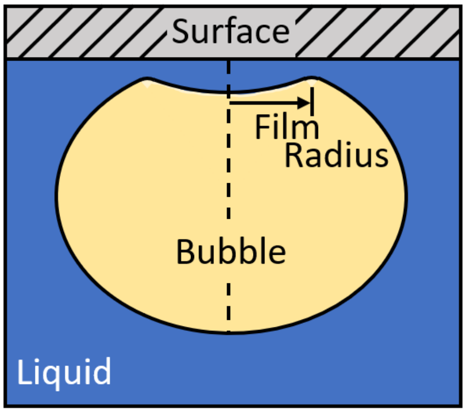

**Figure 41.** *Schematic of a bubble collision with a solid surface.*

there exists no simple and accurate means to theoretically predict or experimentally capture the film radius during dynamic bubble collisions.

It was hypothesized that a dimensionless representation of the collision process would enable the prediction of the film radius. The following steps are taken to do so: (i) Buckingham pi theorem is used to identify relevant dimensionless groups, (ii) previously established and experimentally validated numerical models are used to generate data, (iii) simulation results are used to relate the dimensionless groups, and (iv) a relationship between film radius and the dimensionless groups is established. To validate the film radius prediction, experiments were carried out using interferometry to capture the film radius during the collision of a bubble with a glass surface. Unfortunately, there is currently no technique capable of capturing the film radius during bubble collision with a free surface. As such, we are left to rely on the accuracy of the numerical model implemented to generate data. This work enables a more in-depth characterization and understanding of the dynamic thinning process during bubble impact with a free or solid surface.

### *4.3.1 Experimental Film Radius Measurement*

Experimental tests were carried out to capture the collision of 0.95 mm radius bubbles with a glass surface in water using the experimental setup previously described in Section 3.3. The distance between the needle tip where the bubble was formed and the glass surface, $L$, was varied to change the velocity with which the bubble would impact the glass surface. Four different distances were tested: $L$=33, 8.1, 4.1 and 2.7 mm. At each distance, experiments were performed 3-5 times to ensure repeatability. Bubble trajectory during the collision was captured using high-speed imaging, and film radius measurements were taken using an interferometry system which captured the bubble collisions from above. A typical sequence of images displaying the collision of a bubble with *L*=4.1 mm is shown in Figure 42. The bubble collides and bounces away from the wall five times at 22, 48, 70, 88, and 104 ms. With each subsequent bounce, the bubble rebounds a shorter distance. During its rebound from the fifth collision, the thin liquid film between the bubble and the glass surface ruptures at 108 ms, and three-phase contact formation occurs.

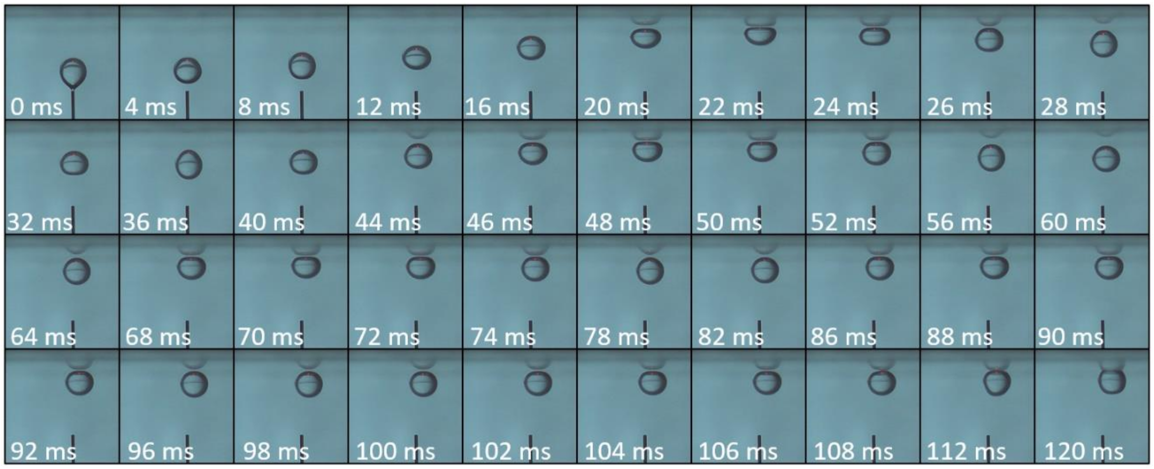

**Figure 42.** *Sequence of images showing the collision of a bubble with a glass surface. Initial distance between the needle tip and surface is 4.1 mm.*

The trajectories of four bubbles released from different distances from the solid surface are shown in Figure 43. Location measurements were taken from the bubble center. For the closer distances of *L*=8.1, 4.1, and 2.7 mm, time *t=0* corresponds to when the bubble is first released from the needle. The impact velocity from these distances was measured to be 28.0, 18.5, and 12.4 cm/s, respectively. For the farther distance of *L*=33 mm, time *t=0* corresponds to when the bubble center first came into frame. In this instance, the bubble impacted the glass surface at terminal velocity of 35.0 cm/s. The results found here are consistent with those found in previous studies on bubble collisions with a solid surface [93,110]. Bubbles released farther away from the surface, which impact at a higher velocity, rebound a greater distance than those released close to the surface. Additionally, bubbles released farther from the surface also bounced more times prior to film rupture and three-phase contact formation. The reasoning behind this has been explained previously by Zawala et al. [93]. A larger impact velocity increases the radial size of the thin liquid film formed between the bubble and surface. Since the film drainage rate is inversely proportional to the film size, larger films will drain slower, thus inhibiting rupture and enabling bouncing to occur. A theoretical solution for the bubble trajectory from Manica et al. [53,111] for *L*=4.1 mm is also included for comparison. This model will be described later in more detail in Section 4.3.3. As previously demonstrated, this model is very accurate in predicting the bubble trajectory. Furthermore, the model is able to predict the spatiotemporal evolution of the film thickness, which will later aid in defining a prediction for the film radius.

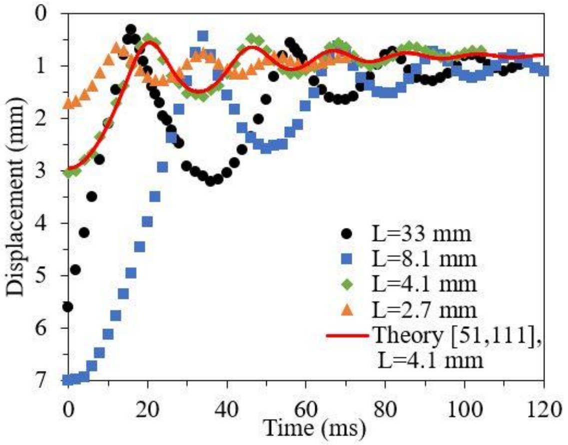

**Figure 43.** *Variation in bubble trajectory with change in distance between needle tip and glass surface, L.*

A typical sequence of interference patterns captured during the third collision of a bubble with *L*=4.1 mm is shown in Figure 44, where the scale bar in the first image is 0.25 mm. During the collision, this film radius grows as the bubble impacts the surface and decelerates, as shown in the first three frames of Figure 44. As the bubble rebounds, the film radius then decreases as shown in the last three frames of Figure 44. Although the film is typically assumed to be axisymmetric, some discrepancies in this assumption can be seen in the figure. This is believed to be a result of the bubble oscillations which occur between collisions when the bubble rebounds from the surface. These oscillations induce small discrepancies in the initial film symmetry of later bounces as demonstrated in the first two frames of Figure 44. However, the symmetry remains at middle stages of the collision process when the film radius is at its maximum. The individual interference bands sometimes became indistinguishable due to noise and the fast-changing nature of the film, but the outer boundary of these interference patterns, where the film radius is located, always remained clear. Very high frame rates (54,000 fps in previous studies [9,51]), which are not achievable with the current experimental setup, are required to capture the movement of individual interference bands. Since the present work focuses only on film radius and not on absolute film thickness values, these images remain appropriate for this study since the film radius location remained clear throughout the collision.

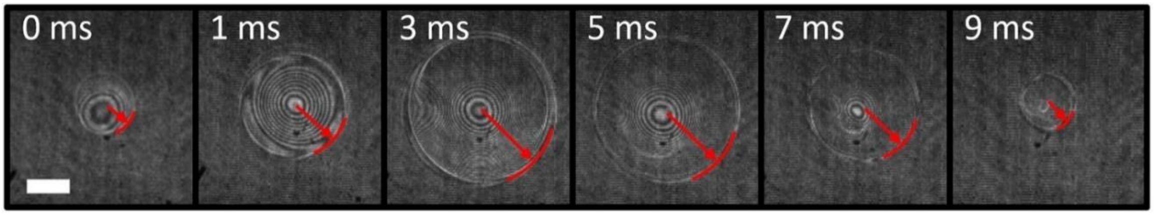

**Figure 44.** *Interference patterns formed during the third collision of a bubble with a glass surface where L=4.1 mm. Scale bar in first image is 0.25 mm.*

To further demonstrate that the outer edge of the interference patterns is indeed the location of the film radius, a typical rupture sequence captured in experiment is shown in Figure 45 along with a schematic of the process. As previously demonstrated, the film rupture takes place at the dimple rim, i.e. at the film radius where the film is thinnest [9]. In the series shown in Figure 45, the rupture point can be seen to start at the bottom outer edge of the interference patterns, which indicates that the outer boundary of the interference patterns is where the film radius is located. In every video captured, the rupture began at this outer boundary. After the initial rupture, the three-phase contact region quickly grew towards the center of the film. This dewetting process is roughly 100 times faster than the film drainage process [9].

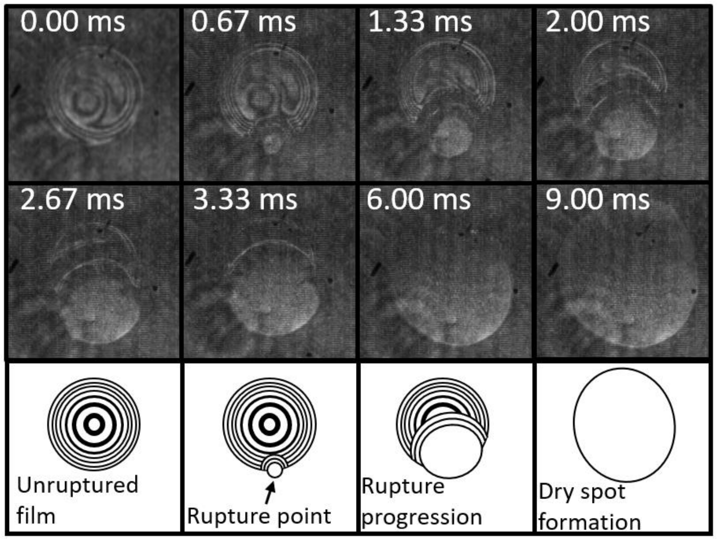

**Figure 45.** *Evolution of film rupture and three-phase contact formation.*

As previously noted, the film radius is not constant, but varies over the course of each bubble collision. The current work focuses on the maximum value that this film radius reaches during each impact. Figure 46 shows the interference pattern found during four subsequent collisions, with *L*=4.1 mm, at the time in which the film radius attained its maximum. With each subsequent collision the film radius (shown with the overlaid arc and arrow) decreases as expected since the bubble is impacting the glass surface with a reduced velocity in later bounces. This maximum film radius value was measured during the first four bounces of bubbles impacting the glass surface from different distances. The average maximum film radius value reached during these collisions over repeated tests is shown in

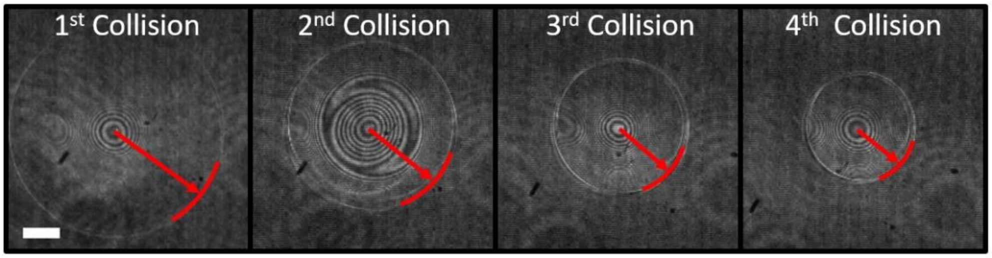

**Figure 46.** *Interference patterns in subsequent collisions of a bubble with a glass surface where L=4.1mm. Scale bar is 0.25mm.*

Table 5. Two trends are easily identified from this table. First, the film radius decreases with subsequent bounces as previously noted. Second, the film radius also decreases with decreasing values of $L$. Again, this is to be expected since bubbles released closer to the surface impact with a lower velocity than those released farther away.

**Table 5.** *Average maximum film radius attained during subsequent bubble collisions released from varying distance from a glass surface.*

| Collision Number | Average Maximum Film Radius, $R_F$ (mm) | | | |
|---|---|---|---|---|
| | $L$=33 mm | $L$=8.1 mm | $L$=4.1 mm | $L$=2.7 mm |
| 1st | 1.16 | 1.02 | 0.86 | 0.64 |
| 2nd | 0.75 | 0.71 | 0.67 | 0.50 |
| 3rd | 0.58 | 0.58 | 0.53 | 0.41 |
| 4th | 0.48 | 0.47 | 0.43 | 0.37 |

### *4.3.2 Identification of Relevant Dimensionless Groups*

During bubble collision, a pressure buildup in the thin liquid film formed between the bubble and surface gives rise to a film force, $F_F$ [53,90,111]. This film force is hypothesized to have a crucial role in defining the collision and thinning processes. This force is dependent on six key variables: surface tension, $\sigma$, viscosity, $\mu$, and density, $\rho$, of the liquid, bubble diameter, $D$, impact velocity, $V_{imp}$, and gravity, $g$. Thus, the dimensional form of the functional relationship is given as:

$$F_F = f\left(\sigma, \mu, \rho, D, V_{imp}, g\right) \tag{39}$$

To nondimensionalize this functional relationship, Buckingham pi theorem is applied [112]. Since there are seven variables containing three primary dimensions (mass, length, and time), four dimensionless pi groups are required to fully define the problem. However, since the terminal velocity of the bubble may be written as a function of bubble size and the liquid properties, only three dimensionless numbers would be required for bubbles impacting the surface at terminal velocity. Buoyancy is an omnipresent force during the bouncing process, and for this reason, the recurring variables are chosen to be those related to buoyancy: $\rho$, $g$, and $D$. The four pi groups are thus defined through:

$$\begin{gathered}
\Pi_1 = \sigma^a \rho^b g^c D^d = (MT^{-2})^a (ML^{-3})^b (LT^{-2})^c (L)^d \\
\Pi_2 = \mu^e \rho^f g^g D^h = (ML^{-1}T^{-1})^e (ML^{-3})^f (LT^{-2})^g (L)^h \\
\Pi_3 = V_{imp}^i \rho^j g^k D^l = (LT^{-1})^i (ML^{-3})^j (LT^{-2})^k (L)^l \\
\Pi_4 = F_F^m \rho^n g^o D^p = (MLT^{-2})^m (ML^{-3})^n (LT^{-2})^o (L)^p
\end{gathered} \tag{40}$$

Knowing the exponents must sum to zero, the values for *a*-*p* are found. The four dimensionless groups are then determined to be:

- $Bo = \frac{\rho g D^2}{\sigma}$; Bond number: ratio of buoyancy to surface tension forces.
- $Ar = \frac{\rho\sqrt{gD^3}}{\mu}$; Archimedes number: ratio of buoyancy to viscous forces.
- $Fr = \frac{V}{\sqrt{gD}}$; Froude number: ratio of inertial to gravitational forces.
- $\frac{F_F}{F_B} = \frac{F_F}{\frac{1}{6}\pi\rho g D^3}$; ratio of film to buoyancy forces.

For bubbles approaching at terminal velocity, the Froude number would not be required to define the collision as the impact velocity becomes a function of the other variables. With these groups, the dimensionless form of the functional relationship may be written as:

$$\frac{F_F}{F_B} = f(Bo, Ar, Fr) \tag{41}$$

### *4.3.3 Numerical Modeling*

As of yet, there exists no means to experimentally measure the film force. Therefore, we rely on two previously established and experimentally validated numerical models from Manica et al. [90,111], which describe bubble collisions with a solid surface and a free surface. A brief description of the numerical models will be given here for the sake of completeness, but it should be noted that the focus of the present work is not to derive or validate these models as this has already been done previously. This work simply uses the numerical models to generate data that can be used to identify the relationship between the relevant dimensionless numbers. In both, a point force model is used to determine the bubble equation of motion based on the balance of four forces: buoyancy ($F_B$), drag ($F_D$), added mass ($F_A$), and a film force ($F_F$). Each of these has been previously described in Section 1.1. The bubble is assumed to be approximately massless to give:

$$F_B + F_D + F_A + F_F = ma \approx 0 \tag{42}$$

$$-\frac{4}{3}\pi R^3 \rho g + C_D Re \frac{\pi}{4} \mu R V + \frac{4}{3}\pi R^3 \rho C_m \frac{dV}{dt} - \frac{2}{3} R^3 \rho \frac{dC_m}{dH} V^2 + \int_0^\infty 2\pi r p dr \ = 0 \tag{43}$$

For free surface collisions, the added mass coefficient, $C_m$, is assumed to be constant at 0.5, so the fourth term on the left-hand side of Equation 43 drops out. For solid surface collisions, this coefficient is given as a function of the distance between the bubble and surface at the axis of symmetry, $H$, and the bubble radius, $R$, using $\psi=(H+R)/R$:

$$C_m = 0.5 + 0.19222\psi^{-3.019} + 0.06214\psi^{-8.331} + 0.0348\psi^{-24.65} + 0.0139\psi^{-120.7} \tag{44}$$

The only change made to the models is in calculation of the drag coefficient, $C_D$. Originally, the theory of Moore [113] was used to calculate the drag coefficient. However, this theory is only valid for bubbles with Reynolds numbers greater than 100 and Weber numbers less than 3. The compiled theory presented by Loth [84] is instead used here which is valid for Reynolds numbers from 1 to 10,000 and any value of Weber number. In this theory, the drag coefficient is expressed using a normalized drag coefficient, $\Delta C_D^*$. For clean bubbles, this function is given as:

$$\Delta C_D^* = \frac{C_D - C_{D,We\to 0}}{C_{D,We\to\infty} - C_{D,We\to 0}} \tag{45}$$

$$C_{D,\,We\rightarrow 0} = \frac{16}{Re}\left\{1 + \left[\frac{8}{Re} + \frac{1}{2}\left(1 + \frac{3.315}{\sqrt{Re}}\right)\right]^{-1}\right\} \tag{46}$$

$$C_{D,\,We\rightarrow \infty} = \frac{8}{3} + \frac{16}{Re} \tag{47}$$

For Reynolds numbers less than 100, the normalized drag coefficient is given as:

$$\Delta C_D^* = \tanh(0.021We^{1.6}) \tag{48}$$

For Reynolds numbers greater than 100, the drag calculation is further divided depending on the Weber number. For Weber numbers greater than 5, where separated drag is appropriate, the following is used:

$$\Delta C_D^* = 2.5\tanh(0.2We) - 1.5 \tag{49}$$

At Weber numbers less than 3, the normalized drag coefficient is not used, and instead the theory presented by Moore [113] based on bubble aspect ratio, $\chi$, is used:

$$C_D = \frac{48}{Re}\mathrm{G}(\chi)\left(1 + \frac{K(\chi)}{Re}\right) \tag{50}$$

$$\mathrm{G}(\chi) = \frac{1}{3}\chi^{\frac{4}{3}}(\chi^2 - 1)^{\frac{3}{2}}\frac{\left[\sqrt{\chi^2 - 1} - (2 - \chi^2)\sec^{-1}(\chi)\right]}{\left[\chi^2\sec^{-1}(\chi) - \sqrt{\chi^2 - 1}\right]^2} \tag{51}$$

$$\mathrm{K}(\chi) = 0.0195\chi^4 - 0.2134\chi^3 + 1.7026\chi^2 - 2.1461\chi - 1.5732 \tag{52}$$

The aspect ratio was determined based on an empirically fit correlation presented by Loth [84], based on the Reynolds and Weber numbers as:

$$\frac{1}{\chi} = 1 - (1 - E_{min})\tanh(c_E We) \tag{53}$$

$$E_{min} = 0.25 + 0.55\exp(-0.09Re) \tag{54}$$

$$c_E = 0.165 + 0.55\exp(-0.3Re) \tag{55}$$

For Weber numbers between 3 and 5, the drag coefficient is simply taken as the maximum value between the drag coefficient predicted by Moore's theory and that predicted for separated drag. Figure 47 shows the predicted drag coefficient for bubbles of varying Reynolds and Weber numbers in water.

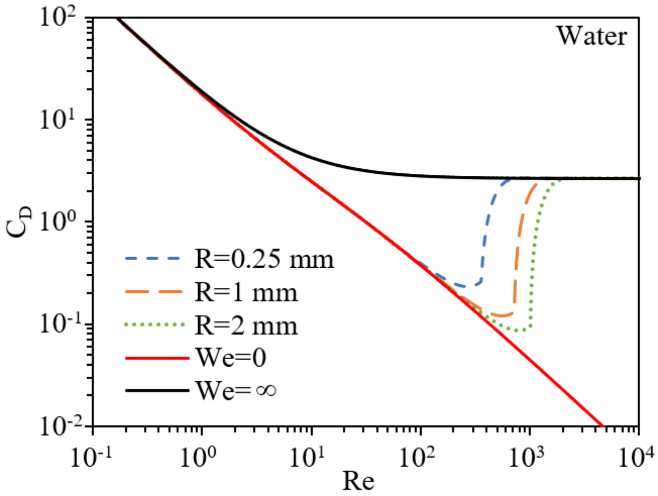

**Figure 47.** *Predicted drag coefficient values for various Reynolds and Weber number bubbles in water.*

In both models, the drainage rate of the film thickness, *h*, between the bubble and the surface is determined using the Stokes-Reynolds equation, assuming the bubble surface to be mobile and the solid or free surface to be immobile:

$$\frac{\partial h}{\partial t} = \frac{1}{3\mu r}\frac{\partial}{\partial r}\left(rh^3\frac{\partial p}{\partial r}\right) \tag{56}$$

The pressure buildup in the film, *p*, is characterized using two different versions of the augmented Young-Laplace equation. These are given by Equations 57 and 58 for a solid and free surface respectively:

$$p = \frac{2\sigma}{R} - \frac{\sigma}{r}\frac{\partial}{\partial r}\left(r\frac{\partial h}{\partial r}\right) \tag{57}$$

$$p = \frac{\sigma}{R} - \frac{\sigma}{2r}\frac{\partial}{\partial r}\left(r\frac{\partial h}{\partial r}\right) + \frac{\rho g z_S}{2} \tag{58}$$

For free surface collisions, the surface deformation, $z_S$, also needs to be determined. The augmented Young-Laplace equation is again used to describe the normal force balance at the free surface as:

$$\frac{\sigma}{r}\frac{\partial}{\partial r}\left(r\frac{\partial z_S}{\partial r}\right) = \rho g z_S - p \tag{59}$$

The dependent variables that are solved for by this model are $V(t)$, $h(r,t)$, $p(r,t)$, and for the free surface model, $z_S(r,t)$. Initial conditions are required for all of these, and boundary conditions are also required for $h$, $p$, and in the case of free surface collisions, $z_S$. The initial velocity is assumed to be zero or the bubble's terminal velocity. The initial film thickness is given as:

$$h(r,0) = h_{00} + \frac{r^2}{2R} \tag{60}$$

where $h_{00}$ is the initial distance between the top of the bubble and the surface. The pressure in the film is assumed to initially be zero, and the initial surface shape is taken as the undeformed free surface shape defined by $z_S=0$ for the free surface collision model. At the center, axisymmetric conditions are assumed so the inner boundary conditions are such that the first spatial derivatives of $h$, $p$, and $z_S$ are equal to zero at $r=0$. At the outer boundary, $r_m$, the film pressure is assumed to decay as $1/r^4$ to write $r\partial p/\partial r+4p=0$ for the solid surface collision model. For the free surface collision model, the pressure is simply assumed to be zero at this location. For a solid surface, the drainage rate at the outer boundary is taken as the opposite of the bubble velocity:

$$\frac{dh}{dt}(r_m,t) = -V(t) \tag{61}$$

For a free surface, the surface deformation is taken into account:

$$\frac{dh}{dt}(r_m,t) = -V(t) + \frac{dz_S}{dt}(r_m,t) \tag{62}$$

The free surface deformation at the outer boundary is based on the analytical surface shape defined by Manica et al. [90]:

$$z_S(r_m, t) = \frac{F_F}{2\pi\sigma} K_0\left(r_m\sqrt{\frac{\rho g}{\sigma}}\right) \tag{63}$$

where $K_0$ is the modified Bessel function of the second kind of order zero. For solid surface collisions, the outer boundary location was varied between $r_m=0.9R\text{-}1.2R$ in the original model. For the present work, it is kept constant at $r_m=1.1R$. For free surface collisions, the outer boundary location is taken as $r_m=1.2R$, as done in the original model.

The equation of motion of the bubble, Equation 43, is coupled with Equations 56 and 57 to solve the solid surface collision model, and with Equations 56, 58, and 59 to solve the free surface collision model. These equations are solved for $V(t)$, $h(r,t)$, $p(r,t)$, and $z_S(r,t)$ when necessary by first discretizing the spatial domain and using a second order finite difference approximation for the spatial derivatives. This reduces the problem to a system of ordinary differential equations, which is then solved using ode15s in Matlab with the initial and boundary conditions as specified. An event function was also employed with the model to stop the simulation if the film thickness reduced to zero. This was not in an attempt to predict rupture, it was solely employed to stop the simulation from predicting negative film thickness values. No claims are made on the relationship between rupture and this termination. The Matlab code written for this modeling is presented in Section 7.3 of the appendix. These models have been shown to be highly accurate in predicting the bubble velocity and trajectory with solid and free surface collisions [53,90,111] as well as the film thickness evolution for bubbles impacting a solid surface [9,53].

### *4.3.4 Prediction of Film Force Ratio and Film Radius*

To elucidate the influence of each dimensionless group, the numerical models described in Section 4.3.3 have been implemented to simulate bubble collisions over a range of Bond, Archimedes, and Froude numbers for both solid and free surface collisions.

During each bubble collision, the film force value spikes due to the sudden increase in film pressure, as demonstrated in the force evolution plot shown in Figure 48 for a 0.74 mm bubble colliding with a free surface in water. The maximum value of the film force during the collision is used in calculating the $F_F/F_B$ ratio.

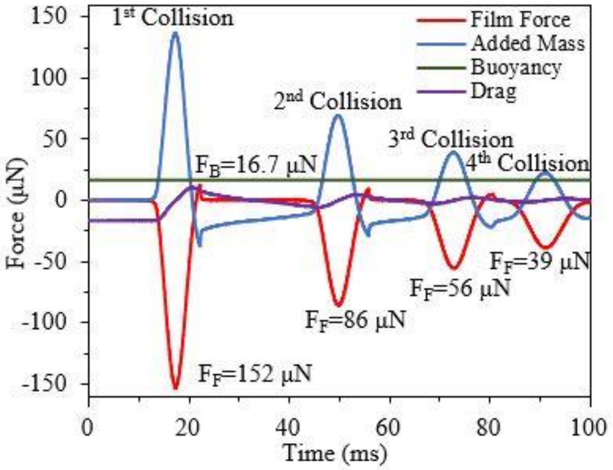

**Figure 48.** *Force evolution of a 0.74 mm bubble collision with a water/air interface.*

Considering bubbles impacting at terminal velocity, the cumulative results of the numerical modeling are shown in Figure 49(a) and (c). Since the Froude number is not required to define these collisions, a single plot is used to show the influence of the Bond and Archimedes numbers. The red points marked failure indicate where the film thickness at impact reached zero and the simulation was stopped. From these plots, an inverse relationship is seen to exist between the film force ratio and the Bond number. This effect can be better understood by considering variations in liquid surface tension. An increased surface tension, i.e. decrease in Bond number, implies the liquid/gas interfaces of the system will act in a stiffer manner. With a stiffer interface, less deformation and a larger pressure buildup occurs in the film, which results in an increased film force. The film force ratio is seen to be directly proportional to the Archimedes number. When the Archimedes number is relatively large, the buoyancy force is significantly greater than the viscous force slowing the bubble which leads to a larger terminal and impact velocity. The increased impact velocity induces a larger pressure buildup, and therefore, a larger film force. Between the solid and free surface collisions, a decrease in the film force ratio can be seen with the free surface compared to the solid surface. This is likely due to the fact that the free surface will rise and deform during the impact, while the solid surface remains immobilized. As such, the free surface acts as a sort of cushion for the colliding bubble which reduces the pressure buildup.

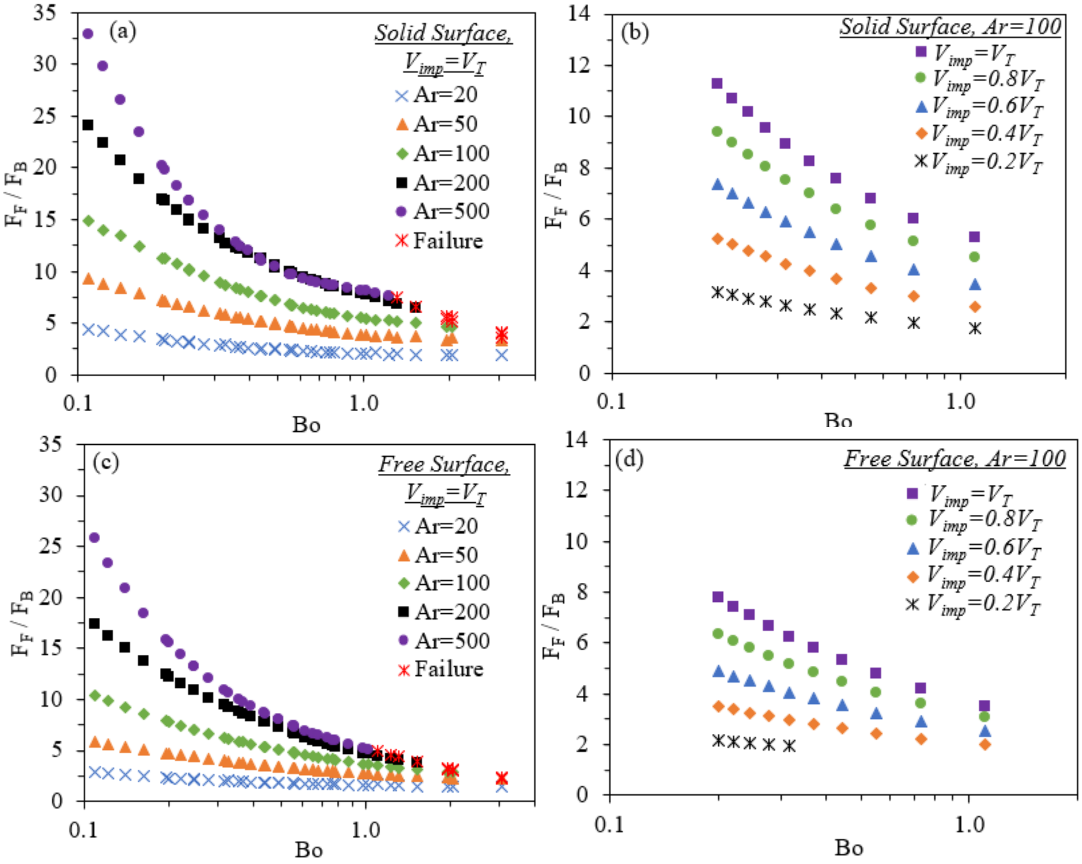

**Figure 49.** *Dimensionless plot of film force ratio for bubbles with varying Bo and Ar impacting (a) a solid surface at terminal and (b) nonterminal velocities, and (c) a free surface at terminal and (d) nonterminal velocities.*

To demonstrate the influence of the Froude number, bubbles with a constant Archimedes number of 100 approaching at nonterminal velocities are considered. These nonterminal cases could be bubbles released close to the interface, or subsequent impacts after the first collision. Since the Froude number is directly proportional to the impact velocity, the nonterminal bubbles impacting at $0.2V_T$-$0.8V_T$ would correspond to the Froude number being 0.2-0.8 times the Froude number calculated using the terminal velocity. As expected, the film force to buoyancy force ratio is seen to decrease with decreasing Froude number. The reduced impact velocity corresponds to a lower pressure buildup in the film, and thus, a reduced film force.

The final step in the theoretical analysis is to relate the film force to the film radius, $R_F$, to enable its prediction. To this end, the so-called Princen equations described in Section 2.1 are applied [11,60]. For a solid surface and a free surface, these are given by Equations 64 and 65 respectively:

$$\text{Solid Surface:} \qquad R_F^2 = \frac{F_F R}{2\pi\sigma} \tag{64}$$

$$\text{Free Surface:} \qquad R_F^2 = \frac{F_F R}{\pi\sigma} \tag{65}$$

These equations have been commonly used in describing dynamic bubble collisions previously [62,110,114]. The results shown in Figure 49 were translated to a dimensionless $R_F$ value normalized by bubble radius using these equations to show the influence of each dimensionless number, as presented in Figure 50. From this, it is seen that a larger Bond number induces a larger film radius. Again, this may further be explained by considering variations in the liquid surface tension. A lower liquid surface tension, i.e. a larger Bond number, indicates the liquid/gas interfaces are less stiff and more prone to deformation. As a result of this increased deformation, it is to be expected that the dimple formed at impact will take on a wider shape. Increases in Archimedes or Froude numbers are both indicative of increased impact velocity. Zawala and Malysa [62] explored the influence of impact velocity on radial film size and the results found here confirm their conclusions. A higher impact velocity leads to increased bubble shape and interface deformation, and thus, a larger film radius is produced.

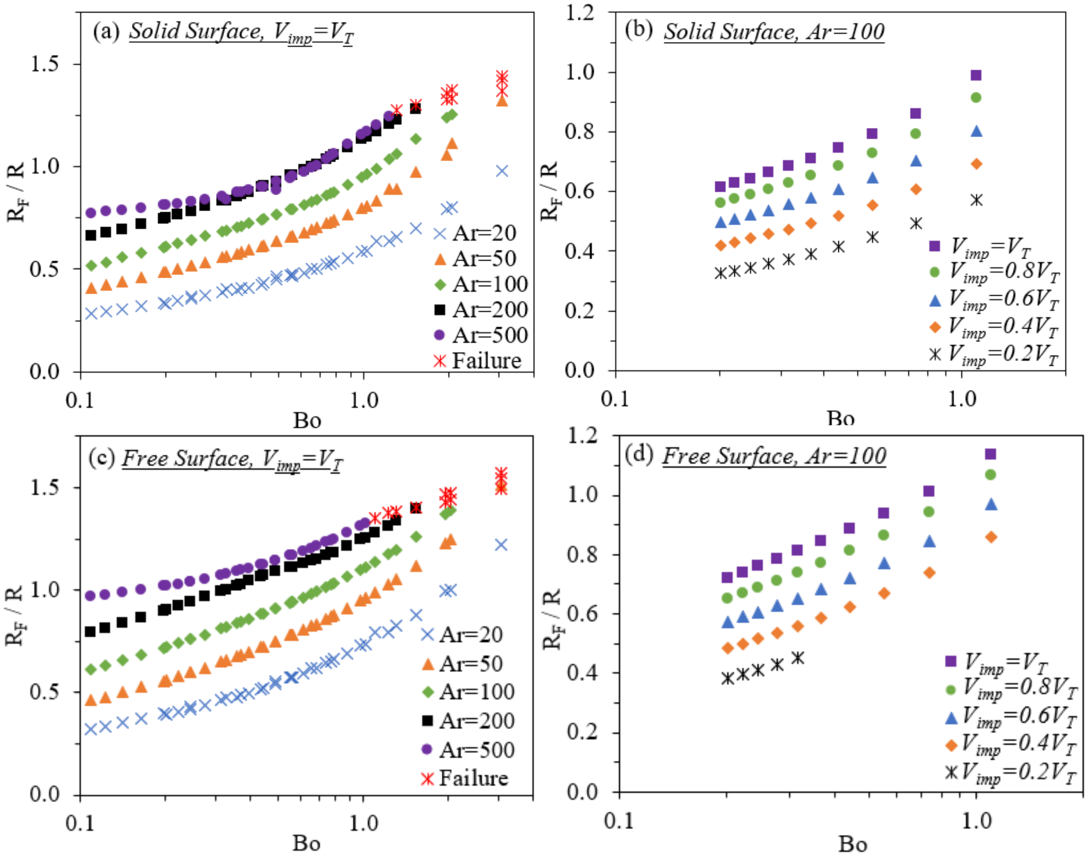

**Figure 50.** *Dimensionless film radius for bubbles with varying Bo and Ar impacting (a) a solid surface at terminal and (b) nonterminal velocities, and (c) a free surface at terminal and (d) nonterminal velocities.*

To validate this film radius prediction technique, the experimental film radius values found for solid surface collisions are compared to those found using the method outlined here in Figure 51. As shown, the majority of the predictions are within 20% error of the experimental values. In general, it can be seen that the first bounce tends to be slightly larger than predicted. A likely reason for this is the deformation of the bubble prior to impact, which is not taken into account by the model when predicting the film shape, although it is accounted for in the drag coefficient calculations. Since bubbles impacting at higher velocities have an oblate spheroid shape, the film radius is slightly larger than that predicted by the model. When the bubble impacts at lower velocities, such as in the subsequent bounces, the model is seen to be more precise. Unfortunately, there is currently no technique available to measure the film radius during dynamic bubble collisions with a free surface. As such, we are left to rely on the accuracy of the model in bubble velocity profile predictions for validation.

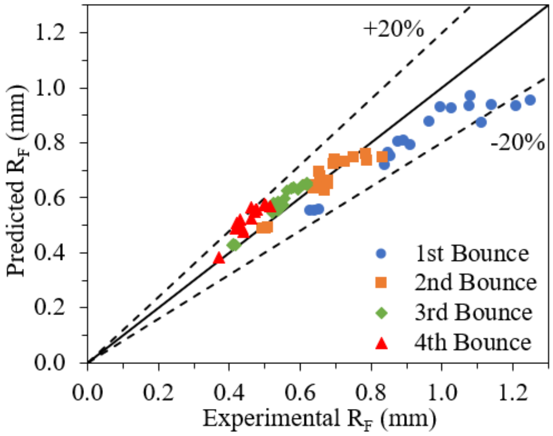

**Figure 51.** *Comparison between experimental and predicted film radius for bubbles colliding with a solid surface.*

While reasonably accurate, this method for predicting the film radius requires a significant amount of computation for prediction. Thus, a least squares regression analysis was performed to fit a function to the numerical data shown in Figure 50. This enables the prediction of the film radius based on easily attainable experimental values and liquid properties. For solid surface and free surface collisions, these functions are given by Equations 66 and 67, respectively:

$$\text{Solid Surface:} \qquad \frac{R_F}{R} = 0.62Bo^{0.42}Fr^{0.48}Ar^{0.039} \qquad (66)$$

$$\text{Free Surface:} \qquad \frac{R_F}{R} = 0.63Bo^{0.38}Fr^{0.44}Ar^{0.072} \qquad (67)$$

## 4.4 Modeling Bubble Collisions at Liquid-Liquid and Compound Interfaces

The collision of a bubble at a liquid-liquid or compound interface is a complex phenomenon with numerous underlying processes. While there have been several successful efforts made at modeling these processes using grid-based simulation techniques [18,46], these methods tend to be complex and highly demanding in terms of computational resources [53]. There are also added complexities related to grid size due to the variation in length scale order of magnitude. While the bubble is typically on the millimeter scale, the film formed between the bubble and the interface is typically on the micrometer scale. As such very fine or adaptive grid sizing is needed to capture both the bubble motion and film drainage phenomena in a single simulation. As an alternative to such grid-based simulations, previous modeling of bubble collisions at solid and free surfaces (outlined in Section 4.3.3) have made simplifications to the Navier-Stokes equations that are valid in different regimes based on Reynolds and Weber numbers [53,90,111]. This technique has proven to be highly accurate in predicting not just the bubble motion but also the spatiotemporal evolution of the liquid film formed at impact [9]. In this section, three extensions of this work are presented for the collision of a bubble at a liquid-liquid, solid-liquid-liquid, and gas-liquid-liquid interface. Experimental results from tests carried out with three different liquid combinations under various experimental conditions, using the setup described in Section 3.4, are also detailed and used to validate the model.

### *4.4.1 Liquid-Liquid Interface Collision Model*

The following derivation outlines a numerical model for a single bubble which collides and bounces at a liquid-liquid interface. As with the models outlined for bubble collisions at a solid surface and a free surface in Section 4.3.3, this model operates by employing a point force analysis to define an equation of motion for the bubble while the Stokes-Reynolds-Young-Laplace equations are used to define the pressure buildup and drainage rate of the film formed between the bubble and the interface as well as the liquid-liquid interface deformation. A schematic of the model is presented in Figure 52. In the subsequent analysis, the subscript *B* is used to relate the associated variable to the bottom liquid while the subscript *T* is used to relate it to the top liquid.

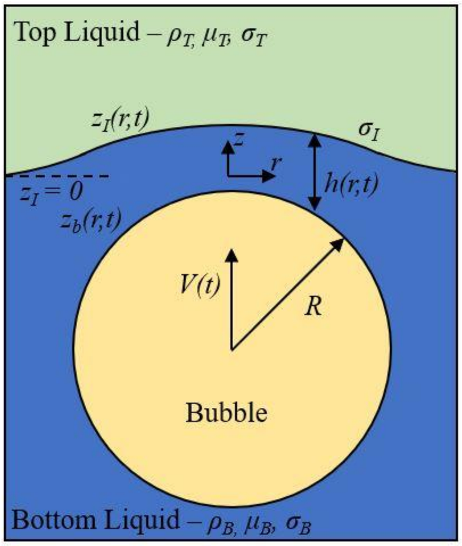

**Figure 52.** *Schematic of proposed model for bubble collisions at a liquid-liquid interface.*

The buoyancy, drag, added mass, and film forces described in Section 1.1, and used in the previous free and solid surface collision models described in Section 4.3.3 with Equation 43, are again used to define the bubble equation of motion as:

$$\frac{4}{3}\pi R^3 \rho_B C_m \frac{dV}{dt} = \frac{4}{3}\pi R^3 \rho_B g - C_D Re \frac{\pi}{4}\mu_B R V + \frac{2}{3} R^3 \rho_B \frac{dC_m}{dH} V^2 - \int_0^\infty 2\pi r p dr \quad (68)$$

where the first term on the left-hand side and third term on the right-hand side represent the added mass, the first and second term on the right-hand side are the buoyancy and drag forces respectively, and the last term of the equation is the film force. The drag coefficient, $C_D$, is calculated using the theory compile by Loth [84] which was outlined in Section 4.3.3

with Equations 45 through 55. As can be seen from Equation 68, it is assumed that the bottom liquid properties can be used to define the buoyancy, drag, and added mass forces. While this is valid when the bubble is far from the interface, the top liquid properties will influence these forces when the bubble is close to the interface. For example, as previously noted in Section 1.1, the added mass force is a result of liquid motion around the bubble. When the bubble is near the interface, it is not only the bottom liquid which will accelerate but also the top liquid. Similar arguments can be made for the buoyancy and drag forces, but the reality is that the complex fluid dynamics associated with liquid-liquid interface collisions are difficult to capture in a simple point force model such as this. Nonetheless, the assumption of using the bottom liquid properties for these forces is employed for the sake of simplicity. However, in an attempt to capture the influence of the upper liquid to some extent, the added mass coefficient has been adjusted to fit the experimental data. Since the upper liquid is, of course, less dense than the lower liquid, it is expected that a reduced value for the added mass coefficient will aid in providing an accurate model. As such, a constant reduced value is used for $C_m$ in the liquid-liquid collision model. Since a constant value is used, the third term on the right-hand side of Equation 68 will reduce to zero. This term will, however, be need in the solid-liquid-liquid model, as described in Section 4.4.2. Additional details on the specific value used will be discussed with the experimental results in Section 4.4.4.

The pressure in the film formed between the bubble and the interface, $p$, is determined based off a balance of normal force acting on the liquid-liquid interface and the bubble surface using the augmented Young-Laplace equation. Assuming an axisymmetric model and that the slope of the deformation is small, $|\partial z_I/\partial r| \ll 1$, the following equation is used to describe the liquid-liquid interface shape, $z_I(r,t)$:

$$\frac{\sigma_I}{r}\frac{\partial}{\partial r}\left(r\frac{\partial z_I}{\partial r}\right) = \Delta\rho g z_I - p + \tau_{v,T} \tag{69}$$

where the left-hand side is the interfacial tension, $\sigma_I$, times the mean curvature of the interface, the first term on the right-hand side represents the hydrostatic pressure, $p$ is the pressure due to fluid motion in the film, and $\tau_{v,T}$ is the normal viscous stress due to the presence of the top liquid. This normal stress is estimated using the following:

$$\tau_{v,T} = -2\mu_T\frac{\partial u_{z,T}}{\partial z} \approx 4\mu_T\left|\frac{\partial^2 z_I}{\partial r^2}\right|\frac{\partial z_I}{\partial t} \tag{70}$$

where $u_{z,T}$ is the liquid velocity in the z-direction at the interface. Since the velocity field around the interface is not made available through this method of modeling, the normal velocity gradient is estimated using the curvature of the interface, $2|\partial^2 z_I/\partial r^2|$, and the interfacial velocity, $\partial z_I/\partial t$. It is assumed that the pressure due to fluid motion above the interface is negligible. Additionally, the normal viscous stress below the interface is assumed negligible, as done in the previous free surface model [90]. Since the minimum film thickness is on the order of microns, it is not necessary to account for the disjoining pressure, which is only relevant when the film reduces to ~100 nm or less [7]. Similarly, the bubble surface shape, $z_b(r,t)$, is given as previously described [90]:

$$\frac{\sigma_B}{r}\frac{\partial}{\partial r}\left(r\frac{\partial z_b}{\partial r}\right) = -\frac{2\sigma_B}{R} + p \tag{71}$$

with the assumption $|\partial z_b/\partial r| \ll 1$. The term $2\sigma_B/R$ represents the Laplace pressure of the bubble.

The thickness of the film between the bubble and the interface is given by:

$$h = z_I - z_b \tag{72}$$

Equations 69 and 71 are then combined using Equation 72 to write the film pressure using $1/\bar{\sigma} = (1/\sigma_I + 1/\sigma_B)$:

$$p = \frac{2\bar{\sigma}}{R} + \frac{\bar{\sigma}}{\sigma_I}\tau_{v,T} + \frac{\bar{\sigma}}{\sigma_I}\Delta\rho g z_I - \frac{\bar{\sigma}}{r}\frac{\partial}{\partial r}\left(r\frac{\partial h}{\partial r}\right) \tag{73}$$

The drainage rate of the film thickness, $h$, is determined using lubrication theory assuming immobile boundary conditions at the liquid-liquid interface and mobile conditions on the bubble surface. Although the true boundary condition at the liquid-liquid interface is the continuity of shear stress and velocity, the assumption that it is immobile is made to simplify the analysis. The same assumption is made in the previous free surface collision model with successful results [90]. In lubrication theory, the Navier-Stokes equation is simplified assuming the film thickness is much less than its radial size. This was first done by Reynolds [4] in his derivation of the classical lubrication theory and is given as:

$$\frac{\partial h}{\partial t} = \frac{1}{3\mu_B r}\frac{\partial}{\partial r}\left(rh^3\frac{\partial p}{\partial r}\right) \tag{74}$$

Equations 68, 69, 73, and 74 must be solved simultaneously in order to determine $V(t)$, $z_I(r,t)$, $p(r,t)$, and $h(r,t)$, respectively. Initial conditions are needed for all four variables, and inner and outer boundary conditions are required for $z_I$, $p$, and $h$. Assuming $h_{00}$ is the initial distance between the top of the bubble and the liquid-liquid interface, the initial conditions for the thickness, pressure, interface shape, and velocity are given as:

$$h(r,0) = h_{00} + \frac{r^2}{2R} \quad p(r,0) = 0 \quad z_I(r,0) = 0 \quad V(0) = 0 \; or \; V_T \tag{75}$$

The axisymmetric inner boundary conditions at $r=0$ are given as:

$$\frac{\partial h}{\partial r}(0,t) = \frac{\partial p}{\partial r}(0,t) = \frac{\partial z_I}{\partial r}(0,t) = 0 \tag{76}$$

At the inner boundary, the interface shape, pressure, and drainage equations (69, 73, and 74) are undefined since $r=0$ is part of the denominator in certain terms of each. L'Hopital's rule is used at this location to determine these values. The outer boundary is defined at a constant radial location, $r_m$. The present model maintains the same value of $r_m=1.2R$ used in the previous free surface collision model and the assumption that the pressure in the film reduces to zero at this location [90]. Equation 72 is used to determine the outer boundary condition for the film thickness with the assumption that the bubble surface velocity is equal to the bubble center of mass velocity at this location:

$$\frac{\partial h}{\partial t}(r_m,t)=\frac{\partial z_I}{\partial t}(r_m,t)-\frac{\partial z_b}{\partial t}(r_m,t)=-V(t)+\frac{\partial z_I}{\partial t}(r_m,t) \tag{77}$$

The outer boundary condition for the liquid-liquid interface is determined in a similar fashion to that used for the free surface collision model based on an analytical solution to Equation 69. Since the film pressure is assumed to be zero at this location, this equation can be rewritten as:

$$\frac{1}{r}\frac{\partial}{\partial r}\left(r\frac{\partial z_I}{\partial r}\right)-\frac{\Delta\rho g z_I}{\sigma_I}=\frac{\partial^2 z_I}{\partial r^2}+\frac{1}{r}\frac{\partial z_I}{\partial r}-\frac{z_I}{\lambda_I^2}=\frac{\tau_{v,T}}{\sigma_I} \tag{78}$$

where $\lambda_I=\sqrt{\sigma_I/\Delta\rho g}$. Equation 78 is truly a nonlinear second order partial differential equation, but in order to solve for an analytical solution, the normal viscous stress is treated as a constant. With this assumption, a solution can be written in terms of the modified Bessel function of the second kind of order zero [115]:

$$z_I=AK_0\left(\frac{r}{\lambda_I}\right)-\frac{\tau_{v,T}}{\Delta\rho g} \tag{79}$$

To determine the constant, $A$, the asymptotic form of the modified Bessel function of the second kind of order zero for small arguments is used to rewrite Equation 79 as:

$$z_I = AK_0\left(\frac{r}{\lambda_I}\right) - \frac{\tau_{v,T}}{\Delta\rho g} \approx -A\ln\left(\frac{r}{2\lambda_I}\right) - A\gamma_E - \frac{\tau_{v,T}}{\Delta\rho g} \tag{80}$$

where $\gamma_E=0.57721566$ is the Euler constant. This form is then matched to an analytical solution for the interface shape in the inner region where the pressure can no longer be neglected but the hydrostatic pressure term can. With this assumption, Equation 69 becomes:

$$\frac{\sigma_I}{r}\frac{\partial}{\partial r}\left(r\frac{\partial z_I}{\partial r}\right) = -\left(p - \tau_{v,T}\right) \tag{81}$$

Noting the axisymmetric boundary condition at $r=0$, the first integration yields:

$$r\frac{\partial z_I}{\partial r} = -\frac{1}{\sigma_I}\int_0^r r\left(p - \tau_{v,T}\right)dr \tag{82}$$

This is integrated again using integration by parts and yields in the limit as $r$ goes to infinity:

$$z_I = -\frac{F_I}{2\pi\sigma_I}\ln\left(\frac{r}{2\lambda_I}\right) + z_I(0) + \frac{1}{\sigma_I}\int_0^\infty r\ln\left(\frac{r}{2\lambda_I}\right)\left(p - \tau_{v,T}\right)dr \tag{83}$$

where $F_I$ is the total force acting on the interface which may be written as:

$$F_I = \int_0^\infty 2\pi r\left(p - \tau_{v,T}\right)dr \tag{84}$$

Matching the coefficients of Equations 80 and 84 gives $A=F_I/(2\pi\sigma_I)$. Thus, the interface deformation at the outer boundary is given as:

$$z_I(r_m, t) = \frac{F_I(t)}{2\pi\sigma_I}K_0\left(\frac{r_m}{\lambda_I}\right) - \frac{\tau_{v,T}(r_m, t)}{\Delta\rho g} \tag{85}$$

With this final boundary condition, the model is fully defined. In order to solve this set of equations for $V$, $h$, $p$, and $z_I$, the method of lines is used. In this, the equations are discretized in the spatial domain to form a system of ordinary differential equations. This system of equations is solved in Matlab using the stiff differential equation solver, ode15s. The Matlab code written for this model is outlined in Section 7.3 of the appendix.

### *4.4.2 Solid-Liquid-Liquid Interface Collision Model*

In this section, a numerical model for bubble collisions at a solid-liquid-liquid interface is outlined. A schematic of the proposed model is shown in Figure 53. In this model, two liquid films are present: (i) a lower film made up of the bottom liquid, $h_2$, and (ii) and upper film made up of the top liquid, $h_1$. Although the forces acting on the bubble remain the same, it is now required to consider the pressure buildup and drainage of both liquid films. Lubrication theory and the augmented Young-Laplace equations are again employed to accomplish this.

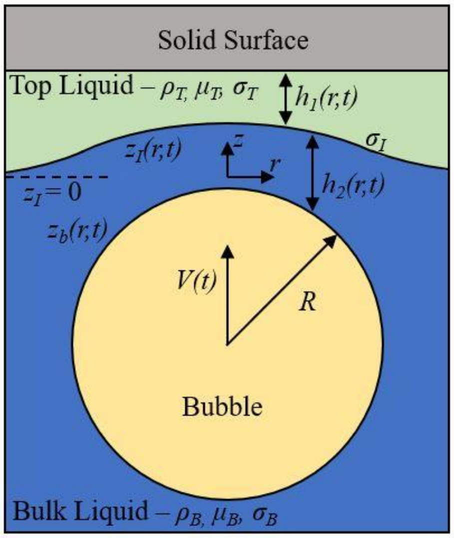

**Figure 53.** *Schematic of proposed model for bubble collisions at a solid-liquid-liquid interface.*

The same force balance model given by Equation 68 is used in this model as well. Only the pressure in the bottom film, $p_2$, is needed in calculation of the film force since the upper film is not in direct contact with the bubble. The only other change made to the force balance model is in calculation of the added mass coefficient, $C_m$. When a bubble collides with a solid surface, the added mass coefficient does not remain constant but instead increases as the bubble gets close to the surface [116] as described by Equation 44 in Section 4.3.3. This equation is again used in this model with the added change that $\psi=(H_1+H_2+R)/R$, where $H_1$ and $H_2$ are the film thicknesses of the upper and lower films at the axis of symmetry. Since the added mass coefficient is now a function of $H_1+H_2$, the derivative of the added mass coefficient with respect to center film thickness, $H$, in Equation 68 instead becomes $dC_m/d(H_1+H_2)$. Furthermore, the presence of the top liquid layer was taken into account in calculation of the added mass coefficient. If the film is very thin, the effect is expected to be negligible and Equation 44 can be used with just the adjustment to $\psi$. For thicker films, the effect will become more apparent so instead the reduced value for $C_m$ described for the liquid-liquid model is used in place of the nominal 0.5 value in Equation 44. The exact thickness at which this transition occurs has been determined based on the model fit to experimental data. As discussed later in Section 4.4.4, this transition is seen to occur when the initial top film thickness reached ~$0.5R$.

The augmented Young-Laplace equation for the liquid-liquid interface, $z_I$, and bubble surface, $z_b$, are modified to include the pressure in the both the lower, $p_2$, and upper, $p_1$, liquid films:

$$\frac{\sigma_I}{r}\frac{\partial}{\partial r}\left(r\frac{\partial z_I}{\partial r}\right)=\Delta\rho g z_I-p_2+p_1+\tau_{v,T} \tag{86}$$

$$\frac{\sigma_B}{r}\frac{\partial}{\partial r}\left(r\frac{\partial z_b}{\partial r}\right)=-\frac{2\sigma_B}{R}+p_2 \tag{87}$$

The top liquid layer is considered to be of uniform thickness, $h_{1,0}$, initially. The top film thickness is thus given by:

$$h_1=h_{1,0}-z_I \tag{88}$$

Since this model does not require solving for the liquid-liquid interface shape, the normal viscous stress previously given by Equation 70 is instead expressed in terms of the top film thickness using Equation 88:

$$\tau_{v,T} = -2\mu_T \frac{\partial u_{z,T}}{\partial z} \approx -4\mu_T \left|\frac{\partial^2 h_1}{\partial r^2}\right| \frac{\partial h_1}{\partial t} \tag{89}$$

Equation 87 is then substituted into Equation 88 to yield an expression for the pressure in the top liquid layer as:

$$p_1 = p_2 - \tau_{v,T} - \Delta\rho g\left(h_{1,0} - h_1\right) - \frac{\sigma_I}{r}\frac{\partial}{\partial r} r\left(\frac{\partial h_1}{\partial r}\right) \tag{90}$$

The thickness of the bottom liquid film, $h_2$, is given by:

$$h_2 = z_I - z_b \tag{91}$$

Using Equations 86 and 87, the film pressure is then written in terms of $1/\bar{\sigma} = (1/\sigma_I + 1/\sigma_B)$:

$$p_2 = \frac{\bar{\sigma}}{\sigma_I} p_1 + \frac{\bar{\sigma}}{\sigma_I}\tau_{v,T} + \frac{2\bar{\sigma}}{R} + \frac{\bar{\sigma}}{\sigma_I}\Delta\rho g\left(h_{1,0} - h_1\right) - \frac{\bar{\sigma}}{r}\frac{\partial}{\partial r}\left(r\frac{\partial h_2}{\partial r}\right) \tag{92}$$

Lubrication theory is again used to define the drainage rate of each of the films based on their respective pressures. No slip conditions are assumed at the solid surface and the liquid-liquid interface is again assumed to be immobile while the bubble surface is assumed to be fully mobile to yield:

$$\frac{\partial h_1}{\partial t} = \frac{1}{12\mu_T r}\frac{\partial}{\partial r}\left(r h_1^3 \frac{\partial p_1}{\partial r}\right) \tag{93}$$

$$\frac{\partial h_2}{\partial t} = \frac{1}{3\mu_B r}\frac{\partial}{\partial r}\left(r h_2^3 \frac{\partial p_2}{\partial r}\right) \tag{94}$$

In this model, Equations 68, 90, 92, 93, and 94 are solved for $V(t)$, $p_1(r,t)$, $p_2(r,t)$, $h_1(r,t)$, and $h_2(r,t)$. Initial conditions are needed for all five variables, and boundary conditions are needed for the film pressures and thicknesses. As previously noted, the initial top layer film thickness is assumed constant at $h_{1,0}$. The initial bottom film thickness is defined in the same manner that initial film thickness is defined in Equation 75 with the initial film thickness at the axis of symmetry being a set value, $h_{2,00}$. The initial pressure in both layers is assumed to be zero, and the initial velocity is either the associated bubble terminal velocity or zero, depending on the conditions being modeled. The inner boundary conditions are given based on the axisymmetric assumption:

$$\frac{\partial p_1}{\partial r}(0,t) = \frac{\partial p_2}{\partial r}(0,t) = \frac{\partial h_1}{\partial r}(0,t) = \frac{\partial h_2}{\partial r}(0,t) = 0 \tag{95}$$

L'Hopital's rule is again used to determine the pressure and drainage rate at the inner boundary since the associated equations are undefined due to $r=0$ being in the denominator. The outer boundary location is implemented as $r_m=1.2R$ for this model as well. At this location, the pressure in both the lower and upper films is assumed to drop to zero. To determine an analytical solution for interface deformation, the exact same analysis process outlined in Section 4.4.1 can also be applied to Equation 86. The only difference between this equation and the previously employed equation for normal interfacial stress balance (Equation 69) is the inclusion of the top liquid pressure. This solution is used along with Equation 88 to give the outer boundary condition for the top film thickness:

$$h_1(r_m,t) = h_{1,0} - \frac{F_I(t)}{2\pi\sigma_I} K_0\left(\frac{r_m}{\lambda_I}\right) + \frac{\tau_{v,T}(r_m,t)}{\Delta\rho g} \tag{96}$$

where $\lambda_I = \sqrt{\sigma_I/\Delta\rho g}$. The pressure in the upper film acting on the interface is accounted for by the interface force to give:

$$F_I = \int_0^\infty 2\pi r\left(p_2 - p_1 - \tau_{v,T}\right) dr \tag{97}$$

Lastly, Equations 88 and 91 are used to define the outer boundary condition, assuming the bubble surface velocity is the same as the bubble center of mass velocity at this position:

$$\frac{\partial h_2}{\partial t}(r_m, t) = \frac{\partial z_I}{\partial t}(r_m, t) - \frac{\partial z_b}{\partial t}(r_m, t) = -V(t) - \frac{\partial h_1}{\partial t}(r_m, t) \tag{98}$$

As with the liquid-liquid model, the partial differential equation for $h_1$, $h_2$, $p_1$, and $p_2$ are discretized in the spatial domain to reduce the problem to a system of ordinary differential equations which are solved with the ordinary differential equation for $V$ in Matlab using ode15s with the initial and boundary conditions described. The code written in Matlab is outlined in Section 7.3 of the appendix.

### 4.4.3 Gas-Liquid-Liquid Interface Collision Model

In one last extension, a model for a bubble collision with a gas-liquid-liquid interface is outlined, a schematic for which is shown in Figure 54. As with the solid-liquid-liquid interface collision model, two liquid films are accounted for in this model using lubrication theory. Unlike the solid-liquid-liquid model, however, the upper surface of the top liquid is a deformable free surface. The fluid above the top liquid is taken to be a gas with negligible density and viscosity.

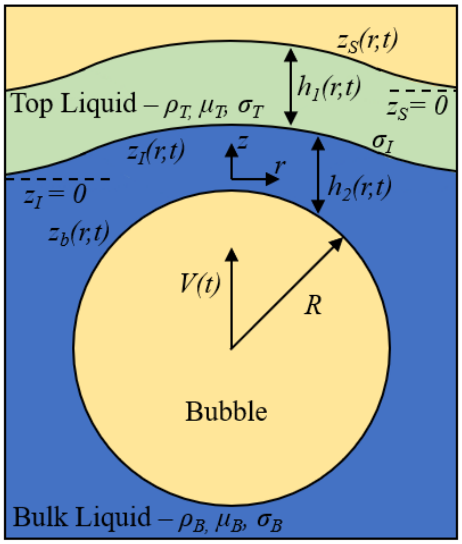

**Figure 54.** *Schematic of the proposed model for bubble collisions at a gas-liquid-liquid interface.*

The force balance model given by Equation 68 is again used here. The added mass coefficient in this scenario will depend upon the initial thickness of the top liquid layer. If the film is relatively thick, the fluid motion around the bubble during its impact with the interface will be very similar to that in a liquid-liquid interface collision. As such, the reduced added mass coefficient described for the liquid-liquid interface collision model can be used. However, if the film is relatively thin, the added mass coefficient would regress to that for a free surface collision, i.e. constant at 0.5 [90]. The exact thickness at which the transition from thin to thick occurs in relation to estimating the added mass coefficient is determined based off the model fit to experimental data. Experimentally, this transition is seen to occur when the initial top film thickness is at ~$0.5R$, as discussed later in Section 4.4.4.

Equations 86 and 87 are also valid for this model in describing the liquid-liquid and bubble surface shape. The augmented Young-Laplace equation is again used to define one additional equation needed to describe the free surface shape, $z_S$:

$$\frac{\sigma_T}{r}\frac{\partial}{\partial r}\left(r\frac{\partial z_S}{\partial r}\right) = \rho_T g z_S - p_1 \tag{99}$$

Considering the top liquid layer to initially be of uniform thickness, $h_{1,0}$, the top film thickness, $h_1(r,t)$, is then given by:

$$h_1 = h_{1,0} + z_S - z_I \tag{100}$$

Using Equations 86, 99, and 100, the pressure in the top liquid layer, $p_1$, is then written using $1/\sigma' = (1/\sigma_I + 1/\sigma_T)$:

$$p_1 = \frac{\sigma'}{\sigma_I}p_2 - \frac{\sigma'}{\sigma_I}\tau_{v,T} + \frac{\sigma'}{\sigma_T}\rho_T g z_S - \frac{\sigma'}{\sigma_I}\Delta\rho g\left(h_{1,0} + z_S - h_1\right) - \frac{\sigma'}{r}\frac{\partial}{\partial r}\left(r\frac{\partial h_1}{\partial r}\right) \tag{101}$$

Since Equation 86, 87, and 91 still hold true for this model, Equation 92 can be used again. The only change needed is in the hydrostatic pressure term in which the interface deformation is given by $h_{1,0}+z_S-h_1$ instead of $h_{1,0}-h_1$ in order to account for the free surface deformation. The normal viscous stress is also adjusted in this model to account for the thickness of the upper film. Particularly, when the top film is very thin, the interfacial velocity will not be representative of the normal velocity gradient as defined by Equation 70. In that scenario, both the upper and lower surface of the film will move with very similar velocities, and thus, the normal velocity gradient would be very small. To account for this effect, the upper film drainage rate is used instead of the interface velocity. The interface curvature is still used, however, as described using Equation 100:

$$\tau_{v,T} = -2\mu_T \frac{\partial u_{z,T}}{\partial z} \approx -4\mu_T \left|\frac{\partial^2 z_S}{\partial r^2} - \frac{\partial^2 h_1}{\partial r^2}\right| \frac{\partial h_1}{\partial t} \tag{102}$$

The drainage rate for the films is given using lubrication theory with the assumption that the free surface and bubble surface are fully mobile while the liquid-liquid interface is immobile. For the upper film the drainage is given by changing the 12 to a 3 in Equation 93 to account for the free surface mobility. Equation 94 is used as is for the lower film drainage rate.

In this model, Equations 68, 101, 92, 93, 94, and 99 are solved for $V(t)$, $p_1(r,t)$, $p_2(r,t)$, $h_1(r,t)$, $h_2(r,t)$, and $z_S(r,t)$ with the modifications mentioned in the previous two paragraphs. Initial conditions are needed for all six and boundary conditions are needed for the film pressures, film thicknesses, and free surface shape. The initial conditions are the same as that outlined for the solid-liquid-liquid collision model with the addition of the free surface initially being flat at $z_S=0$. The inner boundary conditions are also the same as that used for the solid-liquid-liquid collision model given by Equation 95 with the addition of the axisymmetric condition applied to the free surface shape. L'Hopital's rule is again needed to define the equation for film pressures, thicknesses, and interface shape at *r=0*. The outer boundary location is taken at $r_m=1.2R$ as done in the previous two models outlined here. The pressure in both liquid layers is assumed to be zero at this location. The method for finding an analytical solution for interface shape outlined in Section 4.4.1 is applied to Equations 99 and 86 to give the free surface and interface deformation as:

$$z_S = \frac{F_S}{2\pi\sigma_T} K_0\left(\frac{r}{\lambda_T}\right) \tag{103}$$

$$z_I = \frac{F_I}{2\pi\sigma_I} K_0\left(\frac{r}{\lambda_I}\right) - \frac{\tau_{v,T}}{\Delta\rho g} \tag{104}$$

where $\lambda_T = \sqrt{\sigma_T/\rho_T g}$ , $\lambda_I = \sqrt{\sigma_I/\Delta\rho g}$, and $F_S$ and $F_I$ are the total force acting on the free surface and liquid-liquid interface, respectively, given by:

$$F_S = \int_0^\infty 2\pi r p_1 dr \tag{105}$$

$$F_I = \int_0^\infty 2\pi r\left(p_2 - p_1 - \tau_{v,T}\right) dr \tag{106}$$

Equation 103 and 105 are used for the outer boundary condition for the free surface deformation. Using Equations 100, 103, and 104, the outer boundary condition for the top film thickness is written as:

$$h_1(r_m, t) = h_{1,0}(r_m, t) + \frac{F_S(t)}{2\pi\sigma_T} K_0\left(\frac{r_m}{\lambda_T}\right) - \frac{F_I(t)}{2\pi\sigma_I} K_0\left(\frac{r_m}{\lambda_I}\right) + \frac{\tau_{v,T}(r_m, t)}{\Delta\rho g} \tag{107}$$

Using Equation 91 and 100 and assuming the bubble surface velocity to be the same as the bubble center of mass velocity at the outer boundary, the drainage rate of the lower film at this location is given as:

$$\frac{\partial h_2}{\partial t}(r_m, t) = -V(t) + \frac{\partial z_S}{\partial t}(r_m, t) - \frac{\partial h_1}{\partial t}(r_m, t) \tag{108}$$

As with the previous models described here, the partial differential equations for $h_1$, $h_2$, $p_1$, $p_2$, and $z_S$ are discretized in the spatial domain using second-order finite differences to reduce the problem to a system of ordinary differential equations which are solved with the ordinary differential equation for $V$ in Matlab using ode15s with the initial and boundary conditions described. The code written to solve these equations is outlined in Section 7.3 of the appendix.

### *4.4.4 Experimental Validation*

Experiments were carried out using the setup described in Section 3.4 to capture the collision of a 0.65 mm radius bubble with various interfaces. Water was used as the bottom liquid and either 1, 5, or 10 cSt silicone oil (SO-1,5, or 10) was used as the top liquid. The properties of the individual liquids used in the modeling are shown in Table 2 while the properties of the specific combinations are shown in Table 3. Film thicknesses of 0.25, 0.50, and 1.00 mm were tested for each liquid combination in both the gas-liquid-liquid and solid-liquid-liquid configurations. A polypropylene surface was used as the solid surface due to its oleophilic and hydrophobic properties. The top liquid layer was increased to ~10 mm for comparison to the liquid-liquid interface collision model. Bubbles were released from ~120 mm, as well as closer distances, to validate the models for bubbles impacting at terminal and nonterminal velocities. The trajectory of the bubble was recorded using a high-speed camera and was used to determine the bubble velocity and validate the numerical models. The experimental data was offset temporally to match the initial bubble collision of the model. Experiments found in literature for bubble collisions at a liquid-liquid interface made up of PP11 and water [117] and bubble collisions at a gas-liquid-liquid interface made up of water and 20 cSt silicone oil [46] are also used for validation.

Figure 55 presents a comparison of the experimental velocity profiles to those found using the model outlined in Section 4.4.1 for liquid-liquid interface collisions. Bubbles released far from the interface which impact at terminal velocity are shown in Figure 55(a). In the associated models, the added mass coefficient was set to 0.40, 0.46, and 0.47 when the top liquids were 1, 5 and 10 cSt silicone oil respectively. Interestingly, it was noted that these values are all approximately half of the density ratio between the top and bottom liquids. All three of these liquid combinations have very similar interfacial tensions, ~50 mN/m, so differences in their velocity profiles result from variations in the silicone oil density and viscosity. The most significant bouncing is seen to occur with the 1 cSt silicone

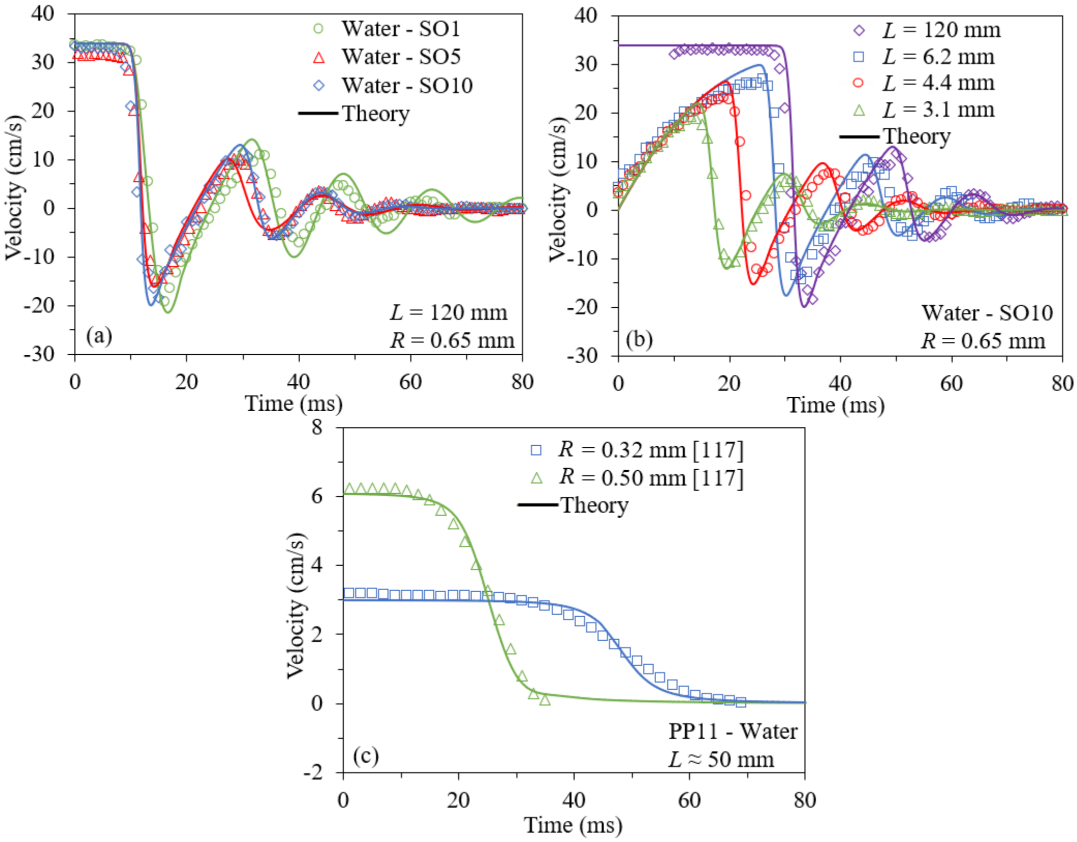

**Figure 55.** *Comparison of numerical model for bubble collisions at a liquid-liquid interface to experimental data for (a) bubbles impacting various water-silicone oil interfaces at terminal velocity, (b) bubbles impact a water-10 cSt silicone oil interface at nonterminal velocities, and (c) bubble of various sizes impacting a PP11-water interface from Vakarelski et al. [117].*

oil as the top liquid, while the experimental data for the 5 and 10 cSt silicone oil is nearly identical. This trend is followed very closely by the numerical model. In Figure 55(b), velocity profiles from bubbles released close to a water-10 cSt silicone oil interface are shown with $L$ being the distance between the capillary and the interface. The initial film thickness was taken as $h_{00}=L-2R$ for the numerical model. The same value of 0.47 was used for the added mass coefficient as was used previously for bubbles impacting at terminal velocity with this liquid combination. As expected, the initial parts of the velocity profiles where the bubble has not yet collided with the interface are identical. The bubble released closest to the interface collides first and achieves the smallest rebound velocity. This is consistent with previous results for bubble collisions at a free surface in which a reduced impact velocity results in smaller bounces [93]. Lastly, experimental results found in literature from Vakarelski et al. [117] for bubbles colliding with a PP11-water interface are presented in Figure 55(c). PP11 is a fluorocarbon liquid with a density, viscosity, and surface tension of 2030 kg/m$^3$, 19.2 mPa s, and 21.5 mN/m [117]. The interfacial tension was measured to be 47 mN/m in this system. An added mass coefficient of 0.25 was used in the numerical modeling, which again fits the usage of half the density ratios for this value. The large density difference between PP11 and water is the likely reason why such a dramatically reduced value is needed. As with the experiments conducted for this study, the model is able to match the experimental data with reasonable accuracy.

The numerical model is also able to predict features of the collision process that are not able to be captured experimentally, such as the film thickness and film pressure shown in Figure 56(a) and (b) respectively for the first collision of a 0.65 mm radius bubble at terminal velocity with a water-5 cSt silicone oil interface. In this, the bubble reaches its maximum height just after 12 ms and then rebounds away from the interface. From Figure 56(a), it can be seen that the film takes on the typical dimple shape during the collision. As the bubble departs from the interface, the film thickness at the axis of symmetry decreases. This is the result of the negative pressure buildup as liquid is sucked back into the film to replace the void left by the departing bubble.

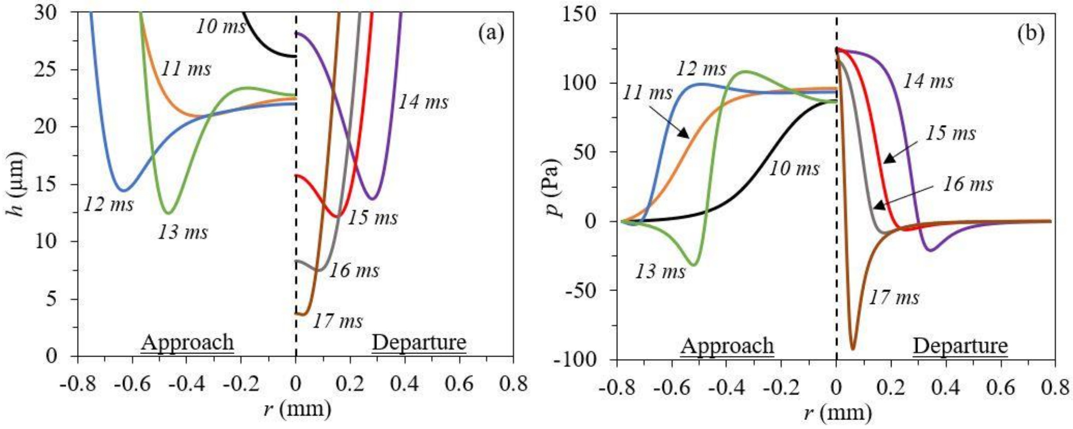

**Figure 56.** *Numerical predictions of (a) film thickness and (b) film pressure buildup during the first collision of a 0.65 mm radius bubble at terminal velocity colliding with a water-5 cSt silicone oil interface.*

A comparison of the velocity profiles predicted by the model and those captured in experiment for bubble collisions at a solid-liquid-liquid interface is shown in Figure 57. In these collisions, the influence of the upper liquid on the forces involved in the collision process will be dependent on the thickness of the upper liquid layer. If the layer is very thin, the influence of the upper liquid properties on predicting these forces may be minimal; however, as the upper layer becomes thicker, this influence will become more apparent. The exact transition thickness at which this occurs is determined based on experimental data. The experimental results suggest that the bubble velocity profile converges very quickly to that of a liquid-liquid interface collision with increasing top film thickness. When the upper film thickness is just 0.50 mm initially, the profiles begin to overlap for all three data sets. Thus, the influence of the upper liquid properties is only accounted for

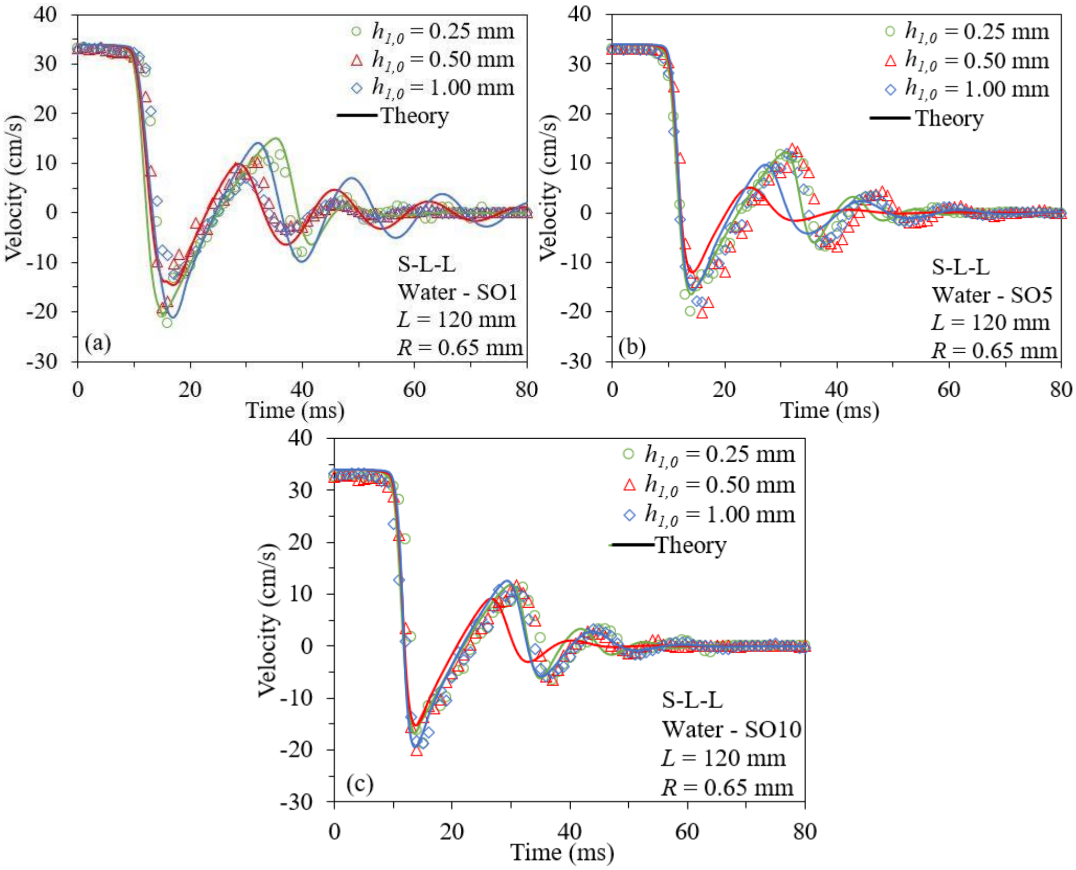

**Figure 57.** *Comparison of numerical model for bubble collisions at a solid-liquid-liquid interface to experimental data for bubbles colliding with various polypropylene-silicone oil-water interfaces at terminal velocity.*

when determining the added mass coefficient for the initial top film thicknesses of 0.50 and 1.00 mm by adjusting the nominal 0.5 value in Equation 44 to the reduced value used in the associated liquid-liquid interface collision model. For the film thickness of 0.25 mm, Equation 44 was used as presented to calculate the added mass coefficient. Interestingly, the most damped behavior predicted by the model occurs at the intermediate film thickness of 0.50 mm. This is most likely a results of idealizations made by the model. To examine this phenomenon further, the bubble surface and liquid-liquid interface location at the central axis, i.e. at $r=0$, were graphed over time, as shown in Figure 58, for the water-5 cSt silicone oil combination. In this figure, it can be seen that for initial film thicknesses of 0.25 mm and 1.00 mm, the bubble surface moves away from interface after the initial collision. However, when the film thickness is 0.50 mm thick, the two interfaces are seen to remain very close together throughout the collision process. This results in the prediction of overdamped motion at this film thickness. In actual experiments, bubble oscillations, which are not accounted for in the model, will occur during the rebound process and prevent this from occurring.

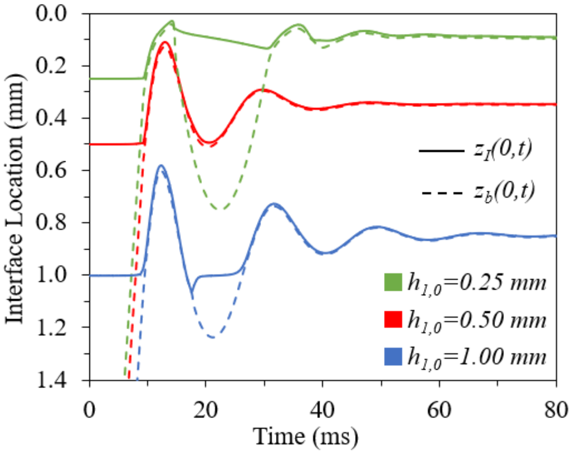

**Figure 58.** *Bubble surface and liquid-liquid interface location at the central axis for various initial film thicknesses.*

As with the liquid-liquid model, the film thickness and pressure are predicted in the solid-liquid-liquid model for both the upper and lower layers. Figure 59 shows these predictions during the first collision of a 0.65 mm radius bubble impacting at terminal velocity with a solid-5 cSt silicone oil-water interface. The initial top film thickness is 0.50 mm. The bottom film thickness and pressure profile evolution are very similar to that in the liquid-liquid interface collision presented in Figure 56. The top film never takes on the dimpled shape like the bottom film. Since the dimple formation is seen to begin when the film thickness reduces to ~20 μm, this is to be expected as the top film only reaches ~100 μm at its thinnest. Accordingly, the pressure buildup in the upper film is also much less than that observed in the lower film. It is likely, however, that the dimple and associated higher pressure would occur for thinner initial top film thicknesses.

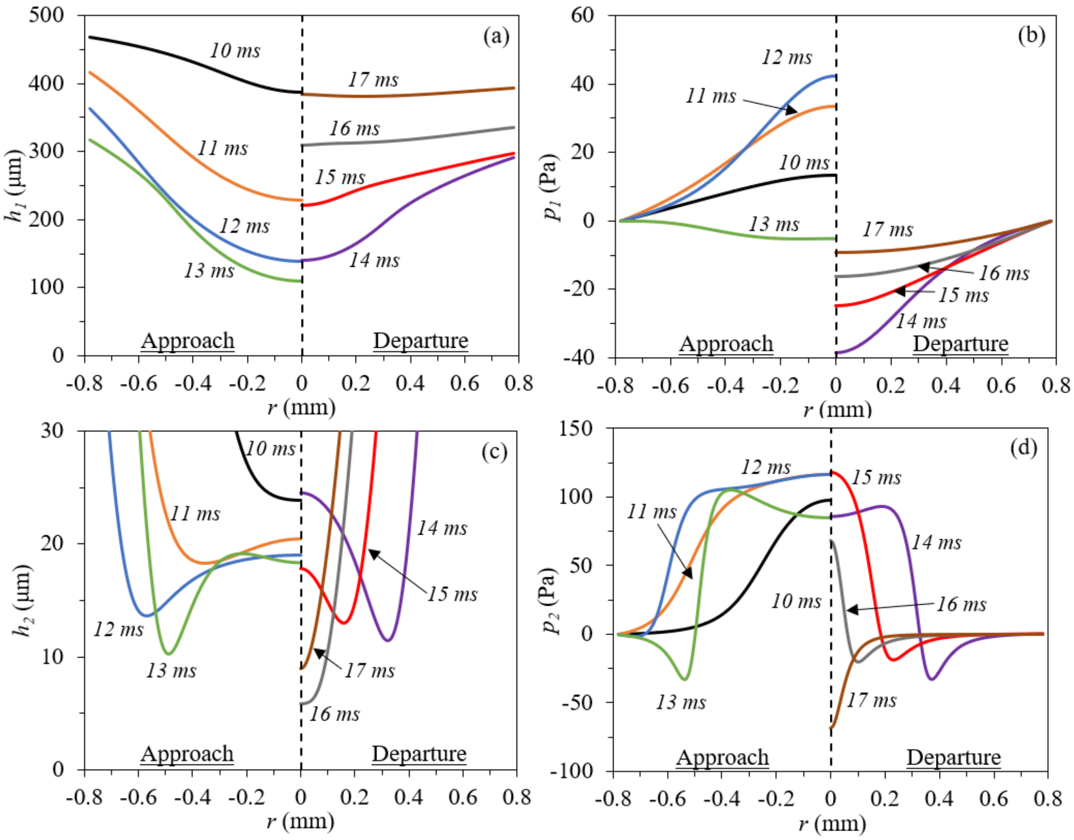

**Figure 59.** *Thickness and pressure distributions in the (a)-(b) upper, and (c)-(d) lower films during a bubble collision at a solid-5 cSt silicone oil-water interface.*

The experimental and theoretical results for bubble collisions at gas-liquid-liquid interfaces are shown in Figure 60. The experiments conducted here with water and 1, 5, and 10 cSt silicone oil are presented in Figures 60(a)-(c) while experimental results from Feng et al. [46] are shown in Figure 60(d) for bubble collisions at an air-20 cSt silicone oil-water interface. The same sized bubbles were used in those experiments as have been used here. Close agreement is seen between the numerical model predictions and all the experimental results. It should be noted that the liquid properties used in modeling data from Feng et al. [46] are those reported for their 20 cSt silicone oil. These properties are similar but not identical to those of the 20 cSt silicone oil used here for flow regime identification in Section 4.1. As was done in modeling the solid-liquid-liquid interface collisions, the added mass coefficient was left as 0.5 when modeling the thinnest initial film thickness of 0.25 mm, while for all other film thicknesses the added mass coefficient was set to the reduced value used in the liquid-liquid interface collision model. This suggests that the transition from a thin to a thick film discussed in Section 4.4.3 in relation to calculation of the added mass coefficient occurs somewhere between *0.38R-0.77R*. Similar to the solid-liquid-liquid interface collisions, the experimental and numerical results are both seen to converge to the liquid-liquid solution by the time the film reaches just one millimeter in thickness. In all the experiments conducted here, the 0.25 mm thick film resulted in the least damping effect on the velocity profile as expected. Unlike the solid-liquid-liquid model, there is no overshoot at the intermediate thickness of 0.50 mm. Instead, the profile simply transitions directly to that of a liquid-liquid interface collision.

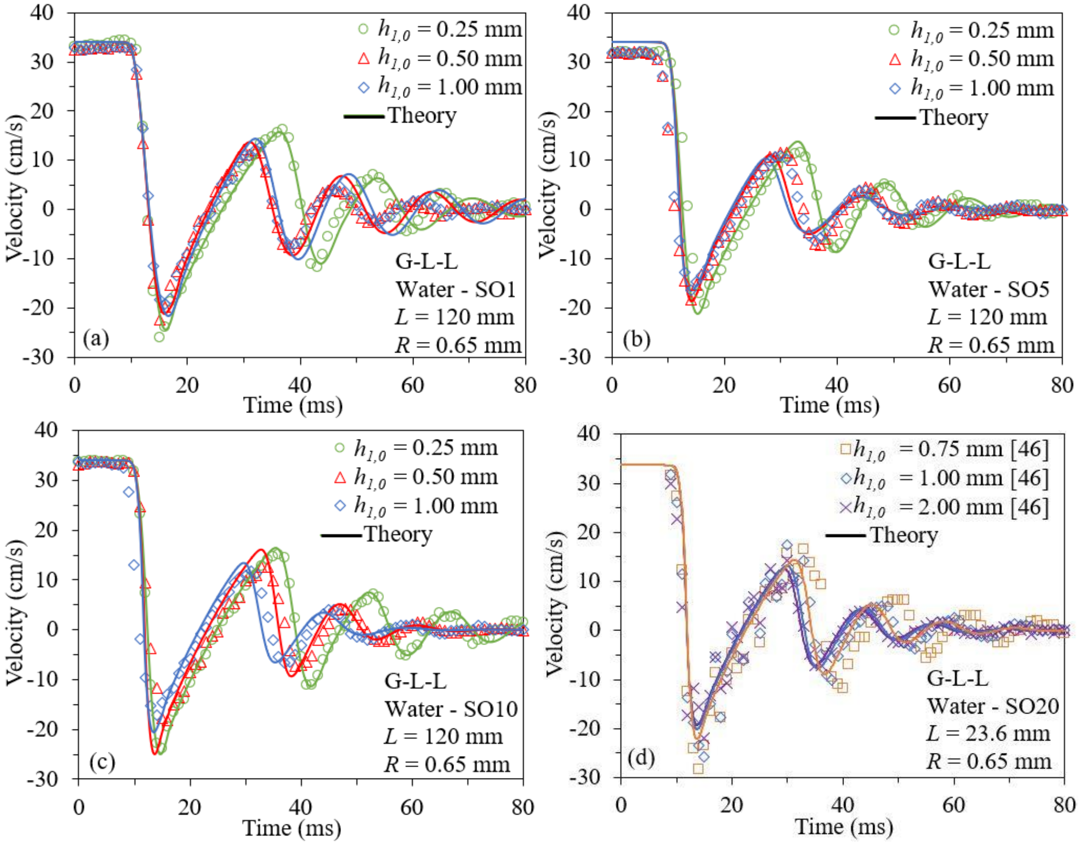

**Figure 60.** *Comparison of numerical model for bubble collisions at a gas-liquid-liquid interface to experimental data for bubbles colliding with various air-silicone oil-water interfaces at terminal velocity.*

Finally, the numerically predicted film thicknesses and pressure distributions during the first collision of a 0.65 mm radius bubble at terminal velocity with a gas-5 cSt silicone oil-water interface are shown in Figure 61. Although the thickness of the upper film is very similar to that predicted by the solid-liquid-liquid model, the pressure distribution is significantly reduced. This is the result of the upper surface's to ability deform under an applied pressure as opposed to the solid immovable surface. The bottom film thickness again acts very similar to the bottom film predicted by the liquid-liquid and solid-liquid-liquid interface collision models. A peak pressure around 100 Pa is achieved in all three, forming a similar plateau type configuration.

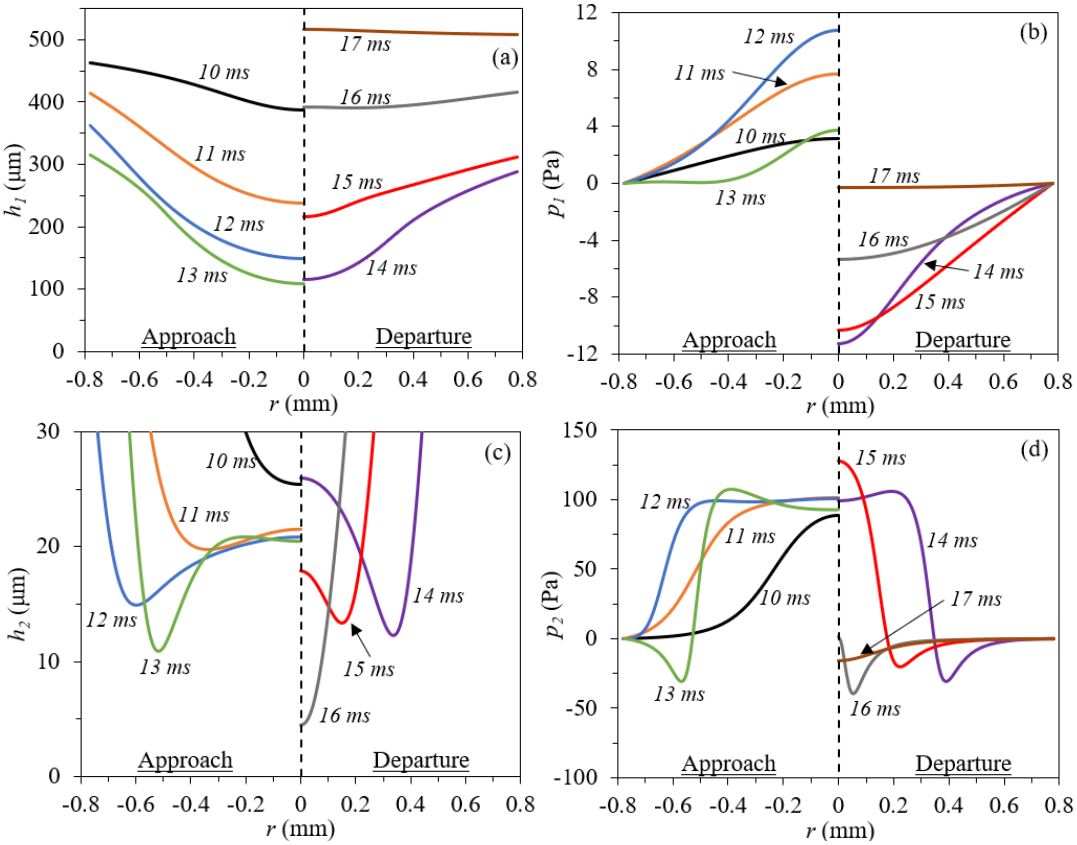

**Figure 61.** *Thickness and pressure distributions in the (a)-(b) upper, and (c)-(d) lower films during a bubble collision at a gas-5 cSt silicone oil-water interface.*

# 5 Summary and Future Recommendations

## 5.1 Key Contributions

Bubble interactions at multi-fluid interfaces occur in numerous industrial applications and environmental phenomena. Bubble passage through a liquid-liquid interface is present in processes related to metallurgy, nuclear reactor safety, direct contact evaporation, and solid shell formation. Furthermore, bubble collisions with liquid-liquid and compound interfaces are present in various environmental phenomena such as bubble collisions with the sea surface microlayer or the collision of liquid encapsulated bubbles. In any of these applications, the flow dynamics associated with the bubble collision play a crucial role in governing the overall process, be it in terms of mass or heat transfer efficiency, bubble shell production rate, chemical reaction rate, etc. Therefore, a fundamental understanding of the fluid dynamics involved in the collision and passage processes would significantly aid in designing such systems to improve process efficiency. To this extent, the present work was aimed to further this understanding through a combined experimental and theoretical approach. Extensive experimentation was carried out related to adiabatic bubble interactions at liquid-liquid and compound interfaces. Theoretical analysis supplemented this work to provide a comprehensive understanding of the associated process. An extension to the related phenomenon of immiscible bubble growth was also explored.

The key contributions from this work are summarized below:

i. Exhaustive experimental testing was carried out to identify and classify various flow regimes associated with single bubble and bubble stream passage through a liquid-liquid interface. Six different liquid combinations were tested to cover a broad range of interfacial tensions, viscosity ratios, and density differences of the associated liquids. Four different regimes were identified for single bubble passage, and six were found for bubble stream passage. The influence of the associated liquid combination properties on the flow dynamics has also been described. Dimensionless numbers capable of characterizing the single bubble and bubble stream passage process were identified and used to map the flow regimes. Flow regime transition criteria were then identified based on this dimensionless mapping and the experimental results.

ii. A numerical model for bubble growth within a droplet contained in a superheated bath of a second immiscible liquid was developed by solving the mass and energy equations. The model considered the growth process using a one-dimensional radial model in which the bubble is completely engulfed by the evaporating liquid. The effect of pressure-driven bubble growth was shown to be minimal and is therefore ignored to significantly simplify the modeling process. Unlike previous models which assumed a constant initial superheat within the drop, the initial conditions for this model were found by solving the radial heat conduction equation. This enables a wide range of experimental conditions to be accounted for in the model. The model was validated using high-speed videos of bubble growth in an FC-72 droplet introduced into a bath of heated water captured experimentally. The model is found to be in close agreement with this experimental data as well as various cases found in literature. A parametric study was then carried out to identify the influence of liquid superheat, initial droplet configuration, and thermal conductivity and thermal mass ratios of the two liquids.

iii. Dimensionless characterization of bubble collisions with a solid surface and a free surface was carried out as a means to predict the radial size of the film formed at impact.

This film size is a crucial parameter of the collision and is known to play a role in defining critical processes such as the film drainage rate. However, this film size is not an easily attainable experimental measurement and requires advances instrumentation to capture. Using the relevant parameters, Buckingham pi theorem was applied to identify the dimensionless number capable of characterizing the collision process. These numbers were found to be the Bond, Archimedes, and Froude numbers, as well as the ratio of the film force to the buoyancy force. Numerical modeling was then employed to identify the relationship between these dimensionless numbers, and a quasi-static model is employed to relate the film force to the film radius. Experiments were carried out using interferometry to capture the radial film size during the collision of a bubble with a glass surface. The film radii captured during these experiments were found to mostly be within ±20% of the theoretically predicted values. A least squares regression analysis was carried out to allow the maximum film radius attained during impact with a solid surface or a free surface to be predicted using easily measurable experimental parameters.

iv. Three numerical models were developed to predict the bubble trajectory and film drainage occurring during the impact of a bubble with a liquid-liquid, solid-liquid-liquid, or gas-liquid-liquid interface. A simple force balance model is employed to capture the bubble motion while the Stokes-Reynolds-Young-Laplace equations are employed to derive predictive expressions for the pressure buildup in the film(s) formed at impact and the associated drainage rate(s). Experimental tests were carried out using three different liquid combinations under various interface conditions to validate the model. These results, as well as experimental data from literature, are found to be in reasonable agreement with the model predictions. This type of modeling represents a significant simplification in terms of solving complexity compared to typical grid-based simulations but nonetheless is able to capture very complex phenomena associated with the collision process.

v. The findings from this work have been published in three journal articles [118–120].

## 5.2 Future Recommendations

In this work, several different aspects of bubble interactions with multi-fluid interfaces were considered. This included identifying and classifying flow regimes associated with single bubble and bubble stream passage through a liquid-liquid interface, the derivation of a numerical model for immiscible bubble growth, the identification and implementation of dimensionless quantities for characterizing bubble collisions at free and solid surfaces, and the development of three numerical models for bubble collisions at liquid-liquid, solid-liquid-liquid, and gas-liquid-liquid interfaces. Some recommendations for future research related to these subjects are presented here:

*Applications of bubble stream passage:* The passage of bubble streams through a liquid-liquid interface have received very little attention. As a result, there has been very little consideration on the possible applications of specific flow patterns. Specifically, the formation of a stable liquid column identified here presents a fascinating phenomenon that could have many potential uses in areas such as direct contact evaporation or liquid-liquid extraction. In addition to the geometric formation creating additional surface area for heat or mass transfer to occur, the added liquid motion provided by the bubbles could aid in improving these processes as well. The identification and exploration of these possible applications presents one possible area for future research.

*Influence of surface-active substances on bubble collisions at multi-liquid interfaces:* The presence of surface-active substances has been shown to cause significant changes in bubble behavior during is collision with free and solid surfaces [85]. Some initial investigations have recently been made on these effects at a liquid-liquid interface [117], but further analysis is needed to provide a comprehensive understanding of these effects on liquid-liquid interface collisions, as well as on compound interface collisions. This could be done through exhaustive experimental testing. Since multiple liquids are involved in these systems, the effects of which liquid the substance is present in could also be explored.

*Pressure measurement in thin liquid films:* The spatiotemporal evolution of the thin liquid film formed during the collision of a bubble with a solid surface was recently examined using interferometry [9,51]. With the recent advances in micromanufacturing capabilities [121–124], a microelectronic device could be made to provide similar spatiotemporal information of the pressure buildup in the thin liquid film. This would provide newfound insight into thin film drainage phenomena and provide direct validation for the existing thin film pressure models.

*Forces acting on a bubble in proximity to a liquid-liquid interface:* As noted in Section 4.4.1, the influence of the top liquid properties on the forces acting on a bubble during its collision with a liquid-liquid interface are not yet well-understood. The improvement of this understanding would aid significantly in providing accurate yet simple models for capturing bubble collisions at liquid-liquid interfaces that do not rely on experimentally determined fitting parameters.

*Dimensionless characterization of bubble collisions at liquid-liquid and compound interfaces:* A similar process to the analysis described here in Section 4.3 for bubble collisions at free and solid surfaces could be carried out for bubble collisions at liquid-liquid and compound interfaces. As outlined by Bonhomme et al. [18], six dimensionless parameters can be used to characterize the systems assuming the bubble viscosity and density are negligible. This number could, perhaps, be further reduced by considering which parameters hold more value in dictating the collision process. Once identified, the numerical models outlined here in Section 4.4 may be used to generate dimensionless maps of bubble collisions at liquid-liquid and compound interfaces. The information provided by these maps would be highly useful for implementing these systems for practical purposes.

# 6 References

[1] Prosperetti, A., 2004, “Bubbles,” Physics of Fluids, **16**(6), pp. 1852–1865.

[2] Young Thomas, 1805, “III. An Essay on the Cohesion of Fluids,” Philosophical Transactions of the Royal Society of London, **95**, pp. 65–87.

[3] Laplace, P. S., 1806, *Mécanique céleste*, Chez J.B.M. Duprat.

[4] Reynolds, O., 1886, “On the Theory of Lubrication and Its Application to Mr. Beauchamp Tower’s Experiments, Including an Experimental Determination of the Viscosity of Olive Oil.,” Proc. R. Soc. Lond., **40**(242–245), pp. 191–203.

[5] Basset, A., 1888, “Chapter XXII,” *A Treatise on Hydrodynamics, Vol II*, Deighton, Bell and sons.

[6] Yang, S., and Leal, L. G., 1991, “A Note on Memory-integral Contributions to the Force on an Accelerating Spherical Drop at Low Reynolds Number,” Physics of Fluids A: Fluid Dynamics, **3**(7), pp. 1822–1824.

[7] Exerowa, D., and Kruglyakov, P. M., 1997, “Foam and Foam Films,” *Foam and Foam Films: Theory, Experiment, Application*, Elsevier, pp. 122–166.

[8] Manica, R., Parkinson, L., Ralston, J., and Chan, D. Y. C., 2010, “Interpreting the Dynamic Interaction between a Very Small Rising Bubble and a Hydrophilic Titania Surface,” J. Phys. Chem. C, **114**(4), pp. 1942–1946.

[9] Hendrix, M. H. W., Manica, R., Klaseboer, E., Chan, D. Y. C., and Ohl, C.-D., 2012, “Spatiotemporal Evolution of Thin Liquid Films during Impact of Water Bubbles on Glass on a Micrometer to Nanometer Scale,” Phys. Rev. Lett., **108**(24), p. 247803.

[10] Chesters, A. K., and Hofman, G., 1982, “Bubble Coalescence in Pure Liquids,” Applied Scientific Research, **38**(1), pp. 353–361.

[11] Ivanov, I. B., Dimitrov, D. S., Somasundaran, P., and Jain, R. K., 1985, “Thinning of Films with Deformable Surfaces: Diffusion-Controlled Surfactant Transfer,” Chemical Engineering Science, **40**(1), pp. 137–150.

[12] Greene, G., Chen, J., and Conlin, M., 1988, “Onset of Entrainment Between Immiscible Liquid Layers Due to Rising Gas-Bubbles,” Int. J. Heat Mass Transf., **31**(6), pp. 1309–1317.

[13] Greene, G., Chen, J., and Conlin, M., 1991, “Bubble Induced Entrainment Between Stratified Liquid Layers,” Int. J. Heat Mass Transf., **34**(1), pp. 149–157.

[14] Reiter, G., and Schwerdtfeger, K., 1992, “Characteristics of Entrainment at Liquid Liquid Interfaces Due to Rising Bubbles,” ISIJ Int., **32**(1), pp. 57–65.

[15] Reiter, G., and Schwerdtfeger, K., 1992, “Observations of Physical Phenomena Occurring During Passage of Bubbles Through Liquid Liquid Interfaces,” ISIJ Int., **32**(1), pp. 50–56.

[16] Natsui, S., Takai, H., Kumagai, T., Kikuchi, T., and Suzuki, R. O., 2014, “Multiphase Particle Simulation of Gas Bubble Passing Through Liquid/Liquid Interfaces,” Mater. Trans., **55**(11), pp. 1707–1715.

[17] Singh, K. K., Gebauer, F., and Bart, H.-J., 2017, “Bouncing of a Bubble at a Liquid-Liquid Interface,” AICHE J., **63**(7), pp. 3150–3157.

[18] Bonhomme, R., Magnaudet, J., Duval, F., and Piar, B., 2012, "Inertial Dynamics of Air Bubbles Crossing a Horizontal Fluid-Fluid Interface," J. Fluid Mech., **707**, pp. 405–443.

[19] Singh, K. K., and Bart, H.-J., 2015, "Passage of a Single Bubble through a Liquid-Liquid Interface," Ind. Eng. Chem. Res., **54**(38), pp. 9478–9493.

[20] Dietrich, N., Poncin, S., Pheulpin, S., and Li, H. Z., 2008, "Passage of a Bubble through a Liquid-Liquid Interface," AICHE J., **54**(3), pp. 594–600.

[21] Manga, M., Stone, H. A., and O'Connell, R. J., 1993, "The Interaction of Plume Heads with Compositional Discontinuities in the Earth's Mantle," J. Geophys. Res., **98**(B11), pp. 19979–19990.

[22] Kawano, S., Hashimoto, H., Ihara, A., and Shin, K., 1996, "Sequential Production of Mm-Sized Spherical Shells in Liquid-Liquid Gas Systems," J. Fluids Eng.-Trans. ASME, **118**(3), pp. 614–618.

[23] Han, Z. J., and Holappa, L., 2003, "Mechanisms of Iron Entrainment into Slag Due to Rising Gas Bubbles," ISIJ Int., **43**(3), pp. 292–297.

[24] Szekely, J., 1963, "Mathematical Model for Heat or Mass Transfer at the Bubble-Stirred Interface of Two Immiscible Liquids," International Journal of Heat and Mass Transfer, **6**(5), pp. 417–422.

[25] Hirasawa, M., Mori, K., Sano, M., Hatanaka, A., Shimatani, Y., and Okazaki, Y., 1987, "Rate of Mass-Transfer Between Molten Slag and Metal Under Gas Injection Stirring," Transactions of the Iron and Steel Institute of Japan, **27**(4), pp. 277–282.

[26] Kim, S., and Fruehan, R., 1987, "Physical Modeling of Liquid Liquid Mass-Transfer in Gas Stirred Ladles," Metallurgical Transactions B-Process Metallurgy, **18**(2), pp. 381–390.

[27] Chevrier, V., and Cramb, A. W., 2004, "Observation and Measurement of Bubble Separation at Liquid-Liquid Interfaces," steel research international, **75**(10), pp. 645–658.

[28] Richardson, F. D., 1971, "Drops and Bubbles in Extractive Metallurgy," MT, **2**(10), pp. 2747–2756.

[29] Song, D.-Y., Maruoka, N., Gupta, G. S., Shibata, H., Kitamura, S.-Y., and Kamble, S., 2012, "Modeling of Ascending/Descending Velocity of Metal Droplet Emulsified in Pb-Salt System," Metall and Materi Trans B, **43**(4), pp. 973–983.

[30] Mercier, J. L., da Cunha, F. M., Teixeira, J. C., and Scofield, M. P., 1974, "Influence of Enveloping Water Layer on the Rise of Air Bubbles in Newtonian Fluids," J. Appl. Mech, **41**(1), pp. 29–34.

[31] Hashimoto, H., and Kawano, S., 1990, "A Study on Encapsulated Liquid-Drop Formation in Liquid Liquid Gas Systems (Fundamental Mechanism of Encapsulated Drop Formation)," Jsme International Journal Series Ii-Fluids Engineering Heat Transfer Power Combustion Thermophysical Properties, **33**(4), pp. 729–735.

[32] Kawano, S., and Hashimoto, H., 1992, "Drag Coefficient of a Spherical Encapsulated Liquid-Drop," Jsme International Journal Series Ii-Fluids Engineering Heat Transfer Power Combustion Thermophysical Properties, **35**(2), pp. 151–157.

[33] Kawano, S., Hashimoto, H., and Suyama, T., 1994, "Buoyancy-Driven Accelerated Motion of an Encapsulated Liquid-Drop," JSME Int. J. Ser. B-Fluids Therm. Eng., **37**(1), pp. 30–37.

[34] Kawano, S., Hashimoto, H., Ihara, A., and Azima, T., 1997, “Small-Amplitude Oscillations of Encapsulated Liquid Drop Interfaces,” JSME Int. J. Ser. B-Fluids Therm. Eng., **40**(1), pp. 33–41.

[35] Kawano, S., Shirai, A., and Nagasaka, S., 2007, “Deformations of Thin Liquid Spherical Shells in Liquid-Liquid-Gas Systems,” Phys. Fluids, **19**(1), p. 012105.

[36] Lee, M. C., Kendall, J. M., Jr., Bahrami, P. A., and Wang, T. G., 1986, “Sensational Spherical Shells,” Aerospace America, **24**, pp. 72–74.

[37] Baqir, A. Sh., Mahood, H. B., Campbell, A. N., and Griffiths, A. J., 2016, “Measuring the Average Volumetric Heat Transfer Coefficient of a Liquid–Liquid–Vapour Direct Contact Heat Exchanger,” Applied Thermal Engineering, **103**, pp. 47–55.

[38] Sideman, S., and Gat, Y., 1966, “Direct Contact Heat Transfer with Change of Phase: Spray-Column Studies of a Three-Phase Heat Exchanger,” AIChE J., **12**(2), pp. 296–303.

[39] Moore, G. R., 1959, “Vaporization of Superheated Drops in Liquids,” AIChE J., **5**(4), pp. 458–466.

[40] Sideman, S., Hirsch, G., and Gat, Y., 1965, “Direct Contact Heat Transfer with Change of Phase: Effect of the Initial Drop Size in Three-Phase Heat Exchangers,” AIChE J., **11**(6), pp. 1081–1087.

[41] Seetharamu, K. N., and Battya, P., 1989, “Direct Contact Evaporation Between Two Immiscible Liquids in a Spray Column,” J. Heat Transfer, **111**(3), pp. 780–785.

[42] R E Johnson, and Sadhal, and S. S., 1985, “Fluid Mechanics of Compound Multiphase Drops and Bubbles,” Annual Review of Fluid Mechanics, **17**(1), pp. 289–320.

[43] Feng, J., Roché, M., Vigolo, D., Arnaudov, L. N., Stoyanov, S. D., Gurkov, T. D., Tsutsumanova, G. G., and Stone, H. A., 2014, “Nanoemulsions Obtained via Bubble-Bursting at a Compound Interface,” Nature Physics, **10**(8), pp. 606–612.

[44] Feng, J., Nunes, J. K., Shin, S., Yan, J., Kong, Y. L., Prud’homme, R. K., Arnaudov, L. N., Stoyanov, S. D., and Stone, H. A., 2016, “A Scalable Platform for Functional Nanomaterials via Bubble-Bursting,” Advanced Materials, **28**(21), pp. 4047–4052.

[45] Cunliffe, M., Engel, A., Frka, S., Gašparović, B., Guitart, C., Murrell, J. C., Salter, M., Stolle, C., Upstill-Goddard, R., and Wurl, O., 2013, “Sea Surface Microlayers: A Unified Physicochemical and Biological Perspective of the Air–Ocean Interface,” Progress in Oceanography, **109**, pp. 104–116.

[46] Feng, J., Muradoglu, M., Kim, H., Ault, J. T., and Stone, H. A., 2016, “Dynamics of a Bubble Bouncing at a Liquid/Liquid/Gas Interface,” Journal of Fluid Mechanics, **807**, pp. 324–352.

[47] Chan, D. Y. C., Klaseboer, E., and Manica, R., 2011, “Film Drainage and Coalescence between Deformable Drops and Bubbles,” Soft Matter, **7**(6), pp. 2235–2264.

[48] Chan, D. Y. C., Klaseboer, E., and Manica, R., 2011, “Theory of Non-Equilibrium Force Measurements Involving Deformable Drops and Bubbles,” Adv Colloid Interface Sci, **165**(2), pp. 70–90.

[49] Derjaguin, B., and Landau, L., 1993, "Theory of the Stability of Strongly Charged Lyophobic Sols and of the Adhesion of Strongly Charged Particles in Solutions of Electrolytes," Progress in Surface Science, **43**(1), pp. 30–59.

[50] Verwey, E. J. W., Overbeek, joint author.), J. T. G. (Jan Theodor Gerard, and Nes, joint author.), K. va, 1948, *Theory of the Stability of Lyophobic Colloids : The Interaction of Sol Particles Having an Electric Double Layer*, New York, Elsevier Pub. Co.

[51] Manica, R., W. Hendrix, M. H., Gupta, R., Klaseboer, E., Ohl, C.-D., and C. Chan, D. Y., 2013, "Effects of Hydrodynamic Film Boundary Conditions on Bubble–Wall Impact," Soft Matter, **9**(41), pp. 9755–9758.

[52] Karakashev, S. I., and Manev, E. D., 2015, "Hydrodynamics of Thin Liquid Films: Retrospective and Perspectives," Advances in Colloid and Interface Science, **222**, pp. 398–412.

[53] Manica, R., Klaseboer, E., and Chan, D. Y. C., 2016, "The Hydrodynamics of Bubble Rise and Impact with Solid Surfaces," Advances in Colloid and Interface Science, **235**, pp. 214–232.

[54] Scheludko, A., 1957, "über das Ausfließen der Lösung aus Schaumfilmen," Kolloid-Zeitschrift, **155**(1), pp. 39–44.

[55] Tsekov, R., 1998, "The R4/5-Problem in the Drainage of Dimpled Thin Liquid Films," Colloids and Surfaces A: Physicochemical and Engineering Aspects, **141**(2), pp. 161–164.

[56] Tsekov, R., 1999, "Drainage of Foam Films," *Foams and Emulsions*, J.F. Sadoc, and N. Rivier, eds., Springer Netherlands, pp. 83–90.

[57] Manev, E., Tsekov, R., and Radoev, B., 1997, "Effect of Thickness Non-Homogeneity on the Kinetic Behaviour of Microscopic Foam Film," Journal of Dispersion Science and Technology, **18**(6–7), pp. 769–788.

[58] Nicolson, M. M., 1949, "The Interaction between Floating Particles," Mathematical Proceedings of the Cambridge Philosophical Society, **45**(2), pp. 288–295.

[59] Chappelear, D. C., 1961, "Models of a Liquid Drop Approaching an Interface," Journal of Colloid Science, **16**, pp. 186–190.

[60] Princen, H. M., 1963, "Shape of a Fluid Drop at a Liquid-Liquid Interface," Journal of Colloid Science, **18**(2), pp. 178–195.

[61] Ivanov, I. B., Radeov, B. P., Traykov, T., Dimitrov, D., Manev, E., and Vassilieff, C., 1975, "Hydrodynamics of Foam and Emulsion Films," *International Conference on Colloid and Surface Science*, Budapest, Hungary, pp. 583–590.

[62] Zawala, J., and Malysa, K., 2011, "Influence of the Impact Velocity and Size of the Film Formed on Bubble Coalescence Time at Water Surface," Langmuir, **27**(6), pp. 2250–2257.

[63] Duangsuwan, W., Tüzün, U., and Sermon, P. A., 2010, "Feasibility of N2/Sunflower Oil Compound Drop Formation in Methanol Induced by Bubble Train," AIChE J., **56**(12), pp. 3274–3278.

[64] Kemiha, M., Olmos, E., Fei, W., Poncin, S., and Li, H. Z., 2007, "Passage of a Gas Bubble through a Liquid-Liquid Interface," Ind. Eng. Chem. Res., **46**(19), pp. 6099–6104.

[65] Hartland, S., 1969, “The Profile of the Draining Film between a Rigid Sphere and a Deformable Fluid-Liquid Interface,” Chemical Engineering Science, **24**(6), pp. 987–995.

[66] Maru, H. C., Wasan, D. T., and Kintner, R. C., 1971, “Behavior of a Rigid Sphere at a Liquid—Liquid Interface,” Chemical Engineering Science, **26**(10), pp. 1615–1628.

[67] Kondur, R., and Shaw, J. M., 1990, “The Behaviour of Large Gas Bubbles at a Liquid-Liquid Interface. Part-1: The Entrainment of Liquid Drops,” *Materials Handling in Pyrometallurgy*, C. Twigge-Molecey, and T. Price, eds., Pergamon, Oxford, pp. 14–24.

[68] Shaw, J. M., and Konduru, R., 1992, “The Behaviour of Large Gas Bubbles at a Liquid-Liquid Interface. Part 2: Liquid Entrainment,” Can. J. Chem. Eng., **70**(2), pp. 381–384.

[69] Uemura, T., Ueda, Y., and Iguchi, M., 2010, “Ripples on a Rising Bubble through an Immiscible Two-Liquid Interface Generate Numerous Micro Droplets,” EPL, **92**(3), p. 34004.

[70] Manga, M., and Stone, H., 1995, “Low-Reynolds-Number Motion of Bubbles, Drops and Rigid Spheres Through Fluid-Fluid Interfaces,” J. Fluid Mech., **287**, pp. 279–298.

[71] Mori, Y. H., 1978, “Configurations of Gas-Liquid Two-Phase Bubbles in Immiscible Liquid Media,” International Journal of Multiphase Flow, **4**(4), pp. 383–396.

[72] Avedisian, C. T., and Andres, R. P., 1978, “Bubble Nucleation in Superheated Liquid—Liquid Emulsions,” Journal of Colloid and Interface Science, **64**(3), pp. 438–453.

[73] Sideman, S., and Taitel, Y., 1964, “Direct-Contact Heat Transfer with Change of Phase: Evaporation of Drops in an Immiscible Liquid Medium,” International Journal of Heat and Mass Transfer, **7**(11), pp. 1273–1289.

[74] Tochitani, Y., Mori, Y. H., and Komotori, K., 1977, “Vaporization of Single Liquid Drops in an Immiscible Liquid Part I: Forms and Motions of Vaporizing Drops,” Warme- und Stoffubertragung, **10**(1), pp. 51–59.

[75] Tochitani, Y., Nakagawa, T., Mori, Y. H., and Komotori, K., 1977, “Vaporization of Single Liquid Drops in an Immiscible Liquid Part II: Heat Transfer Characteristics,” Warme- und Stoffubertragung, **10**(2), pp. 71–79.

[76] Raina, G. K., and Grover, P. D., 1982, “Direct Contact Heat Transfer with Change of Phase: Theoretical Model,” AIChE J., **28**(3), pp. 515–517.

[77] Battya, P., Raghavan, V. R., and Seetharamu, K. N., 1984, “Parametric Studies on Direct Contact Evaporation of a Drop in an Immiscible Liquid,” International Journal of Heat and Mass Transfer, **27**(2), pp. 263–272.

[78] Haustein, H. D., Gany, A., and Elias, E., 2009, “Rapid Boiling of a Two-Phase Droplet in an Immiscible Liquid at High Superheat,” J. Heat Transfer, **131**(12), pp. 121010-121010–7.

[79] Avedisian, C., and Suresh, K., 1985, “Analysis of Non-Explosive Bubble-Growth Within a Superheated Liquid Droplet Suspended in an Immiscible Liquid,” Chem. Eng. Sci., **40**(12), pp. 2249–2259.

[80] Roesle, M. L., and Kulacki, F. A., 2010, “Boiling of Small Droplets,” International Journal of Heat and Mass Transfer, **53**(23), pp. 5587–5595.

[81] Zawala, J., Dorbolo, S., Terwagne, D., Vandewalle, N., and Malysa, K., 2011, “Bouncing Bubble on a Liquid/Gas Interface Resting or Vibrating,” Soft Matter, **7**(14), pp. 6719–6726.

[82] Zawala, J., Dorbolo, S., Vandewalle, N., and Malysa, K., 2013, “Bubble Bouncing at a Clean Water Surface,” Phys. Chem. Chem. Phys., **15**(40), pp. 17324–17332.

[83] Zawala, J., 2016, “‘Immortal’ Liquid Film Formed by Colliding Bubble at Oscillating Solid Substrates,” Physics of Fluids, **28**(5), p. 057103.

[84] Loth, E., 2008, “Quasi-Steady Shape and Drag of Deformable Bubbles and Drops,” Int. J. Multiph. Flow, **34**(6), pp. 523–546.

[85] Malysa, K., Krasowska, M., and Krzan, M., 2005, “Influence of Surface Active Substances on Bubble Motion and Collision with Various Interfaces,” Advances in Colloid and Interface Science, **114–115**, pp. 205–225.

[86] “Super Low Viscosity Pure Silicone Fluids” [Online]. Available: http://www.clearcoproducts.com/pure-silicone-super-low-viscosity.html. [Accessed: 06-Mar-2019].

[87] “Low Viscosity Pure Silicone Fluids” [Online]. Available: http://www.clearcoproducts.com/pure-silicone-low-viscosity.html. [Accessed: 06-Mar-2019].

[88] “Medium Viscosity Pure Silicone Fluids” [Online]. Available: http://www.clearcoproducts.com/pure-silicone-standard-viscosity.html. [Accessed: 06-Mar-2019].

[89] “F2 Chemicals Ltd: Flutec PP1” [Online]. Available: http://f2chemicals.com/flutec_pp1.html. [Accessed: 06-Mar-2019].

[90] Manica, R., Klaseboer, E., and Chan, D. Y. C., 2016, “The Impact and Bounce of Air Bubbles at a Flat Fluid Interface,” Soft Matter, **12**(13), pp. 3271–3282.

[91] Chaudhury, K. N., and Dabhade, S. D., 2016, “Fast and Provably Accurate Bilateral Filtering,” IEEE Transactions on Image Processing, **25**(6), pp. 2519–2528.

[92] Yakhshi-Tafti, E., Kumar, R., and Cho, H. J., 2011, “Measurement of Surface Interfacial Tension as a Function of Temperature Using Pendant Drop Images,” International Journal of Optomechatronics, **5**(4), pp. 393–403.

[93] Zawala, J., Krasowska, M., Dabros, T., and Malysa, K., 2007, “Influence of Bubble Kinetic Energy on Its Bouncing During Collisions with Various Interfaces,” Can. J. Chem. Eng., **85**(5), pp. 669–678.

[94] Manev, E. D., and Angarska, J. K., 2005, “Critical Thickness of Thin Liquid Films: Comparison of Theory and Experiment,” Colloids and Surfaces A: Physicochemical and Engineering Aspects, **263**(1–3), pp. 250–257.

[95] Klaseboer, E., Chevaillier, J.-P., Maté, A., Masbernat, O., and Gourdon, C., 2000, “Model and Experiments of a Drop Impinging on an Immersed Wall,” Physics of Fluids, **13**(1), pp. 45–57.

[96] Tsao, H., and Koch, D. L., 1997, “Observations of High Reynolds Number Bubbles Interacting with a Rigid Wall,” Physics of Fluids, **9**(1), pp. 44–56.

[97] Sinn, N., Alishahi, M., and Hardt, S., 2015, “Detachment of Particles and Particle Clusters from Liquid/Liquid Interfaces,” Journal of Colloid and Interface Science, **458**, pp. 62–68.

[98] Alterman, Z., 1961, “Effect of Surface Tension on the Kelvin-Helmholtz Instability of Two Rotating Fluids,” Proc Natl Acad Sci U S A, **47**(2), pp. 224–227.

[99] Díaz-Damacillo, L., Ruiz-Angulo, A., and Zenit, R., 2016, “Drift by Air Bubbles Crossing an Interface of a Stratified Medium at Moderate Reynolds Number,” International Journal of Multiphase Flow, **85**, pp. 258–266.

[100] Duda, J. L., Malone, M. F., Notter, R. H., and Vrentas, J. S., 1975, “Analysis of Two-Dimensional Diffusion-Controlled Moving Boundary Problems,” International Journal of Heat and Mass Transfer, **18**(7), pp. 901–910.

[101] Apfel, R. E., 1971, “Vapor Nucleation at a Liquid–Liquid Interface,” The Journal of Chemical Physics, **54**(1), pp. 62–63.

[102] Baqir, A. S., Griffiths, A. J., and Rageb, A. A., 2011, “Vaporization of Single N-Pentane Liquid Drop in a Flowing Distilled,” College of Engineering, University of Babylon.

[103] Avedisian, C. T., 1982, “Effect of Pressure on Bubble Growth Within Liquid Droplets at the Superheat Limit,” J. Heat Transfer, **104**(4), pp. 750–757.

[104] Wang, L., and Qu, X., 2012, “Impact of Interface Approach Velocity on Bubble Coalescence,” Minerals Engineering, **26**, pp. 50–56.

[105] Kirkpatrick, R. D., and Lockett, M. J., 1974, “The Influence of Approach Velocity on Bubble Coalescence,” Chemical Engineering Science, **29**(12), pp. 2363–2373.

[106] Sanada, T., Watanabe, M., and Fukano, T., 2005, “Effects of Viscosity on Coalescence of a Bubble upon Impact with a Free Surface,” Chemical Engineering Science, **60**(19), pp. 5372–5384.

[107] Traykov, T. T., and Ivanov, I. B., 1977, “Hydrodynamics of Thin Liquid Films. Effect of Surfactants on the Velocity of Thinning of Emulsion Films,” International Journal of Multiphase Flow, **3**(5), pp. 471–483.

[108] Langevin, D., 2015, “Bubble Coalescence in Pure Liquids and in Surfactant Solutions,” Current Opinion in Colloid & Interface Science, **20**(2), pp. 92–97.

[109] Giribabu, K., Reddy, M. L. N., and Ghosh, P., 2007, “Coalescence of Air Bubbles in Surfactant Solutions: Role of Salts Containing Mono-, Di-, and Trivalent Ions,” Chemical Engineering Communications, **195**(3), pp. 336–351.

[110] Kosior, D., Zawala, J., and Malysa, K., 2014, “Influence of N-Octanol on the Bubble Impact Velocity, Bouncing and the Three Phase Contact Formation at Hydrophobic Solid Surfaces,” Colloids and Surfaces A: Physicochemical and Engineering Aspects, **441**, pp. 788–795.

[111] Manica, R., Klaseboer, E., and Chan, D. Y. C., 2015, “Force Balance Model for Bubble Rise, Impact, and Bounce from Solid Surfaces,” Langmuir, **31**(24), pp. 6763–6772.

[112] Buckingham, E., 1914, “On Physically Similar Systems; Illustrations of the Use of Dimensional Equations,” Phys. Rev., **4**(4), pp. 345–376.

[113] Moore, D. W., 1965, “The Velocity of Rise of Distorted Gas Bubbles in a Liquid of Small Viscosity,” Journal of Fluid Mechanics, **23**(4), pp. 749–766.

[114] Kosior, D., Zawala, J., Todorov, R., Exerowa, D., and Malysa, K., 2014, “Bubble Bouncing and Stability of Liquid Films Formed under Dynamic and Static Conditions from N-Octanol Solutions,” Colloids and Surfaces A: Physicochemical and Engineering Aspects, **460**, pp. 391–400.

[115] Abramowitz, M., and Stegun, I. A., 1972, *Handbook of Mathematical Functions*.

[116] Kharlamov, A. A., Chára, Z., and Vlasák, P., 2008, “Hydraulic Formulae for the Added Masses of an Impermeable Sphere Moving near a Plane Wall,” J Eng Math, **62**(2), p. 161.

[117] Vakarelski, I. U., Manica, R., Li, E. Q., Basheva, E. S., Chan, D. Y. C., and Thoroddsen, S. T., 2018, “Coalescence Dynamics of Mobile and Immobile Fluid Interfaces,” Langmuir, **34**(5), pp. 2096–2108.

[118] Emery, T. S., Raghupathi, P. A., and Kandlikar, S. G., 2018, “Flow Regimes and Transition Criteria during Passage of Bubbles through a Liquid–Liquid Interface,” Langmuir, **34**(23), pp. 6766–6776.

[119] Emery, T. S., Raghupathi, P. A., and Kandlikar, S. G., 2018, “Bubble Growth inside an Evaporating Liquid Droplet Introduced in an Immiscible Superheated Liquid,” International Journal of Heat and Mass Transfer, **127**, pp. 313–321.

[120] Emery, T. S., and Kandlikar, S. G., 2019, “Film Size During Bubble Collision With a Solid Surface,” J. Fluids Eng, **141**(7), pp. 071302-071302–8.

[121] Wang, Q., Lu, Y., Mishin, S., Oshmyansky, Y., and Horsley, D. A., 2017, “Design, Fabrication, and Characterization of Scandium Aluminum Nitride-Based Piezoelectric Micromachined Ultrasonic Transducers,” Journal of Microelectromechanical Systems, **26**(5), pp. 1132–1139.

[122] Angel, S., and Daniel, R. J., 2017, “Sensitivity Enhancement by Striped Arrow Embossed Diaphragms in Low Pressure MEMS Piezoresistive Pressure Sensors,” *2017 Trends in Industrial Measurement and Automation (TIMA)*, pp. 1–5.

[123] Jang, M., and Yun, K.-S., 2017, “MEMS Capacitive Pressure Sensor Monolithically Integrated with CMOS Readout Circuit by Using Post CMOS Processes,” Micro and Nano Systems Letters, **5**(1), p. 4.

[124] Havreland, A. S., Petersen, S. D., Østergaard, C., Reck-Nielsen, K., and Thomsen, E. V., 2017, “Micro-Fabricated All Optical Pressure Sensors,” Microelectronic Engineering, **174**, pp. 11–15.

# Chapter 7

# 7 Appendix

## 7.1 Matlab Code for Pendant Drop Analysis

The numerical code written in Matlab for the pendant drop analysis used to determine the interfacial tensions of the liquid combinations is outlined in this section. There are two files needed to run this analysis: one main controlling file that performs most of the image processing and curve fitting, and one function used for Gaussian bilateral filtering. Once the image is read in and converted to grayscale, it undergoes four operations. First, Gaussian bilateral filtering is performed to smooth the image while preserving the edges. An approximate method developed by Chaudhury and Dabhade [91] is implemented with their associated code. The image is then binarized, holes in the image are filled, and Canny edge detection is performed using built in Matlab functions. The drop apex location and experimental drop profile are then extracted from the edge detection. Equation 16 is then solved over a wide range of $a$ and $\omega$ values to get the associated theoretical drop profile. A brute force optimization is used to determine the best fit theoretical profile based on the residuals calculated using Equation 17. The $\omega$ value associated with the theorical profile that has the minimum error is then used to determine the interfacial tension.

### *7.1.1 Main Controlling File*

```
% Travis S. Emery
% Pendant Drop Analysis
tic
close all
clear
clc
% User inputs
cal=0.0000184; % Spatial calibration [m/px]
delrho=1000; % density difference [kg/m^3]
Img=rgb2gray(imread('Water_S01.jpg'));
% Gaussian Bilateral Filtering
sigmar=25; % width of range Gaussian
sigmas=25; % width of spatial Gaussian
```

```
eps=1e-3; % kernel approximation accuracy
[Smooth,~]=GPA(double(Img),sigmar,sigmas,eps,'Gauss');
% Binarize Image
Bin=~imbinarize(uint8(Smooth),adaptthresh(uint8(Smooth),0.4,...
    'ForegroundPolarity','dark','NeighborhoodSize',65));
% Fill holes
Fill=imfill(Bin,'holes');
% Canny edge detection
Edge=edge(Fill,'canny');
% Get apex location, first non-zero row from bottom is Y0, average of
% edge locations in that row is X0
Y0=length(Img(:,1))-find(flipud(sum(Edge,2)),1)+1;
X0=mean(find(Edge(Y0,:)));
% Get left and right contours, adjusted to start at (0,0)
y=(0:Y0-2).'; % -2 b/c starting at zero and no edge in first row
xl=zeros(size(y));
xr=zeros(size(y));
for i=2:Y0
    temp=find(Edge(i,:));
    xl(Y0+1-i)=X0-temp(1);
    xr(Y0+1-i)=temp(end)-X0;
end
% Get index of drop top
for i=length(xr):-1:1
    if xr(i)>=xr(end)+3
        top=i;
        break
    end
end
% Brute force profile optimization
sspan=linspace(0,pi,1000);
omegatest=0.05:0.001:0.4;
atest=floor(0.8*max(xr+xl)/2):0.1:ceil(1.1*max(xr+xl)/2);
xprof=zeros(length(sspan),length(omegatest),length(atest));
yprof=zeros(length(sspan),length(omegatest),length(atest));
omegares=zeros(length(omegatest),length(atest));
sol0=[eps;eps;eps];
for i=1:length(omegatest)
    [~,sol]=ode45(@(s,y) f(s,y,omegatest(i)),sspan,sol0);
    for j=1:length(atest)
        xprof(:,i,j)=atest(j)*sol(:,1);
        yprof(:,i,j)=atest(j)*sol(:,2);
        ymax=min(top,floor(yprof(end,i,j)));
        xtest=interp1(yprof(:,i,j),xprof(:,i,j),y(1:ymax),...
            'linear','extrap');
        omegares(i,j)=sum((xtest-xr(1:ymax)).^2+(xtest-xl(1:ymax)).^2);
    end
end
[~,minidx]=min(omegares(:));
[minrow,mincol]=ind2sub(size(omegares),minidx);
a=atest(mincol);
omega=omegatest(minrow);
sigma=delrho*9.81*(cal*a)^2/omega;

% Graphing
% Image after each successive step
figure(1)
```

```
set(gcf,'color','w');
subplot(2,3,1)
imshow(Img)
title('Original Image')
subplot(2,3,2)
imshow(uint8(Smooth))
title('Smoothed')
subplot(2,3,3)
imshow(Bin)
title('Binarized')
subplot(2,3,4)
imshow(Fill)
title('Holes Filled')
subplot(2,3,5)
imshow(Edge)
title('Canny Edge Detection')
% Contour plot of residuals
figure(2)
set(gcf,'color','w');
contour(atest,omegatest,log(omegares))
xlabel('Radius (px)')
ylabel('\beta')
title('Contour plot of residuals for fit curves')
set(gca,'fontsize',18)
% Smoothed image with overlaid theoretical profile
figure(3)
set(gcf,'color','w');
imshow(uint8(Smooth));
hold on
th=0:pi/50:2*pi;
xcirc=a*cos(th)+X0;
ycirc=a*sin(th)+Y0-a;
plot(xcirc,ycirc,'linewidth',2)
plot(xprof(:,minrow,mincol)+X0,Y0-yprof(:,minrow,mincol),'linewidth',2)
title(['Pendant Drop Analysis, \sigma_I = ' ...
    num2str(round(sigma*10000)/10) ' mN/m'])

toc

function dydt=f(~,y,omegatest)
    dydt=zeros(size(y));
    dydt(1)=cos(y(3));
    dydt(2)=sin(y(3));
    dydt(3)=2-omegatest*y(2)-sin(y(3))/y(1);
end
```

### 7.1.2 Gaussian Bilateral Filtering Function

```
function [g,Nest] = GPA(f, sigmar, W, eps, flag)
% Kunal N. Chaudhury and Swapnil D. Dabhade
% Fast and Provably Accurate Bilateral Filtering, 2016
% IEEE Transactions on Image Processing, 25(6), pp. 2519-2528
% Gaussian Bilateral filter:
% [g,Ng] = GPA(f, sigmar, sigmas, eps, 'Gauss')
% f              : input image
% sigmar         : width of range Gaussian
```

```
% sigmas         : width of spatial Gaussian
% eps            : kernel approximation accuracy
% g              : output image
% Ng             : approximation order
%
% Box bilateral filter:
% [b,Nb] = GPA(f, sigmar, B, eps, 'box')
% f              : input image
% sigmar         : width of range Gaussian
% B              : width of box kernel
% eps            : kernel approximation accuracy
% g              : output image
% Nb             : approximation order

if strcmp(flag,'Gauss')
    L=round(3*W);
    Hs=fspecial('gaussian',2*L+1,W);
elseif  strcmp(flag,'box')
    L=W;
    Hs=fspecial('average',2*L+1);
else
    error('not enough arguments');
end
% Approximate order
T = 128; % dynamic range of image is [0,2T]
if  sigmar > 70
    N=10;
elseif sigmar < 5
    N=800;
else
    lam=(T/sigmar)^2;
    p = log(exp(1)*lam);
    q = -lam - log(eps);
    t = q*exp(-1)/lam;
    W = t - t^2 + 1.5*t^3 - (8/3)*t^4;
    N = min(max(q/W,10),300);
    if sigmar < 30
        for iter = 1:5
            N = N - (N*log(N)-p*N-q)/(log(N)+1-p);
        end
    end
end
Nest = ceil(N);
% Perform filtering
f=padarray(f,[L,L]);
H=(f-T)/sigmar;
F=exp(-0.5*H.^2);
G=ones(size(H));
P=zeros(size(H));
Q=zeros(size(H));
Fbar=imfilter(F,Hs);
for n = 1 : Nest
    Q=Q+G.*Fbar;
    F=H.*F/sqrt(n);
    Fbar=imfilter(F,Hs);
    P=P+G.*Fbar*sqrt(n);
    G=H.*G/sqrt(n);
```

```
end
g=T+sigmar*(P(L+1:end-L,L+1:end-L)./Q(L+1:end-L,L+1:end-L));
g(g<0)=0;
g(g>255)=255;
end
```

## 7.2 Matlab Code for Immiscible Bubble Growth Model

The numerical code written in Matlab for the immiscible bubble growth model outlined in Section 4.2 is presented here. There are four files needed to run the model. A main controlling file is used to define the model parameters such as the initial droplet size, initial bulk and droplet temperature, the superheat required to initiate boiling, the liquid properties, and the discretization schemes. This main controlling file calls on one of two function to determine the initial temperature profile; one function assumes the liquid-liquid interface temperature to be constant while the other treats it as variable. The last file is simply a graphing file used to visualize the results. From a user standpoint, the initial droplet and vapor core size, temperature conditions, liquid properties, and the temperature condition at the liquid-liquid interface during heating need to be specified in the main controlling file in accordance with the system being modeled. No adjustments need to be made in the functions which determine the initial temperature profile. In the graphing file, the user also specifies if they want to show and/or save the animation, and the temporal step size to use if showing the animation. All four files should be in the same directory when running the model.

### *7.2.1 Main Controlling File*

```
% Travis S. Emery
% Immiscible bubble growth model
% Concentric model to predict bubble growth in a drop of superheated
% liquid surrounded by an immiscible bulk liquid
tic
close all
clear
clc
```

```
% Temperature at liquid-liquid interface during initial heating period
LLTemp="constant"; % options are constant or variable
% ALL UNITS ADJUSTED TO mm AND ms
% Initial core and droplet size
R10=1E-2; % [mm]
R20=0.5; % [mm]
% Temperature conditions
Tinf=61+273.15; % Bulk fluid temperature [K]
T0=25+273.15;  % Initial drop temperature [K]
Ts=0; % Supheat required to initiate bubble growth [K]
% Boiling time domain
dt=0.1; % temporal resolution [ms]
tf=500; % final time [ms]
tspan=linspace(0,tf,tf/dt+1); % time domain

% FLUID 1 properties - adjusted for units in mm and ms
% FC-72
Tsat1=56+273.15; % Saturation Temperature [K]
rhov1=13E-9; % vapor density [kg/mm^3]
rhol1=1594E-9; % liquid density [kg/mm^3]
k1=0.054E-6; % liquid thermal conductivity [kg mm/ms^3 K]
Cp1=1101; % liquid specific heat [mm^2/ms^2 K]
alpha1=k1/(rhol1*Cp1); % liquid thermal diffusivity [mm^2/ms]
hfg=88000; % latent heat of vaporization
% FLUID 2 properties - adjusted for r in mm and time in ms
% Water
rhol2=980E-9; % liquid density [kg/mm^3]
k2=0.591E-6; % liquid thermal conductivity [kg mm/ms^3 K]
Cp2=4180; % liquid specific heat [mm^2/ms^2 K]
alpha2=k2/(rhol2*Cp2); % liquid thermal diffusivity [mm^2/ms]

% Dimensionless model parameters
R1bar0=R10/R20; % vapor core radius
R2bar0=1; % droplet radius
dn=0.01; % eta resoution
nf=20; % eta at "infinity"
n=linspace(0,nf,nf/dn+1); % eta domain
tauspan=tspan*alpha1/R20^2; % tau domain
% Dimensionless parameters from fluid properties
zeta=k2/k1;
gamma=alpha2/alpha1;
epsilon=1-rhov1/rhol1;
epsilonbar=1-rhol2/rhol1;
Ja=rhol1*Cp1*(Tinf-Tsat1)/(rhov1*hfg);

% Get initial temperature profile and time taken until boiling begins
if strcmpi(LLTemp,"constant")
    [Tbarinit,heattau]=ConstLLTDimensionlessIntialTempFun(n,T0,Tinf,...
        Tsat1,R1bar0,R2bar0,Ts);
elseif strcmpi(LLTemp,"variable")
    [Tbarinit,heattau]=VaryLLTDimensionlessIntialTempFun(n,T0,Tinf,...
        Tsat1,gamma,R1bar0,R2bar0,Ts);
end
heatt=heattau*R20^2/alpha1;
rinit=n*(R20-R10)+R10;
Tinit=Tbarinit*(Tinf-Tsat1)+Tsat1;
```

```
% Split into two domains, one for each liquid
n1=linspace(0,1,1/dn+1);
n2=linspace(1,nf,(nf-1)/dn+1);
Tbar10=Tbarinit(1:length(n1));
Tbar20=Tbarinit(length(n1):end);
% Solve system of ODEs
y0=[R1bar0;R2bar0;Tbar10;Tbar20];
options=odeset('Events',@(tautest,y) eventFunc(tautest,y,R20));
[tau,y]=ode15s(@(tautest,y) fun(tautest,y,n1,n2,dn,zeta,gamma,...
    epsilon,Ja),tauspan,y0,options);
% Extract results
R1bar=y(:,1); % L-V interface location
R2bar=y(:,2); % L-L interface location
Tbar1=y(:,3:length(n1)+2); % liquid 1 temperature profile
Tbar2=y(:,length(n1)+3:end); % liquid 2 temperature profile
Tbar=horzcat(Tbar1(:,1:end-1),Tbar2); % combined temperature profile
% Convert to dimensional coordinated
t=tau*R20^2/alpha1; % time
R1=R1bar*R20; % L-V interface location
R2=R2bar*R20; % L-L interface location
T=Tbar*(Tinf-Tsat1)+Tsat1; % combined temperature profile

toc

function f=fun(~,y,n1,n2,dn,zeta,gamma,epsilon,Ja)
    f=zeros(length(y),1);
    % Temporary variables for easier calculations
    R1bar=y(1);
    R2bar=y(2);
    Tbar1=y(3:length(n1)+2);
    Tbar2=y(length(n1)+3:end);
    r1bar=n1*(R2bar-R1bar)+R1bar;
    r2bar=n2*(R2bar-R1bar)+R1bar;
    % Initialize variables for spatial derivatives
    dTbar1dn=zeros(length(n1),1);
    d2Tbar1dn2=zeros(length(n1),1);
    dTbar2dn=zeros(length(n2),1);
    d2Tbar2dn2=zeros(length(n2),1);
    % Get n derivative in each domain
    for i=1:length(n1)
        if i==1
            dTbar1dn(i)=(-3/2*Tbar1(i)+2*Tbar1(i+1)-1/2*Tbar1(i+2))/dn;
            d2Tbar1dn2(i)=(2*Tbar1(i)-5*Tbar1(i+1)+4*Tbar1(i+2)-...
                Tbar1(i+3))/dn^2;
        elseif i==length(n1)
            dTbar1dn(i)=zeta*(-3/2*Tbar2(1)+2*Tbar2(2)-...
                1/2*Tbar2(3))/dn;
            d2Tbar1dn2(i)=(2*Tbar1(i)-5*Tbar1(i-1)+4*Tbar1(i-2)-...
                Tbar1(i-3))/dn^2;
        else
            dTbar1dn(i)=(1/2*Tbar1(i+1)-1/2*Tbar1(i-1))/dn;
            d2Tbar1dn2(i)=(Tbar1(i-1)-2*Tbar1(i)+Tbar1(i+1))/dn^2;
        end
    end
    for i=1:length(n2)
        if i==1
            dTbar2dn(i)=(-3/2*Tbar2(i)+2*Tbar2(i+1)-1/2*Tbar2(i+2))/dn;
```

```
            d2Tbar2dn2(i)=(2*Tbar2(i)-5*Tbar2(i+1)+4*Tbar2(i+2)-...
                Tbar2(i+3))/dn^2;
        elseif i==length(n2)
            dTbar2dn(i)=(3/2*Tbar2(i)-2*Tbar2(i-1)+1/2*Tbar2(i-2))/dn;
            d2Tbar2dn2(i)=(2*Tbar2(i)-5*Tbar2(i-1)+4*Tbar2(i-2)-...
                Tbar2(i-3))/dn^2;
        else
            dTbar2dn(i)=(1/2*Tbar2(i+1)-1/2*Tbar2(i-1))/dn;
            d2Tbar2dn2(i)=(Tbar2(i-1)-2*Tbar2(i)+Tbar2(i+1))/dn^2;
        end
    end
    for i=1:length(f)
        if i==1 % dR1dt
            f(i)=Ja/(R2bar-R1bar)*dTbar1dn(1);
        elseif i==2 % dR2dt
            f(i)=epsilon*R1bar^2/R2bar^2*f(1);
        elseif i==3 % dTbar1dt at n=0
            f(i)=0;
        elseif i>3&&i<=length(n1)+2 % dTbar1dt
            f(i)=(dTbar1dn(i-2)*f(1)*((r1bar(i-2)^3*(R2bar^2-epsilon...
                *R1bar^2)-r1bar(i-2)^2*(R2bar^3-epsilon*R1bar^3))/...
                (R2bar^2*(R2bar-R1bar))+epsilon*R1bar^2)-2*...
                r1bar(i-2)*dTbar1dn(i-2)-r1bar(i-2)^2/(R2bar-R1bar)*...
                d2Tbar1dn2(i-2))/(-(R2bar-R1bar)*r1bar(i-2)^2);
        elseif i==length(n1)+3 % dTbar2dt at n=1
            f(i)=f(i-1);
        elseif i>length(n1)+3&&i<length(f) % dTbar2dt
            f(i)=(dTbar2dn(i-length(n1)-2)*f(1)*((r2bar(i-length(n1)...
                -2)^3*(R2bar^2-epsilon*R1bar^2)-r2bar(i-length(n1)...
                -2)^2*(R2bar^3-epsilon*R1bar^3))/(R2bar^2*(R2bar-...
                R1bar))+epsilon*R1bar^2)-gamma*2*r2bar(i-length(n1)...
                -2)*dTbar2dn(i-length(n1)-2)-gamma*r2bar(i-...
                length(n1)-2)^2/(R2bar-R1bar)*d2Tbar2dn2(i-...
                length(n1)-2))/(-(R2bar-R1bar)*r2bar(i-length(n1)...
                -2)^2);
        elseif i==length(f) % dTbar2dt at n=inf
            f(i)=0;
        end
    end
end

function [value,isterminal,direction] = eventFunc(~,y,R20)
    value=R20*(y(2)-y(1))-0.001;
    isterminal=1;
    direction=0;
end
```

### *7.2.2 Graphing File*

```
% Travis S. Emery
% Graphing for immiscible bubble growth model
close all
Animation="off"; % turn animation off or on
AnimationStep=20; % animation step size
save="no"; % save movie; options are yes or no
```

```
% Initial Temperature Profile
figure(1)
set(gcf,'color','w')
subplot(1,2,1)
plot(rinit,Tinit-273.15)
title('Initial Temperature Profile')
xlabel('Radial Distance, r (mm)')
ylabel('Temperature (^oC)')
axis([0 2*(R20-R10)+R10 Tsat1-5-273.15 Tinf+10-273.15])
subplot(1,2,2)
plot(n,Tbarinit)
title('Initial Dimensionless Temperature Profile')
str='$$\eta=\frac{r-R_1}{R_2-R_1}$';
xlabel(str,'interpreter','latex','fontsize',12);
str='$$\overline{T}=\frac{T-T_{sat,1}}{T_\infty-T_{sat,1}}$';
ylabel(str,'interpreter','latex','fontsize',12);
axis([0 2 0 1])

% Bubble Growth
figure(2)
set(gcf,'color','w')
subplot(1,2,1)
plot(tau,R1bar)
hold on
plot(tau,R2bar)
xlabel('\tau')
ylabel('Dimensionless Interface Location');
h=legend('$$\overline{R_1}$$','$$\overline{R_2}$$');
set(h,'Interpreter','latex','fontsize',12,'location','northwest')
subplot(1,2,2)
plot(t,R1)
hold on
plot(t,R2)
xlabel('Time (ms)')
ylabel('Interface Location (mm)')
legend('R_1','R_2','location','northwest')

% Temperature Profile Evolution
figure(3)
set(gcf,'color','w')
subplot(1,2,1)
plot(n,Tbar(round(0.2*length(tau)),:))
hold on
plot(n,Tbar(round(0.4*length(tau)),:))
plot(n,Tbar(round(0.6*length(tau)),:))
plot(n,Tbar(round(0.8*length(tau)),:))
plot(n,Tbar(end,:))
xlabel('\eta')
str='$$\overline{T}=\frac{T-T_{sat,1}}{T_\infty-T_{sat,1}}$';
ylabel(str,'interpreter','latex','fontsize',13);
legend(['\tau=' num2str(tau(round(0.2*length(tau))))],['\tau='...
    num2str(tau(round(0.4*length(tau))))],['\tau=' num2str(tau(...
    round(0.6*length(tau))))],['\tau=' num2str(tau(round(0.8*...
    length(tau))))],['\tau=' num2str(tau(end))])
axis([0 2 0 1])
subplot(1,2,2)
plot(n,T(round(0.2*length(t)),:)-273.15)
```

```
hold on
plot(n,T(round(0.4*length(t)),:)-273.15)
plot(n,T(round(0.6*length(t)),:)-273.15)
plot(n,T(round(0.8*length(t)),:)-273.15)
plot(n,T(end,:)-273.15)
xlabel('\eta')
ylabel('Temperature (^oC)');
legend(['t=' num2str(t(round(0.2*length(t)))) ' ms'],['t='...
    num2str(t(round(0.4*length(t)))) ' ms'],['t=' num2str(...
    t(round(0.6*length(t)))) ' ms'],['t=' num2str(t(round(0.8*...
    length(t)))) ' ms'],['t=' num2str(t(end)) ' ms'])
axis([0 2 min(min(T))-5-273.15 max(max(T))+5-273.15])

% Animation
if strcmpi(Animation,"on")
fig=figure(4);
set(gcf,'color','w', 'Position', [500, 500, 1000, 500]);
% Dimensionless Temperature Profile
subplot(1,2,1)
title('Dimensionless Temperature Profile')
str='$$\eta=\frac{r-R_1}{R_2-R_1}$';
xlabel(str,'interpreter','latex','fontsize',18);
str='$$\overline{T}=\frac{T-T_{sat,1}}{T_\infty-T_{sat,1}}$';
ylabel(str,'interpreter','latex','fontsize',18);
axis([0 2 0 1])
axis square
box on
an1=animatedline('linewidth',2);
set(gca,'fontsize',18,'linewidth',2)
% Bubble growth
subplot(1,2,2)
title('Bubble Growth')
xlabel('Radial Distance, r (mm)')
ylabel('Radial Distance, r (mm)')
axis([-ceil(R2(end)) ceil(R2(end)) -ceil(R2(end)) ceil(R2(end))])
axis square
box on
an2a=animatedline('linewidth',2);
an2b=animatedline('linewidth',2);
set(gca,'TickDir','out','fontsize',18,'linewidth',2)

xsq=[-ceil(R2(end)) ceil(R2(end)) ceil(R2(end)) -ceil(R2(end))];
ysq=[-ceil(R2(end)) -ceil(R2(end)) ceil(R2(end)) ceil(R2(end))];
ang=0:0.01:2*pi;
framecount=1;
myMovie=struct('cdata', cell(1,ceil(length(tau)/AnimationStep)),...
    'colormap', cell(1,ceil(length(tau)/AnimationStep)));
for i=1:AnimationStep:length(tau)
    clearpoints(an1)
    addpoints(an1,n,Tbar(i,:))
    clearpoints(an2a)
    clearpoints(an2b)
    x1=R1(i)*cos(ang);
    y1=R1(i)*sin(ang);
    x2=R2(i)*cos(ang);
    y2=R2(i)*sin(ang);
    addpoints(an2a,x1,y1)
```

```
    addpoints(an2b,x2,y2)
    hold on
    fill(xsq,ysq,[197 224 180]./255,'linewidth',2)
    fill(x2,y2,[68 114 196]./255,'linewidth',2)
    fill(x1,y1,[255 230 153]./255,'linewidth',2)
    drawnow
    if strcmpi(save, 'yes')
        myMovie(framecount)=getframe(fig);
        framecount=framecount+1;
    end
end

if strcmpi(save, 'yes')
    % Get the name of the file that the user wants to save
    [baseFileName,folder]=uiputfile('*.avi','Specify a file');
    if baseFileName==0 % User clicked the Cancel button
        return;
    end
    fullFileName=fullfile(folder,baseFileName);
    % Create a video writer object with that file name.
    writerObj=VideoWriter(fullFileName,'Uncompressed AVI');
    open(writerObj);
    % Write out all the frames.
    numberOfFrames=length(myMovie);
    for frameNumber=1:numberOfFrames
       writeVideo(writerObj,myMovie(frameNumber));
    end
    close(writerObj);
end

end
```

### 7.2.3 Initial Temperature Function for Constant Interface Temperature

```
function [Tbarinit,taufend]=ConstLLTDimensionlessIntialTempFun(n,T0,...
    Tinf,Tsat1,R1bar0,R2bar0,Ts)
    % Travis S. Emery
    % Determines initial temperature profile assuming a constant
    % liquid-liquid interface temperature
    % Solves for temperture profile in droplet with no vapor core, then
    % interprets solution to initial geometry specified by the problem
    dtau=10^-3; % tau step size
    tauf=3; % Initial guess for tau until boiling begins
    tauspan=linspace(0,tauf,tauf/dtau+1);
    ndrop=linspace(0,1,1001);
    pdeFunc=@(n,tau,Tbar,DTbarDn) pde(n,tau,Tbar,DTbarDn,0,1);
    icFunc=@(n) pdeic(n);
    bcFunc=@(nl,Tbarl,nr,Tbarr,tau) pdebc(nl,Tbarl,nr,Tbarr,tau);
    m=0;
    options=odeset('Events',@(m,tau,n,Tbar) eventFunc(m,tau,n,Tbar,...
        Tsat1,T0,Tinf,Ts));

[sol,~,~,te,~]=pdepe(m,pdeFunc,icFunc,bcFunc,ndrop,tauspan,options);
    taufend=te;
    ntemp=linspace(R1bar0,R2bar0,length(n(n<=1)));
    Ttemp=interp1(ndrop,sol(end,:),ntemp);
```

```
    Tbarinit=ones(size(n));
    Tbarinit(1:length(n(n<=1)))=((Ttemp*(Tinf-T0)+T0)-Tsat1)/...
        (Tinf-Tsat1);
    Tbarinit(1)=0;
    Tbarinit=Tbarinit.';
    function [c,f,s]=pde(n,~,~,DTbarDn,R1bar,R2bar)
        rbar=n*(R2bar-R1bar)+R1bar;
        c=rbar^2*(R2bar-R1bar);
        f=rbar^2/(R2bar-R1bar)*DTbarDn;
        s=0;
    end
    function Tbar0=pdeic(n)
        if n<1
            Tbar0=0 ;
        else
            Tbar0=1 ;
        end
    end
    function [pl,ql,pr,qr]=pdebc(~,~,~,Tbarr,~)
        pl=0;
        ql=1;
        pr=Tbarr-1;
        qr=0;
    end
    function [value,isterminal,direction]=eventFunc(~,~,~,Tbar,...
            Tsat1,T0,Tinf,Ts)
        value=Tbar(1)-(Tsat1+Ts-T0)/(Tinf-T0);
        isterminal=1;
        direction=0;
    end
end
```

### *7.2.4 Initial Temperature Function for Variable Interface Temperature*

```
function [Tbarinit,taufend] =
VaryLLTDimensionlessIntialTempFun(n,T0,...
    Tinf,Tsat1,gamma,R1bar0,R2bar0,Ts)
    % Travis S. Emery
    % Determines initial temperature profile assuming a variable
    % liquid-liquid interface temperature
    % Solves for temperture profile in droplet with no vapor core, then
    dtau=10^-3; % tau step size
    tauf=3; % Initial guess for tau until boiling begins
    tau=linspace(0,tauf,tauf/dtau+1);
    pdeFunc=@(n,tau,Tbar,DTbarDn) pde(n,tau,Tbar,DTbarDn,gamma,0,1);
    icFunc=@(n) pdeic(n);
    bcFunc=@(nl,Tbarl,nr,Tbarr,tau) pdebc(nl,Tbarl,nr,Tbarr,tau);
    m=0;
    options=odeset('Events',@(m,tau,n,Tbar) eventFunc(m,tau,n,Tbar,...
        Tsat1,T0,Tinf,Ts));
    [sol,~,~,te,~]=pdepe(m,pdeFunc,icFunc,bcFunc,n,tau,options);
    taufend=te;
    ntemp=linspace(R1bar0,R2bar0,length(n(n<=1)));
    Ttemp=interp1(n,sol(end,:),ntemp);
    Tbarinit=sol(end,:);
    Tbarinit(1:length(n(n<=1)))=Ttemp;
```

```
    Tbarinit=(((Tbarinit*(Tinf-T0)+T0)-Tsat1)/(Tinf-Tsat1)).';
    Tbarinit(1)=0;
    function [c,f,s]=pde(n,~,~,DTbarDn,gamma,R1bar,R2bar)
        rbar=n*(R2bar-R1bar)+R1bar;
        c=rbar^2*(R2bar-R1bar);
        if n<1
            f=rbar^2/(R2bar-R1bar)*DTbarDn;
        else
            f=rbar^2/(R2bar-R1bar)*DTbarDn*gamma;
        end
        s=0;
    end
    function Tbar0=pdeic(n)
        if n<1
            Tbar0=0 ;
        else
            Tbar0=1 ;
        end
    end
    function [pl,ql,pr,qr]=pdebc(~,~,~,Tbarr,~)
        pl=0;
        ql=1;
        pr=Tbarr-1;
        qr=0;
    end
    function [value,isterminal,direction]=eventFunc(~,~,~,Tbar,...
            Tsat1,T0,Tinf,Ts)
        value=Tbar(1)-(Tsat1+Ts-T0)/(Tinf-T0);
        isterminal=1;
        direction=0;
    end
end
```

## 7.3 Matlab Code for Bubble Collision Models

The numerical code written in Matlab for the bubble collision models outlined in Section 4.4 is presented in this section. There are ten separate files that make up the models for bubble collisions at a solid-liquid (SL), gas-liquid (GL), liquid-liquid (LL), solid-liquid-liquid (SLL), or gas-liquid-liquid (GLL) interface. A main controlling file is used to define the system to be modeled, including information such as the type of interface type, whether the initial velocity of the bubble is the associated terminal velocity or zero, the bubble size and initial distance from the interface, the initial top film thickness if applicable, the liquid properties, and the domain sizing and discretization. For single-liquid systems, the properties defined for the bottom liquid are used in the model. Once a simulation is run, a graphing file is used to generate plots and animations of the results. In this, static plots are shown at nine different times spaced evenly between user specified values. The user also specifies if they want to show and/or save the animation, and the temporal step size to use if showing the animation. From a user standpoint, only the main controlling file and the graphing file need to be used to define the desired problem, run the model, and visualize the results. The other eight files are functions used by the main controlling function to solve the defined model. These functions need only be in the same directory as the main and graphing files. One function is used for each of the five interface types, one is used to determine the drag coefficient based on an input Reynolds and Weber number using the theory compile by Loth [84], one is used to get the spatial derivates using a second order finite difference scheme, and the last is used to define the coefficients used for integration by Simpson's rule. Since Simpson's rule can only be used for an odd number of discrete point (counted starting from n=1), the standard rule is combined with Simpson's 3/8 formula if there is an even number of discrete points to integrate over.

### *7.3.1 Main Controlling File*

```
% Travis S. Emery
% Bubble collision modeling
% This is the main controlling function in which the system parameters
% are defined to then be solved by the associated model
tic
close all
clear
clc
% Model Parameters
Itype="LL"; % options are SL, GL, LL, SLL, or GLL
V0type="terminal"; % options are terminal or nonterminal
Cm=0.46; % set Cm value for LL, SLL, and GLL models; not for SL or GL
% ALL UNITS IN mm AND ms
R=0.65; % bubble radius [mm]
H10=0.5; % initial top film thickness [mm]
H200=10; % initial distance from bubble top to interface [mm]
% Constants
g=9.81E-3; % gravitational acceleration [mm/ms^2]
% Liquid properties
rhob=1000E-9; % bottom liquid density [kg/mm^3]
```

```
mub=1E-9; % bottom liquid viscosity [kg/(mm*ms)]
sigmab=72E-9; % bottom liquid surface tension [kg/ms^2]
rhot=918E-9; % top liquid density [kg/mm^3]
mut=4.59E-9; % top liquid viscosity [kg/(mm*ms)]
sigmat=19.7E-9; % top liquid surface tension [kg/ms^2]
sigmai=51E-9; % interfacial tension [kg/ms^2]
sigmabar=1/(1/sigmai+1/sigmab); [kg/ms^2]
sigmaprime=1/(1/sigmai+1/sigmat); [kg/ms^2]
% Discretization
dr=0.01; % spatial resolution [mm]
rm=round(1.2*R/dr)*dr; % outer boundary location [mm]
r=linspace(0,rm,rm/dr+1).'; % spatial domain
dt=0.1; % time resolution [ms]
tf=100; % final time [ms]
tspan=linspace(0,tf,tf/dt+1).'; % time domain
maxstep=0.01;  % maximum time step for solver [ms]
% Solve the system described by the above parameters
if strcmpi(Itype,"SL")
    [t,X,V,h,p,zb,Fb,Fd,Fa,Ff]=SL(tspan,maxstep,r,dr,R,rhob,mub,...
        sigmab,g,H200,V0type);
elseif strcmpi(Itype,"GL")
    [t,X,V,h,p,zS,zb,Fb,Fd,Fa,Ff]=GL(tspan,maxstep,r,dr,R,rhob,...
        mub,sigmab,g,H200,V0type);
elseif strcmpi(Itype,"LL")
    [t,X,V,h,p,tauv,zI,zb,Fb,Fd,Fa,Ff]=LL(tspan,maxstep,r,dr,R,...
        rhob,mub,sigmab,rhot,mut,sigmai,sigmabar,g,H200,V0type,Cm);
elseif strcmpi(Itype,"SLL")
    [t,X,V,h1,h2,p1,p2,tauv,zI,zb,Fb,Fd,Fa,Ff]=SLL(tspan,maxstep...
        ,r,dr,R,rhob,mub,sigmab,rhot,mut,sigmai,sigmabar,g,H10...
        ,H200,V0type,Cm);
elseif strcmpi(Itype,"GLL")
    [t,X,V,h1,h2,p1,p2,tauv,zI,zb,zS,Fb,Fd,Fa,Ff]=GLL(tspan...
        ,maxstep,r,dr,R,rhob,mub,sigmab,rhot,mut,sigmat,sigmai...
        ,sigmabar,sigmaprime,g,H10,H200,V0type,Cm);
end
% Convert solution to desired units and combine
% [ms] [mm] [cm/s] [uN]
Sol=[t X V*100 Fb*-1E9 Fd*-1E9 Fa*-1E9 Ff*-1E9];
toc
```

### 7.3.2 Graphing File

```
% Travis S. Emery
% Graphing for bubble collision modeling
close all
Animation="on"; % turn animation off or on
AnimationStep=2; % animation step size
save="yes"; % save movie; options are yes or no

% Plot thickness, pressure, and interface profiles at 9 times
% spaced evenly between user-specified values t1 and t2
t1=31;
t2=35;
tindex=linspace(t1,t2,9);
index=zeros(size(tindex));
for i=1:length(tindex)
    index(i)=find(t>tindex(i),1)-1;
```

```
end

% Bubble trajectory
figure(1)
yyaxis left
plot(t,100*V)
xlabel('Time (ms)')
ylabel('Velocity (cm/s)')
yyaxis right
plot(t,X)
ylabel('Distance (mm)')
title('Bubble Trajectory Profile')
set(gca,'Ydir','reverse')
set(gcf,'color','w')

% Force Evolution
figure(2)
plot(t,-1E9*Ff)
hold on
plot(t,-1E9*Fa)
plot(t,-1E9*Fb)
plot(t,-1E9*Fd)
legend('Film Force','Added Mass','Buoyancy','Drag','Location',...
    'Northeast')
xlabel('Time (ms)')
ylabel('Force (\muN)')
title('Force Profile')
set(gcf,'color','w')

% Make full profiles
totalr=horzcat(-fliplr(r(2:end).'),r.');
totalzb=horzcat(fliplr(zb(:,2:end)),zb);
if strcmp(Itype,'SL') || strcmp(Itype,'GL') || strcmp(Itype,'LL')
    totalh=horzcat(fliplr(h(:,2:end)),h);
    totalp=horzcat(fliplr(1e9*p(:,2:end)),1e9*p);
    if strcmp(Itype,'GL')
        totalz=horzcat(fliplr(zS(:,2:end)),zS);
    elseif strcmp(Itype,'LL')
        totalz=horzcat(fliplr(zI(:,2:end)),zI);
    end
else
    totalh1=horzcat(fliplr(h1(:,2:end)),h1);
    totalh2=horzcat(fliplr(h2(:,2:end)),h2);
    totalz=horzcat(fliplr(zI(:,2:end)),zI);
    totalp1=horzcat(fliplr(1e9*p1(:,2:end)),1e9*p1);
    totalp2=horzcat(fliplr(1e9*p2(:,2:end)),1e9*p2);
    if strcmp(Itype,'GLL')
        totalzS=horzcat(fliplr(zS(:,2:end)),zS);
    end
end

% Film Thickness Profiles
figure(3)
if strcmp(Itype,'SL') || strcmp(Itype,'GL') || strcmp(Itype,'LL')
    plot(totalr,totalh(index(1),:),'k')
    hold on
    plot(totalr,totalh(index(2),:),'m')
```

```
    plot(totalr,totalh(index(3),:),'g')
    plot(totalr,totalh(index(4),:),'r')
    plot(totalr,totalh(index(5),:),'b')
    plot(totalr,totalh(index(6),:),'c')
    plot(totalr,totalh(index(7),:),'y')
    plot(totalr,totalh(index(8),:),'m')
    plot(totalr,totalh(index(9),:),'k')
    legend(['t=' num2str(tindex(1)) ' ms'],...
        ['t=' num2str(tindex(2)) ' ms'],['t=' num2str(tindex(3))...
        ' ms'],['t=' num2str(tindex(4)) ' ms'],['t=' ...
        num2str(tindex(5)) ' ms'],['t=' num2str(tindex(6)) ' ms']...
        ,['t=' num2str(tindex(7)) ' ms'],['t=' num2str(tindex(8))...
        ' ms'],['t=' num2str(tindex(9)) ' ms'])
    xlabel('Radial Distance, r (mm)')
    ylabel('Film Thickness, h (mm)')
    title('Film Thickness Profile')
    axis([-ceil(r(end)*10)/10 ceil(r(end)*10)/10 0 0.05])
    set(gcf,'color','w')
else
    subplot(1,2,1)
    plot(totalr,totalh1(index(1),:),'k')
    hold on
    plot(totalr,totalh1(index(2),:),'m')
    plot(totalr,totalh1(index(3),:),'g')
    plot(totalr,totalh1(index(4),:),'r')
    plot(totalr,totalh1(index(5),:),'b')
    plot(totalr,totalh1(index(6),:),'c')
    plot(totalr,totalh1(index(7),:),'y')
    plot(totalr,totalh1(index(8),:),'m')
    plot(totalr,totalh1(index(9),:),'k')
    legend(['t=' num2str(tindex(1)) ' ms'],['t=' num2str(tindex(2))...
        ' ms'],['t=' num2str(tindex(3)) ' ms'],['t=' ...
        num2str(tindex(4)) ' ms'],['t=' num2str(tindex(5)) ' ms'],...
        ['t=' num2str(tindex(6)) ' ms'],['t=' num2str(tindex(7)) ...
        ' ms'],['t=' num2str(tindex(8)) ' ms'],['t=' ...
        num2str(tindex(9)) ' ms'])
    xlabel('Radial Distance, r (mm)')
    ylabel('Top Film Thickness, h_1 (mm)')
    title('Top Layer Film Thickness Profile')
    axis([-ceil(r(end)*10)/10 ceil(r(end)*10)/10 0 0.1])
    set(gcf,'color','w')
    subplot(1,2,2)
    plot(totalr,totalh2(index(1),:),'k')
    hold on
    plot(totalr,totalh2(index(2),:),'m')
    plot(totalr,totalh2(index(3),:),'g')
    plot(totalr,totalh2(index(4),:),'r')
    plot(totalr,totalh2(index(5),:),'b')
    plot(totalr,totalh2(index(6),:),'c')
    plot(totalr,totalh2(index(7),:),'y')
    plot(totalr,totalh2(index(8),:),'m')
    plot(totalr,totalh2(index(9),:),'k')
    legend(['t=' num2str(tindex(1)) ' ms'],['t=' num2str(tindex(2))...
        ' ms'],['t=' num2str(tindex(3)) ' ms'],['t=' ...
        num2str(tindex(4)) ' ms'],['t=' num2str(tindex(5)) ' ms'],...
        ['t=' num2str(tindex(6)) ' ms'],['t=' num2str(tindex(7)) ...
        ' ms'],['t=' num2str(tindex(8)) ' ms'],['t=' ...
```

```
        num2str(tindex(9)) ' ms'])
    xlabel('Radial Distance, r (mm)')
    ylabel('Bottom Film Thickness, h_2 (Pa)')
    title('Bottom Layer Film Thickness Profile')
    axis([-ceil(r(end)*10)/10 ceil(r(end)*10)/10 0 0.1])
    set(gcf,'color','w')
end

% Pressure Profiles
figure(4)
if strcmp(Itype,'SL') || strcmp(Itype,'GL') || strcmp(Itype,'LL')
    plot(totalr,totalp(index(1),:),'k')
    hold on
    plot(totalr,totalp(index(2),:),'m')
    plot(totalr,totalp(index(3),:),'g')
    plot(totalr,totalp(index(4),:),'r')
    plot(totalr,totalp(index(5),:),'b')
    plot(totalr,totalp(index(6),:),'c')
    plot(totalr,totalp(index(7),:),'y')
    plot(totalr,totalp(index(8),:),'m')
    plot(totalr,totalp(index(9),:),'k')
    legend(['t=' num2str(tindex(1)) ' ms'],['t=' num2str(tindex(2))...
        ' ms'],['t=' num2str(tindex(3)) ' ms'],['t=' ...
        num2str(tindex(4)) ' ms'],['t=' num2str(tindex(5)) ' ms'],...
        ['t=' num2str(tindex(6)) ' ms'],['t=' num2str(tindex(7)) ...
        ' ms'],['t=' num2str(tindex(8)) ' ms'],['t=' ...
        num2str(tindex(9)) ' ms'])
    axis([-ceil(r(end)*10)/10 ceil(r(end)*10)/10 -ceil(...
        max(max(totalp))/100)*100 ceil(max(max(totalp))/100)*100])
    xlabel('Radial Distance, r (mm)')
    ylabel('Film Pressure, p (Pa)')
    title('Film Pressure Profile')
    set(gcf,'color','w')
else
    subplot(1,2,1)
    plot(totalr,totalp1(index(1),:),'k')
    hold on
    plot(totalr,totalp1(index(2),:),'m')
    plot(totalr,totalp1(index(3),:),'g')
    plot(totalr,totalp1(index(4),:),'r')
    plot(totalr,totalp1(index(5),:),'b')
    plot(totalr,totalp1(index(6),:),'c')
    plot(totalr,totalp1(index(7),:),'y')
    plot(totalr,totalp1(index(8),:),'m')
    plot(totalr,totalp1(index(9),:),'k')
    legend(['t=' num2str(tindex(1)) ' ms'],['t=' num2str(tindex(2))...
        ' ms'],['t=' num2str(tindex(3)) ' ms'],['t=' ...
        num2str(tindex(4)) ' ms'],['t=' num2str(tindex(5)) ' ms'],...
        ['t=' num2str(tindex(6)) ' ms'],['t=' num2str(tindex(7)) ...
        ' ms'],['t=' num2str(tindex(8)) ' ms'],['t=' ...
        num2str(tindex(9)) ' ms'])
    axis([-ceil(r(end)*10)/10 ceil(r(end)*10)/10 -ceil(...
        max(max(totalp1))/10)*10 ceil(max(max(totalp1))/10)*10])
    xlabel('Radial Distance, r (mm)')
    ylabel('Top Film Pressure, p_1 (Pa)')
    title('Top Layer Pressure Profile')
    set(gcf,'color','w')
```

```
    subplot(1,2,2)
    plot(totalr,totalp2(index(1),:),'k')
    hold on
    plot(totalr,totalp2(index(2),:),'m')
    plot(totalr,totalp2(index(3),:),'g')
    plot(totalr,totalp2(index(4),:),'r')
    plot(totalr,totalp2(index(5),:),'b')
    plot(totalr,totalp2(index(6),:),'c')
    plot(totalr,totalp2(index(7),:),'y')
    plot(totalr,totalp2(index(8),:),'m')
    plot(totalr,totalp2(index(9),:),'k')
    legend(['t=' num2str(tindex(1)) ' ms'],['t=' num2str(tindex(2))...
        ' ms'],['t=' num2str(tindex(3)) ' ms'],['t=' ...
        num2str(tindex(4)) ' ms'],['t=' num2str(tindex(5)) ' ms'],...
        ['t=' num2str(tindex(6)) ' ms'],['t=' num2str(tindex(7)) ...
        ' ms'],['t=' num2str(tindex(8)) ' ms'],['t=' ...
        num2str(tindex(9)) ' ms'])
    axis([-ceil(r(end)*10)/10 ceil(r(end)*10)/10 -ceil(...
        max(max(totalp2))/100)*100 ceil(max(max(totalp2))/100)*100])
    xlabel('Radial Distance, r (mm)')
    ylabel('Bottom Film Pressure, p_2 (Pa)')
    title('Bottom Layer Pressure Profile')
    set(gcf,'color','w')
end

% Animation
if strcmpi(Animation,"on")
fig=figure(5);
set(gcf, 'Position', [500, 0, 1250, 1100],'color','w')
% Trajectory
subplot(2,2,1)
yyaxis left
xlabel('Time (ms)')
ylabel('Velocity (cm/s)')
an1a = animatedline('Color','b','linewidth',2);
axis([0 t(end) floor(min(V*100)/10)*10 ceil(max(V*100)/10)*10])
yyaxis right
axis([0 t(end) -1 5])
ylabel('Distance (mm)')
an1b = animatedline('Color','r','linewidth',2);
set(gca,'Ydir','reverse','fontsize',18,'linewidth',2)
xticks([0 25 50 75 100 125 150])
box on
% Pressure
if strcmp(Itype,'GL') || strcmp(Itype,'SL') || strcmp(Itype,'LL')
    subplot(2,2,3)
    axis([totalr(1) totalr(end) -ceil(max(max(totalp))/100)*100 ...
        ceil(max(max(totalp))/100)*100])
    xlabel('Radial Distance, r (mm)')
    ylabel('Film Pressure, p (Pa)')
    an2 = animatedline('linewidth',2);
    set(gca,'fontsize',18,'linewidth',2)
    box on
else
    subplot(4,2,5)
    axis([totalr(1) totalr(end) -ceil(max(max(totalp1))/10)*10 ...
        ceil(max(max(totalp1))/10)*10])
```

```
    ylabel({'Top Film';'Pressure, p_1 (Pa)'})
    an2a = animatedline('linewidth',2);
    set(gca,'fontsize',18,'linewidth',2)
    box on
    subplot(4,2,7)
    axis([totalr(1) totalr(end) -ceil(max(max(totalp2))/100)*100 ...
        ceil(max(max(totalp2))/100)*100])
    xlabel('Radial Distance, r (mm)')
    ylabel({'Bottom Film';'Pressure, p_2 (Pa)'})
    an2b = animatedline('linewidth',2);
    set(gca,'fontsize',18,'linewidth',2)
    box on
end
% Film Thickness
if strcmp(Itype,'SL') || strcmp(Itype,'GL') || strcmp(Itype,'LL')
    subplot(2,2,4)
    set(gca, 'YScale', 'log')
    xlabel('Radial Distance, r (mm)')
    ylabel('Film Thickness, h (mm)')
    axis([totalr(1) totalr(end) 0.0001 20])
    an4 = animatedline('linewidth',2);
    box on
    set(gca,'fontsize',18,'linewidth',2)
else
    subplot(4,2,6)
    ylabel({'Top Film';'Thickness, h_1 (mm)'})
    axis([totalr(1) totalr(end) 0 ceil(H10)+0.5])
    an4a = animatedline('linewidth',2);
    set(gca,'fontsize',18,'linewidth',2)
    box on
    subplot(4,2,8)
    set(gca, 'YScale', 'log')
    xlabel('Radial Distance, r (mm)')
    ylabel({'Bottom Film';'Thickness, h_2 (mm)'})
    axis([totalr(1) totalr(end) 0.0001 20])
    an4b = animatedline('linewidth',2);
    set(gca,'fontsize',18,'linewidth',2)
    yticks([10^-4 10^-2 10^0])
    box on
end
% Interface Profile
subplot(2,2,2)
axis([totalr(1) totalr(end) -5 1])
if strcmp(Itype,'SL')
    an3 = animatedline('linewidth',2);
    set(gca,'fontsize',18,'linewidth',2)
    box on
elseif strcmp(Itype,'GL') || strcmp(Itype,'LL') || strcmp(Itype,'SLL')
    an3a = animatedline('linewidth',2);
    an3b = animatedline('linewidth',2);
    set(gca,'fontsize',18,'linewidth',2)
    box on
else
    an3a = animatedline('linewidth',2);
    an3b = animatedline('linewidth',2);
    an3c = animatedline('linewidth',2);
    set(gca,'fontsize',18,'linewidth',2)
```

```
    box on
end
set(gca, 'YScale', 'linear')
xlabel('Radial Distance, r (mm)')
ylabel('Interface Profile (mm)')

framecount=1;
myMovie=struct('cdata', cell(1,ceil(length(t)/AnimationStep)),...
    'colormap', cell(1,ceil(length(t)/AnimationStep)));
for i=1:AnimationStep:length(t)
    % Trajectory
    addpoints(an1a,t(i),100*V(i));
    addpoints(an1b,t(i),X(i))
    % Pressure
    if strcmp(Itype,'GL') || strcmp(Itype,'SL') || strcmp(Itype,'LL')
        clearpoints(an2)
        addpoints(an2,totalr,totalp(i,:))
    else
        clearpoints(an2a)
        addpoints(an2a,totalr,totalp1(i,:))
        clearpoints(an2b)
        addpoints(an2b,totalr,totalp2(i,:))
    end
    % Film Thickness
    if strcmp(Itype,'GL') || strcmp(Itype,'LL') || strcmp(Itype,'SL')
        clearpoints(an4)
        addpoints(an4,totalr,totalh(i,:))
    else
        clearpoints(an4a)
        clearpoints(an4b)
        addpoints(an4a,totalr,totalh1(i,:))
        addpoints(an4b,totalr,totalh2(i,:))
    end
    % Interface Profile
    if strcmp(Itype,'SL')
        clearpoints(an3)
        addpoints(an3,totalr,totalzb(i,:))
        hold on
        bubble1=[totalr(1) totalr totalr(end) totalr(1)];
        bubble2=[-5 totalzb(i,:) -5 -5];
        fill(bubble1,bubble2,[255 230 153]./255,'linewidth',2)
        filmtop1=[totalr totalr(end) totalr(1) totalr(1)];
        filmtop2=[totalzb(i,:) 0 0 totalzb(i,1)];
        fill(filmtop1,filmtop2,[143 170 220]./255,'linewidth',2)
        fill([totalr(1) totalr(end) totalr(end) totalr(1)],...
            [0 0 1 1],[165 165 165]./255,'linewidth',2)
    elseif strcmp(Itype,'GL') || strcmp(Itype,'LL')
        clearpoints(an3a)
        clearpoints(an3b)
        addpoints(an3a,totalr,totalz(i,:))
        addpoints(an3b,totalr,totalzb(i,:))
        hold on
        bubble1=[totalr(1) totalr totalr(end) totalr(1)];
        bubble2=[-5 totalzb(i,:) -5 -5];
        fill(bubble1,bubble2,[255 230 153]./255,'linewidth',2)
        film1=[totalr(1) totalr fliplr(totalr)];
        film2=[totalzb(i,1) totalz(i,:) fliplr(totalzb(i,:))];
```

```
        fill(film1,film2,[143 170 220]./255,'linewidth',2)
        top1=[totalr totalr(end) totalr(1) totalr(1)];
        top2=[totalz(i,:) 1 1 totalz(i,1)];
        if strcmp(Itype,'GL')
            fill(top1,top2,'w','linewidth',2)
        else
            fill(top1,top2,[197 224 180]./255,'linewidth',2)
        end
    elseif strcmp(Itype,'SLL')
        clearpoints(an3a)
        clearpoints(an3b)
        addpoints(an3a,totalr,totalz(i,:))
        addpoints(an3b,totalr,totalzb(i,:))
        hold on
        bubble1=[totalr(1) totalr totalr(end) totalr(1)];
        bubble2=[-5 totalzb(i,:) -5 -5];
        fill(bubble1,bubble2,[255 230 153]./255,'linewidth',2)
        filmbot1=[totalr(1) totalr fliplr(totalr)];
        filmbot2=[totalzb(i,1) totalz(i,:) fliplr(totalzb(i,:))];
        fill(filmbot1,filmbot2,[143 170 220]./255,'linewidth',2)
        filmtop1=[totalr totalr(end) totalr(1) totalr(1)];
        filmtop2=[totalz(i,:) 0 0 totalz(i,1)];
        fill(filmtop1,filmtop2,[197 224 180]./255,'linewidth',2)
        fill([totalr(1) totalr(end) totalr(end) totalr(1)],...
            [0 0 1 1],[165 165 165]./255,'linewidth',2)
    else
        clearpoints(an3a)
        clearpoints(an3b)
        clearpoints(an3c)
        addpoints(an3a,totalr,totalz(i,:))
        addpoints(an3b,totalr,totalzb(i,:))
        addpoints(an3c,totalr,totalzS(i,:))
        hold on
        bubble1=[totalr(1) totalr totalr(end) totalr(1)];
        bubble2=[-5 totalzb(i,:) -5 -5];
        fill(bubble1,bubble2,[255 230 153]./255,'linewidth',2)
        filmbot1=[totalr(1) totalr fliplr(totalr)];
        filmbot2=[totalzb(i,1) totalz(i,:) fliplr(totalzb(i,:))];
        fill(filmbot1,filmbot2,[143 170 220]./255,'linewidth',2)
        filmtop1=[totalr(1) totalr fliplr(totalr)];
        filmtop2=[totalz(i,1) totalzS(i,:) fliplr(totalz(i,:))];
        fill(filmtop1,filmtop2,[197 224 180]./255,'linewidth',2)
        air1=[totalr totalr(end) totalr(1) totalr(1)];
        air2=[totalzS(i,:) 1 1 totalzS(i,1)];
        fill(air1,air2,'w','linewidth',2)
    end
    drawnow
    if strcmpi(save, 'yes')
        myMovie(framecount)=getframe(fig);
        framecount=framecount+1;
    end
end

if strcmpi(save, 'yes')
    % Get the name of the file that the user wants to save
    [baseFileName,folder]=uiputfile('*.avi','Specify a file');
    if baseFileName==0 % User clicked the Cancel button
```

```
        return;
    end
    fullFileName=fullfile(folder,baseFileName);
    % Create a video writer object with that file name.
    writerObj=VideoWriter(fullFileName,'Uncompressed AVI');
    open(writerObj);
    % Write out all the frames.
    numberOfFrames=length(myMovie);
    for frameNumber=1:numberOfFrames
       writeVideo(writerObj,myMovie(frameNumber));
    end
    close(writerObj);
end

end
```

### 7.3.3 Solid-Liquid Collision Function

```
function [t,X,V,h,p,zb,Fb,Fd,Fa,Ff]=SL(tspan,maxstep,r,dr,R,rho,...
    mu,sigma,g,H00,V0type)
% Travis S. Emery
% Solver for bubble collisions at a Solid-Liquid interface
% Find terminal velocity if needed
if strcmpi(V0type,"terminal")
    Vtfun=@(V) 4/3*pi*R^3*rho*g-getLothCdRe(rho*abs(V)*2*R/mu,...
        rho*V^2*2*R/sigma)*pi/4*mu*R*V;
    Vt=fzero(Vtfun,0.2); % terminal velocity
end
% Get coefficients for integration by Simpson's rule
SimpCoeff=getSimpCoeff(length(r));
% Initial conditions
h0=H00+r.^2/(2*R);
p0=zeros(size(r));
X0=H00+R;
if strcmpi(V0type,"terminal")
    V0=Vt;
    Fa0=0;
elseif strcmpi(V0type,"nonterminal")
    V0=0;
    Fa0=4/3*pi*R^3*rho*g;
end
Ff0=0;
Fd0=getLothCdRe(rho*abs(V0)*2*R/mu,rho*V0^2*2*R/sigma)*pi/4*mu*R*V0;
y0=[h0;p0;X0;V0;Ff0;Fd0;Fa0];
% Initial time derivatives
hp0=-V0*ones(size(r));
pp0=zeros(size(r));
Xp0=-V0;
if strcmpi(V0type,"terminal")
    Vp0=0;
elseif strcmpi(V0type,"nonterminal")
    phi0=(h0(1)+R)/R;
    Cm0=0.5+0.19222*phi0^-3.019+0.06214*phi0^-8.331+...
        0.0348*phi0^-24.65+0.0139*phi0^-120.7;
    Vp0=g/Cm0;
end
```

```
Ffp0=0;
Fdp0=0;
Fap0=0;
yp0=[hp0;pp0;Xp0;Vp0;Ffp0;Fdp0;Fap0];
% Set mass matrix
M=zeros(2*length(r)+5);
for j=1:length(r)
    M(j,j)=1; % dhdt
end
M(2*length(r)+1,2*length(r)+1)=1; % dXdt
M(2*length(r)+2,2*length(r)+2)=1; % dVdt
% Set absolute tolerances - [unit] tolerance
hAbsTol=1E-6*ones(size(r)); % [mm] 1 nm
pAbsTol=1E-11*ones(size(r)); % [GPa] 10 mPa
XAbsTol=1E-6; % [mm] 1 nm
VAbsTol=1E-6; % [m/s] 1 um/s
FAbsTol=1E-9*ones(3,1); % [kN] 1 uN
AbsTol=[hAbsTol;pAbsTol;XAbsTol;VAbsTol;FAbsTol];
% Set options
options=odeset('Mass',M,'InitialSlope',yp0,'MassSingular','yes',...
    'Events',@(t,y) eventfun(t,y,r),'Maxstep',maxstep,'AbsTol',AbsTol);
% Get consistent initial conditions if needed
implicitODE=@(t,y,yp) M*yp-fun(t,y,dr,R,r,rho,mu,sigma,g,SimpCoeff);
if sum(abs(implicitODE(tspan(1),y0,yp0))>AbsTol)>0
    [y0_new,yp0_new]=decic(implicitODE,tspan(1),y0,[],yp0,[],options);
    y0=y0_new;
    options=odeset(options,'InitialSlope',yp0_new);
end
% y is a system of ODEs such that y=[h;p;X;V;Ff;Fd;Fa]
[t,y]=ode15s(@(t,y) fun(t,y,dr,R,r,rho,mu,sigma,g,SimpCoeff),tspan,...
    y0,options);
h=y(:,1:length(r)); % film thickness
p=y(:,length(r)+1:2*length(r)); % film pressure
zb=-h; % bubble surface shape
X=y(:,2*length(r)+1); % bubble center trajectory
V=y(:,2*length(r)+2); % bubble center velocity
Ff=y(:,2*length(r)+3); % film force
Fd=y(:,2*length(r)+4); % drag force
Fa=y(:,2*length(r)+5); % added mass force
Fb=-4/3*pi*R^3*rho*g*ones(size(t)); % buoyancy force

function f=fun(~,y,dr,R,r,rho,mu,sigma,g,SimpCoeff)
    f=zeros(size(y));
    % Temporary variables for easier calculations
    htemp=y(1:length(r));
    ptemp=y(length(r)+1:2*length(r));
    Vtemp=y(2*length(r)+2);
    % Get spatial derivatives, all second order
    [dhdr,d2hdr2]=getDerivatives(htemp,dr);
    [dpdr,d2pdr2]=getDerivatives(ptemp,dr);
    % Get Cd and Cm
    CdRe=getLothCdRe(rho*abs(Vtemp)*2*R/mu,rho*Vtemp^2*2*R/sigma);
    phi=(htemp(1)+R)/R;
    Cm=0.5+0.19222*phi^-3.019+0.06214*phi^-8.331+0.0348*phi^-24.65...
        +0.0139*phi^-120.7;
    dCmdH=(-3.019*0.19222*phi^-4.019-8.331*0.06214*phi^-9.331-...
        24.65*0.0348*phi^-25.65-120.7*0.0139*phi^-121.7)/R;
```

```
    for i=1:length(f)
        if i==1 % dhdt at r=0
            f(i)=2*y(i)^3/(3*mu)*d2pdr2(i);
        elseif i>1 && i<length(r) % dhdt
            f(i)=y(i)^3/(3*mu*r(i))*dpdr(i)+y(i)^2/mu*dhdr(i)*...
                dpdr(i)+y(i)^3/(3*mu)*d2pdr2(i);
        elseif i==length(r) % dhdt at r=rm
            f(i)=-Vtemp;
        elseif i==length(r)+1 % dpdt at r=0
            f(i)=-y(i)+2*sigma/R-2*sigma*d2hdr2(i-length(r));
        elseif i>length(r)+1 && i<2*length(r) % dpdt
            f(i)=-y(i)+2*sigma/R-sigma/r(i-length(r))*...
                dhdr(i-length(r))-sigma*d2hdr2(i-length(r));
        elseif i==2*length(r) % dpdt at r=rm
            % Pressure decays as 1/r^4
            f(i)=4*y(i)+r(i-length(r))*dpdr(i-length(r));
            % Pressure is zero
%             f(i)=y(i);
        elseif i==2*length(r)+1 % dXdt
            f(i)=-Vtemp;
        elseif i==2*length(r)+2 % dVdt
            f(i)=(4/3*pi*R^3*rho*g-CdRe*pi/4*mu*R*y(i)+...
                2/3*pi*R^3*rho*dCmdH*y(i)^2-...
                2*pi*dr/3*sum(SimpCoeff.*r.*ptemp))/...
                (4/3*pi*R^3*rho*Cm);
        elseif i==2*length(r)+3 % dFfdt
            f(i)=y(i)-2*pi*dr/3*sum(SimpCoeff.*r.*ptemp);
        elseif i==2*length(r)+4 % dFddt
            f(i)=y(i)-CdRe*pi/4*mu*R*Vtemp;
        elseif i==2*length(r)+5 % dFadt
            f(i)=y(i)-4/3*pi*R^3*rho*Cm*f(2*length(r)+2)+...
                2/3*pi*R^3*rho*dCmdH*Vtemp^2;
        end
    end
end

function [value,isterminal,direction] = eventfun(~,y,r)
    % Stop solver if film thickness goes to zero
    value=min(y(1:length(r)));
    isterminal=1;
    direction=0;
end

end
```

### 7.3.4 Gas-Liquid Collision Function

```
function [t,X,V,h,p,zS,zb,Fb,Fd,Fa,Ff]=GL(tspan,maxstep,r,dr,R,rho,...
    mu,sigma,g,H00,V0type)
% Travis S. Emery
% Solver for bubble collisions at a Gas-Liquid interface
% Find terminal velocity if needed
if strcmpi(V0type,"terminal")
    Vtfun=@(V) 4/3*pi*R^3*rho*g-getLothCdRe(rho*abs(V)*2*R/mu,...
        rho*V^2*2*R/sigma)*pi/4*mu*R*V;
    Vt=fzero(Vtfun,0.2); % terminal velocity
```

```
end
% Get coefficients for integration by Simpson's rule
SimpCoeff=getSimpCoeff(length(r));
% Initial Conditions
h0=H00+r.^2/(2*R);
p0=zeros(size(r));
zS0=zeros(size(r));
X0=H00+R;
if strcmpi(V0type,"terminal")
    V0=Vt;
    Fa0=0;
elseif strcmpi(V0type,"nonterminal")
    V0=0;
    Fa0=4/3*pi*R^3*rho*g;
end
Ff0=0;
Fd0=getLothCdRe(rho*abs(V0)*2*R/mu,rho*V0^2*2*R/sigma)*pi/4*mu*R*V0;
y0=[h0;p0;zS0;X0;V0;Ff0;Fd0;Fa0];
% Initial time derivatives
hp0=-V0*ones(size(r));
pp0=zeros(size(r));
zSp0=zeros(size(r));
Xp0=-V0;
if strcmpi(V0type,"terminal")
    Vp0=0;
elseif strcmpi(V0type,"nonterminal")
    Vp0=2*g;
end
Ffp0=0;
Fdp0=0;
Fap0=0;
yp0=[hp0;pp0;zSp0;Xp0;Vp0;Ffp0;Fdp0;Fap0];
% Set mass matrix
M=zeros(3*length(r)+5);
for j=1:length(r)
    M(j,j)=1; % dhdt
end
M(length(r),3*length(r))=-1; % dhdt at r=rm
M(3*length(r)+1,3*length(r)+1)=1; % dXdt
M(3*length(r)+2,3*length(r)+2)=1; % dVdt
% Set absolute tolerances - [unit] tolerance
hAbsTol=1E-6*ones(size(r)); % [mm] 1 nm
pAbsTol=1E-11*ones(size(r)); % [GPa] 10 mPa
zSAbsTol=1E-6*ones(size(r)); % [mm] 1 nm
XAbsTol=1E-6; % [mm] 1 nm
VAbsTol=1E-6; % [m/s] 1 um/s
FAbsTol=1E-9*ones(3,1); % [kN] 1 uN
AbsTol=[hAbsTol;pAbsTol;zSAbsTol;XAbsTol;VAbsTol;FAbsTol];
% Set options
options=odeset('Mass',M,'InitialSlope',yp0,'MassSingular','yes',...
    'Events',@(t,y) eventfun(t,y,r),'Maxstep',maxstep,'AbsTol',AbsTol);
% Get consistent initial conditions if needed
implicitODE=@(t,y,yp) M*yp-fun(t,y,dr,R,r,rho,mu,sigma,g,SimpCoeff);
if sum(abs(implicitODE(tspan(1),y0,yp0))>AbsTol)>0
    [y0_new,yp0_new]=decic(implicitODE,tspan(1),y0,[],yp0,[],options);
    y0=y0_new;
    options=odeset(options,'InitialSlope',yp0_new);
```

```
end
% y is a system of ODEs s.t. y=[h;p;zS;X;V;Ff;Fd;Fa]
[t,y]=ode15s(@(t,y) fun(t,y,dr,R,r,rho,mu,sigma,g,SimpCoeff),...
    tspan,y0,options);
h=y(:,1:length(r)); % film thickness
p=y(:,length(r)+1:2*length(r)); % film pressure
zS=y(:,2*length(r)+1:3*length(r)); % interface shape
zb=zS-h; % bubble surface shape
X=y(:,3*length(r)+1); % bubble center trajectory
V=y(:,3*length(r)+2); % bubble center velocity
Ff=y(:,3*length(r)+3); % film force
Fd=y(:,3*length(r)+4); % drag force
Fa=y(:,3*length(r)+5); % added mass force
Fb=-4/3*pi*R^3*rho*g*ones(size(t)); % buoyancy force

function f=fun(~,y,dr,R,r,rho,mu,sigma,g,SimpCoeff)
    f=zeros(size(y));
    % Temporary variables for easier calculations
    htemp=y(1:length(r));
    ptemp=y(length(r)+1:2*length(r));
    zStemp=y(2*length(r)+1:3*length(r));
    Vtemp=y(3*length(r)+2);
    % Get spatial derivatives, all second order
    [dhdr,d2hdr2]=getDerivatives(htemp,dr);
    [dpdr,d2pdr2]=getDerivatives(ptemp,dr);
    [dzSdr,d2zSdr2]=getDerivatives(zStemp,dr);
    % Get Cd and Cm
    CdRe=getLothCdRe(rho*abs(Vtemp)*2*R/mu,rho*Vtemp^2*2*R/sigma);
    Cm=0.5;
    for i = 1:length(f)
        if i==1 % dhdt at r=0
            f(i)=2*y(i)^3/(3*mu)*d2pdr2(i);
        elseif i>1 && i<length(r) % dhdt
            f(i)=y(i)^3/(3*mu*r(i))*dpdr(i)+y(i)^2/mu*dhdr(i)*...
                dpdr(i)+y(i)^3/(3*mu)*d2pdr2(i);
        elseif i==length(r) % dhdt at r=rm
            f(i)=-Vtemp;
        elseif i==length(r)+1 % dpdt at r=0
            f(i)=-y(i)+sigma/R+rho*g*zStemp(i-length(r))/2-...
                sigma*d2hdr2(i-length(r));
        elseif i>length(r)+1 && i<2*length(r) % dpdt
            f(i)=-y(i)+sigma/R+rho*g*zStemp(i-length(r))/2-...
                sigma/(2*r(i-length(r)))*dhdr(i-length(r))-...
                sigma/2*d2hdr2(i-length(r));
        elseif i==2*length(r) % dpdt at r=rm
            f(i)=y(i);
        elseif i==2*length(r)+1 % dzdt at r=0
            f(i)=rho*g*y(i)-ptemp(i-2*length(r))-...
                2*sigma*d2zSdr2(i-2*length(r));
        elseif i>2*length(r)+1 && i<3*length(r) % dzdt
            f(i)=rho*g*y(i)-ptemp(i-2*length(r))-...
                sigma/r(i-2*length(r))*dzSdr(i-2*length(r))-...
                sigma*d2zSdr2(i-2*length(r));
        elseif i==3*length(r) % dzdt at r=rm
            f(i)=y(i)-y(3*length(r)+3)/(2*pi*sigma)*...
                besselk(0,r(end)/sqrt(sigma/(rho*g)));
        elseif i==3*length(r)+1 % dXdt
```

```
            f(i)=-Vtemp;
        elseif i==3*length(r)+2 % dVdt
            f(i)=(4/3*pi*R^3*rho*g-CdRe*pi/4*mu*R*y(i)-...
                2*pi*dr/3*sum(SimpCoeff.*r.*ptemp))/...
                (4/3*pi*R^3*rho*Cm);
        elseif i==3*length(r)+3 % dFfdt
            f(i)=y(i)-2*pi*dr/3*sum(SimpCoeff.*r.*ptemp);
        elseif i==3*length(r)+4 % dFddt
            f(i)=y(i)-CdRe*pi/4*mu*R*Vtemp;
        elseif i==3*length(r)+5 % dFadt
            f(i)=y(i)-4/3*pi*R^3*rho*Cm*f(3*length(r)+2);
        end
    end
end

function [value,isterminal,direction] = eventfun(~,y,r)
    % Stop solver if film thickness goes to zero
    value=min(y(1:length(r)));
    isterminal=1;
    direction=0;
end

end
```

### 7.3.5 *Liquid-Liquid Collision Function*

```
function [t,X,V,h,p,tauv,zI,zb,Fb,Fd,Fa,Ff]=LL(tspan,maxstep,r,dr,R...
    ,rhob,mub,sigmab,rhot,mut,sigmai,sigmabar,g,H00,V0type,Cm)
% Travis S. Emery
% Solver for bubble collisions at a Liquid-Liquid interface
% Find terminal velocity if needed
if strcmpi(V0type,"terminal")
    Vtfun=@(V) 4/3*pi*R^3*rhob*g-getLothCdRe(rhob*abs(V)*2*R/mub,...
        rhob*V^2*2*R/sigmab)*pi/4*mub*R*V;
    Vt=fzero(Vtfun,0.2); % terminal velocity
end
% Get coefficients for integration by Simpson's rule
SimpCoeff=getSimpCoeff(length(r));
% Initial Conditions
h0=H00+r.^2/(2*R);
p0=zeros(size(r));
zI0=zeros(size(r));
tauv0=zeros(size(r));
X0=H00+R;
if strcmpi(V0type,"terminal")
    V0=Vt;
    Fa0=0;
elseif strcmpi(V0type,"nonterminal")
    V0=0;
    Fa0=4/3*pi*R^3*rhob*g;
end
Ff0=0;
Fd0=getLothCdRe(rhob*abs(V0)*2*R/mub,rhob*V0^2*2*R/sigmab)*...
    pi/4*mub*R*V0;
y0=[h0;p0;zI0;tauv0;X0;V0;Ff0;Fd0;Fa0];
% Initial time derivatives
```

```
hp0=-V0*ones(size(r));
pp0=zeros(size(r));
zIp0=zeros(size(r));
tauvp0=zeros(size(r));
Xp0=-V0;
if strcmpi(V0type,"terminal")
    Vp0=0;
elseif strcmpi(V0type,"nonterminal")
    Vp0=2*g;
end
Ffp0=0;
Fdp0=0;
Fap0=0;
yp0=[hp0;pp0;zIp0;tauvp0;Xp0;Vp0;Ffp0;Fdp0;Fap0];
% Set absolute tolerances - [unit] tolerance
hAbsTol=1E-6*ones(size(r)); % [mm] 1 nm
pAbsTol=1E-11*ones(size(r)); % [GPa] 10 mPa
zIAbsTol=1E-6*ones(size(r)); % [mm] 1 nm
tauvAbsTol=1E-11*ones(size(r)); % [GPa] 10 mPa
XAbsTol=1E-6; % [mm] 1 nm
VAbsTol=1E-6; % [m/s] 1 um/s
FAbsTol=1E-9*ones(3,1); % [kN] 1 uN
AbsTol=[hAbsTol;pAbsTol;zIAbsTol;tauvAbsTol;XAbsTol;VAbsTol;FAbsTol];
% Set options
options=odeset('Mass',@(t,y) mass(t,y,r,dr,rhob,rhot,mut,sigmai,...
    sigmabar,g),'InitialSlope',yp0,'MassSingular','yes',...
    'MStateDependence','strong','Events',@(t,y) eventfun(t,y,r),...
    'Maxstep',maxstep,'AbsTol',AbsTol);
% Get consistent initial conditions if needed
implicitODE=@(t,y,yp) mass(t,y,r,dr,rhob,rhot,mut,sigmai,sigmabar,g)...
    *yp-fun(t,y,dr,R,r,rhob,mub,sigmab,rhot,sigmai,sigmabar,...
    g,SimpCoeff,Cm);
if sum(abs(implicitODE(tspan(1),y0,yp0))>AbsTol)>0
    [y0_new,yp0_new]=decic(implicitODE,tspan(1),y0,[],yp0,[],options);
    y0=y0_new;
    options=odeset(options,'InitialSlope',yp0_new);
end
% y is a system of ODEs s.t. y=[h;p;zI;tauv;X;V;Ff;Fd;Fa;Fi]
[t,y]=ode15s(@(t,y) fun(t,y,dr,R,r,rhob,mub,sigmab,rhot,sigmai,...
    sigmabar,g,SimpCoeff,Cm),tspan,y0,options);
h=y(:,1:length(r)); % film thickness
p=y(:,length(r)+1:2*length(r)); % film pressure
zI=y(:,2*length(r)+1:3*length(r)); % interface shape
zb=zI-h; % bubble surface shape
tauv=y(:,3*length(r)+1:4*length(r)); % viscous stress
X=y(:,4*length(r)+1); % bubble center trajectory
V=y(:,4*length(r)+2); % bubble center velocity
Ff=y(:,4*length(r)+3); % film force
Fd=y(:,4*length(r)+4); % drage force
Fa=y(:,4*length(r)+5); % added mass force
Fb=-4/3*pi*R^3*rhob*g*ones(size(t)); % buoyancy force

function f=fun(~,y,dr,R,r,rhob,mub,sigmab,rhot,sigmai,sigmabar...
        ,g,SimpCoeff,Cm)
    f=zeros(size(y));
    % Temporary variables for easier calculations
    htemp=y(1:length(r));
```

```
    ptemp=y(length(r)+1:2*length(r));
    zItemp=y(2*length(r)+1:3*length(r));
    tauvtemp=y(3*length(r)+1:4*length(r));
    Vtemp=y(4*length(r)+2);
    % Get spatial derivatives, all second order
    [dhdr,d2hdr2]=getDerivatives(htemp,dr);
    [dpdr,d2pdr2]=getDerivatives(ptemp,dr);
    [dzIdr,d2zIdr2]=getDerivatives(zItemp,dr);
    % Get Cd
    CdRe=getLothCdRe(rhob*abs(Vtemp)*2*R/mub,rhob*Vtemp^2*2*R/sigmab);
    for i = 1:length(f)
        if i==1 % dhdt at r=0
            f(i)=2*y(i)^3/(3*mub)*d2pdr2(i);
        elseif i>1 && i<length(r) % dhdt
            f(i)=y(i)^3/(3*mub*r(i))*dpdr(i)+y(i)^2/mub*dhdr(i)*...
                dpdr(i)+y(i)^3/(3*mub)*d2pdr2(i);
        elseif i==length(r) % dhdt at r=rm
            f(i)=-Vtemp;
        elseif i==length(r)+1 % dpdt at r=0
            f(i)=-y(i)+2*sigmabar/R+sigmabar/sigmai*(rhob-rhot)*...
                g*zItemp(i-length(r))-2*sigmabar*d2hdr2(i-length(r));
        elseif i>length(r)+1 && i<2*length(r) % dpdt
            f(i)=-y(i)+2*sigmabar/R+sigmabar/sigmai*(rhob-rhot)*...
                g*zItemp(i-length(r))-sigmabar/r(i-length(r))*...
                dhdr(i-length(r))-sigmabar*d2hdr2(i-length(r));
        elseif i==2*length(r) % dpdt at r=rm
            f(i)=y(i);
        elseif i==2*length(r)+1 % dzIdt at r=0
            f(i)=(rhob-rhot)*g*y(i)-ptemp(i-2*length(r))-...
                2*sigmai*d2zIdr2(i-2*length(r));
        elseif i>2*length(r)+1 && i<3*length(r) % dzdt
            f(i)=(rhob-rhot)*g*y(i)-ptemp(i-2*length(r))-...
                sigmai/r(i-2*length(r))*dzIdr(i-2*length(r))-...
                sigmai*d2zIdr2(i-2*length(r));
        elseif i==3*length(r) % dzIdt at r=rm
            f(i)=y(i)-dr/3*sum(SimpCoeff.*r.*(ptemp-tauvtemp))/...
                sigmai*besselk(0,r(end)/sqrt(sigmai/((rhob-rhot)*g)));
        elseif i>=3*length(r)+1 && i<=4*length(r) % dtauvdt
            f(i)=y(i);
        elseif i==4*length(r)+1 % dXdt
            f(i)=-Vtemp;
        elseif i==4*length(r)+2 % dVdt
            f(i)=(4/3*pi*R^3*rhob*g-CdRe*pi/4*mub*R*y(i)-...
                2*pi*dr/3*sum(SimpCoeff.*r.*ptemp))/...
                (4/3*pi*R^3*rhob*Cm);
        elseif i==4*length(r)+3 % dFfdt
            f(i)=y(i)-2*pi*dr/3*sum(SimpCoeff.*r.*ptemp);
        elseif i==4*length(r)+4 % dFddt
            f(i)=y(i)-CdRe*pi/4*mub*R*Vtemp;
        elseif i==4*length(r)+5 % dFadt
            f(i)=y(i)-4/3*pi*R^3*rhob*Cm*f(4*length(r)+2);
        end
    end
end

function M = mass(~,y,r,dr,rhob,rhot,mut,sigmai,sigmabar,g)
    % Set tauv coefficient, tauv=4*mut*abs(d2zIdr2)*dzIdt
```

```
    zItemp=y(2*length(r)+1:3*length(r));
    [~,d2zIdr2]=getDerivatives(zItemp,dr);
    tauvcoeff=4*mut*abs(d2zIdr2);
    % Mass matrix function
    M=zeros(length(y));
    for j=1:length(y)
        if j>=1 && j<length(r) % dhdt
            M(j,j)=1;
        elseif j==length(r) % dhdt at r=rm
            M(j,j)=1;
            M(j,j+2*length(r))=-1;
        elseif j>=length(r)+1 && j<2*length(r) % dpdt
            M(j,j+length(r))=-sigmabar/sigmai*tauvcoeff(j-length(r));
        elseif j==2*length(r) % dpdt at r=rm
            M(j,j)=0;
        elseif j>=2*length(r)+1 && j<3*length(r) % dzIdt
            M(j,j)=-tauvcoeff(j-2*length(r));
        elseif j==3*length(r) % dzIdt at r=rm
            M(j,j)=-tauvcoeff(j-2*length(r))/((rhob-rhot)*g);
        elseif j>=3*length(r)+1 && j<=4*length(r) % dtauvdt
            M(j,j-length(r))=tauvcoeff(j-3*length(r));
        elseif j==4*length(r)+1 % dXdt
            M(j,j)=1;
        elseif j==4*length(r)+2 % dVdt
            M(j,j)=1;
        elseif j==4*length(r)+3 % dFfdt
            M(j,j)=0;
        elseif j==4*length(r)+4 % dFddt
            M(j,j)=0;
        elseif j==4*length(r)+5 % dFadt
            M(j,j)=0;
        end
    end
end

function [value,isterminal,direction]=eventfun(~,y,r)
    % Stop solver if film thickness goes to zero
    value=min(y(1:length(r)));
    isterminal=1;
    direction=0;
end

end
```

### *7.3.6 Solid-Liquid-Liquid Collision Function*

```
function
[t,X,V,h1,h2,p1,p2,tauv,zI,zb,Fb,Fd,Fa,Ff]=SLL(tspan,maxstep,...
    r,dr,R,rhob,mub,sigmab,rhot,mut,sigmai,sigmabar,g,H10,H200,...
    V0type,Cm)
% Travis S. Emery
% Solver for bubble collisions at a Solid-Liquid-Liquid interface
% Find terminal velocity if needed
if strcmpi(V0type,"terminal")
    Vtfun=@(V) 4/3*pi*R^3*rhob*g-getLothCdRe(rhob*abs(V)*2*R/mub,...
        rhob*V^2*2*R/sigmab)*pi/4*mub*R*V;
```

```
    Vt=fzero(Vtfun,0.2); % terminal velocity
end
% Get coefficients for integration by Simpson's rule
SimpCoeff=getSimpCoeff(length(r));
% Initial Conditions
h10=H10*ones(size(r));
h20=H200+r.^2/(2*R);
p10=zeros(size(r));
p20=zeros(size(r));
tauv0=zeros(size(r));
X0=H10+H200+R;
if strcmpi(V0type,"terminal")
    V0=Vt;
    Fa0=0;
elseif strcmpi(V0type,"nonterminal")
    V0=0;
    Fa0=4/3*pi*R^3*rhob*g;
end
Ff0=0;
Fd0=getLothCdRe(rhob*abs(V0)*2*R/mub,rhob*V0^2*2*R/sigmab)*...
    pi/4*mub*R*V0;
y0=[h10;h20;p10;p20;tauv0;X0;V0;Ff0;Fd0;Fa0];
% Initial time derivatives
h1p0=zeros(size(r));
h2p0=-V0*ones(size(r));
p1p0=zeros(size(r));
p2p0=zeros(size(r));
tauvp0=zeros(size(r));
Xp0=-V0;
if strcmpi(V0type,"terminal")
    Vp0=0;
elseif strcmpi(V0type,"nonterminal")
    phi0=(h10(1)+h20(1)+R)/R;
    Cm0=Cm+0.19222*phi0^-3.019+0.06214*phi0^-8.331+0.0348*...
        phi0^-24.65+0.0139*phi0^-120.7;
    Vp0=g/Cm0;
end
Ffp0=0;
Fdp0=0;
Fap0=0;
yp0=[h1p0;h2p0;p1p0;p2p0;tauvp0;Xp0;Vp0;Ffp0;Fdp0;Fap0];
% Set absolute tolerances - [unit] tolerance
hAbsTol=1E-6*ones(2*length(r),1); % [mm] 1 nm
pAbsTol=1E-11*ones(2*length(r),1); % [GPa] 10 mPa
tauvAbsTol=1E-11*ones(length(r),1); % [GPa] 10 mPa
XAbsTol=1E-6; % [mm] 1 nm
VAbsTol=1E-6; % [m/s] 1 um/s
FAbsTol=1E-9*ones(3,1); % [kN] 1 uN
AbsTol=[hAbsTol;pAbsTol;tauvAbsTol;XAbsTol;VAbsTol;FAbsTol];
% Set options and get consistent initial conditions
options=odeset('Mass',@(t,y) mass(t,y,r,dr,rhob,rhot,mut,sigmai,...
    sigmabar,g),'InitialSlope',yp0,'MassSingular','yes','Events',...
    @(t,y) eventfun(t,y,r),'MaxStep',maxstep,'AbsTol',AbsTol);
% Get consistent initial conditions if needed
implicitODE=@(t,y,yp) mass(t,y,r,dr,rhob,rhot,mut,sigmai,sigmabar,g)...
    *yp-fun(t,y,R,dr,r,rhob,mub,sigmab,rhot,mut,sigmabar,sigmai,g,...
    H10,SimpCoeff,Cm);
```

```
if sum(abs(implicitODE(tspan(1),y0,yp0))>AbsTol)>0
    [y0_new,yp0_new]=decic(implicitODE,tspan(1),y0,[],yp0,[],options);
    y0=y0_new;
    options=odeset(options,'InitialSlope',yp0_new);
end
% y is a system of ODEs s.t. y=[h1;h2;p1;p2;tauv;X;V;Ff;Fd;Fa]
[t,y]=ode15s(@(t,y)
fun(t,y,R,dr,r,rhob,mub,sigmab,rhot,mut,sigmabar,...
    sigmai,g,H10,SimpCoeff,Cm),tspan,y0,options);
h1=y(:,1:length(r)); % top film thickness
h2=y(:,length(r)+1:2*length(r)); % bottom film thickness
zI=-h1; % interface shape
zb=zI-h2; % bubble surface shape
p1=y(:,2*length(r)+1:3*length(r)); % top film pressure
p2=y(:,3*length(r)+1:4*length(r)); % bottom film pressure
tauv=y(:,1+4*length(r):5*length(r)); % viscous stress
X=y(:,5*length(r)+1);  % bubble center trajectory
V=y(:,5*length(r)+2);  % bubble center velocity
Ff=y(:,5*length(r)+3); % film force
Fd=y(:,5*length(r)+4); % drag force
Fa=y(:,5*length(r)+5); % added mass force
Fb=-4/3*pi*R^3*rhob*g*ones(length(t),1); % buoyancy force

function f=fun(~,y,R,dr,r,rhob,mub,sigmab,rhot,mut,sigmabar,sigmai,...
        g,H10,SimpCoeff,Cm)
    f=zeros(length(y),1);
    % Temporary variables for easier calculations
    h1temp=y(1:length(r));
    h2temp=y(length(r)+1:2*length(r));
    p1temp=y(2*length(r)+1:3*length(r));
    p2temp=y(3*length(r)+1:4*length(r));
    tauvtemp=y(4*length(r)+1:5*length(r));
    Vtemp=y(5*length(r)+2);
    % Get spatial derivatives, all second order
    [dh1dr,d2h1dr2]=getDerivatives(h1temp,dr);
    [dp1dr,d2p1dr2]=getDerivatives(p1temp,dr);
    [dh2dr,d2h2dr2]=getDerivatives(h2temp,dr);
    [dp2dr,d2p2dr2]=getDerivatives(p2temp,dr);
    % Get Cd and Cm
    CdRe=getLothCdRe(rhob*abs(Vtemp)*2*R/mub,rhob*Vtemp^2*2*R/sigmab);
    phi=(h1temp(1)+h2temp(1)+R)/R;
    Cmeff=Cm+0.19222*phi^-3.019+0.06214*phi^-8.331+0.0348*phi^-24.65...
        +0.0139*phi^-120.7;
    dCmdH=(-3.019*0.19222*phi^-4.019-8.331*0.06214*phi^-9.331-...
        24.65*0.0348*phi^-25.65-120.7*0.0139*phi^-121.7)/R;
    for i=1:length(f)
        if i==1 % dh1dt at r=0
            f(i)=y(i)^3/(6*mut)*d2p1dr2(i);
        elseif i>1&&i<length(r) % dh1dt
            f(i)=y(i)^3/(12*mut*r(i))*dp1dr(i)+y(i)^2/(4*mut)*...
                dh1dr(i)*dp1dr(i)+y(i)^3/(12*mut)*d2p1dr2(i);
        elseif i==length(r) % dh1dt at r=rm
            f(i)=-y(i)+H10-dr/3*sum(SimpCoeff.*r.*(p2temp-p1temp-...
                tauvtemp))/sigmai*besselk(0,r(end)/sqrt(sigmai/...
                ((rhob-rhot)*g)));
        elseif i==length(r)+1 % dh2dt at r=0
            f(i)=2*y(i)^3/(3*mub)*d2p2dr2(i-length(r));
```

```
        elseif i>length(r)+1 && i<2*length(r) % dh2dt
            f(i)=y(i)^3/(3*mub*r(i-length(r)))*dp2dr(i-length(r))+...
                y(i)^2/mub*dh2dr(i-length(r))*dp2dr(i-length(r))+...
                y(i)^3/(3*mub)*d2p2dr2(i-length(r));
        elseif i==2*length(r) % dh2dt at r=rm
            f(i)=-Vtemp;
        elseif i==2*length(r)+1 % dp1dt at r=0
            f(i)=-y(i)+p2temp(i-2*length(r))-(rhob-rhot)*g*(H10-...
                h1temp(i-2*length(r)))-2*sigmai*d2h1dr2(i-2*length(r));
        elseif i>2*length(r)+1 && i<3*length(r) % dp1dt
            f(i)=-y(i)+p2temp(i-2*length(r))-(rhob-rhot)*g*(H10-...
                h1temp(i-2*length(r)))-sigmai/r(i-2*length(r))*...
                dh1dr(i-2*length(r))-sigmai*d2h1dr2(i-2*length(r));
        elseif i==3*length(r) % dp1dt at r=rm
            f(i)=y(i);
        elseif i==3*length(r)+1 % dp2dt at r=0
            f(i)=-y(i)+sigmabar/sigmai*p1temp(i-3*length(r))+...
                2*sigmabar/R+sigmabar/sigmai*(rhob-rhot)*g*(H10-...
                h1temp(i-3*length(r)))-2*sigmabar*...
                d2h2dr2(i-3*length(r));
        elseif i>3*length(r)+1 && i<4*length(r) % dp2dt
            f(i)=-y(i)+sigmabar/sigmai*p1temp(i-3*length(r))+...
                2*sigmabar/R+sigmabar/sigmai*(rhob-rhot)*g*(H10-...
                h1temp(i-3*length(r)))-sigmabar/r(i-3*length(r))*...
                dh2dr(i-3*length(r))-sigmabar*d2h2dr2(i-3*length(r));
        elseif i==4*length(r) % dp2dt at r=rm
            f(i)=y(i);
        elseif i>=4*length(r)+1 && i<=5*length(r) % dtauvdt
            f(i)=y(i);
        elseif i==5*length(r)+1 % dXdt
            f(i)=-Vtemp;
        elseif i==5*length(r)+2 % dVdt
            f(i)=(4/3*pi*R^3*rhob*g-CdRe*pi/4*mub*R*y(i)+...
                2/3*pi*R^3*rhob*dCmdH*y(i)^2-2*pi*dr/3*...
                sum(SimpCoeff.*r.*p2temp))/(4/3*pi*R^3*rhob*Cmeff);
        elseif i==5*length(r)+3 % dFfdt
            f(i)=y(i)-2*pi*dr/3*sum(SimpCoeff.*r.*p2temp);
        elseif i==5*length(r)+4 % dFddt
            f(i)=y(i)-CdRe*pi/4*mub*R*Vtemp;
        elseif i==5*length(r)+5 % dFadt
            f(i)=y(i)-4/3*pi*R^3*rhob*Cmeff*f(5*length(r)+2)+...
                2/3*pi*R^3*rhob*dCmdH*Vtemp^2;
        end
    end
end

function M = mass(~,y,r,dr,rhob,rhot,mut,sigmai,sigmabar,g)
    % Set tauv coefficient, tauv=-4*mut*abs(d2h1dr2)*dh1dt
    h1temp=y(1:length(r));
    [~,d2h1dr2]=getDerivatives(h1temp,dr);
    tauvcoeff=-4*mut*abs(d2h1dr2);
    % Set mass matrix
    M=zeros(length(y));
    for j=1:length(y)
        if j>=1 && j<length(r) % dh1dt
            M(j,j)=1;
        elseif j==length(r) % dh1dt at r=rm
```

```
            M(j,j)=-tauvcoeff(j)/((rhob-rhot)*g);
        elseif j>=length(r)+1 && j<2*length(r) % dh2dt
            M(j,j)=1;
        elseif j==2*length(r) % dh2dt at r=rm
            M(j,j)=1;
            M(j,j-length(r))=1;
        elseif j>=2*length(r)+1 && j<3*length(r) % p1dt
            M(j,j-2*length(r))=tauvcoeff(j-2*length(r));
        elseif j==3*length(r) % dp1dt at r=rm
            M(j,j)=0;
        elseif j>=3*length(r)+1 && j<4*length(r) % p2dt
            M(j,j-3*length(r))=-sigmabar/sigmai*...
                tauvcoeff(j-3*length(r));
        elseif j==4*length(r) % dp2dt at r=rm
            M(j,j)=0;
        elseif j>=4*length(r)+1 && j<=5*length(r) % dtauvdt
            M(j,j-4*length(r))=tauvcoeff(j-4*length(r));
        elseif j==5*length(r)+1 % dXdt
            M(j,j)=1;
        elseif j==5*length(r)+2 % dVdt
            M(j,j)=1;
        elseif j==5*length(r)+3 % dFfdt
            M(j,j)=0;
        elseif j==5*length(r)+4 % dFddt
            M(j,j)=0;
        elseif j==5*length(r)+5 % dFadt
            M(j,j)=0;
        end
    end
end

function [value,isterminal,direction] = eventfun(~,y,r)
    % Stop solver if film thickness goes to zero
    value=min(y(1:2*length(r)));
    isterminal = 1;
    direction = 0;
end

end
```

### 7.3.7 Gas-Liquid-Liquid Collision Function

```
function [t,X,V,h1,h2,p1,p2,tauv,zI,zb,zS,Fb,Fd,Fa,Ff]=GLL(tspan,...
    maxstep,r,dr,R,rhob,mub,sigmab,rhot,mut,sigmat,sigmai,sigmabar,...
    sigmaprime,g,H10,H200,V0type,Cm)
% Travis S. Emery
% Solver for bubble collisions at a Gas-Liquid-Liquid interface
% Find terminal velocity if needed and set aspect ratio
if strcmpi(V0type,"terminal")
    Vtfun=@(V) 4/3*pi*R^3*rhob*g-getLothCdRe(rhob*abs(V)*2*R/mub,...
        rhob*V^2*2*R/sigmab)*pi/4*mub*R*V;
    Vt=fzero(Vtfun,0.2); % terminal velocity
end
% Get coefficients for integration by Simpson's rule
SimpCoeff=getSimpCoeff(length(r));
% Initial Conditions
```

```
h10=H10*ones(size(r));
h20=H200+r.^2/(2*R);
p10=zeros(size(r));
p20=zeros(size(r));
zS0=zeros(size(r));
tauv0=zeros(size(r));
X0=H10+H200+R;
if strcmpi(V0type,"terminal")
    V0=Vt;
    Fa0=0;
elseif strcmpi(V0type,"nonterminal")
    V0=0;
    Fa0=4/3*pi*R^3*rhob*g;
end
Ff0=0;
Fd0=getLothCdRe(rhob*abs(V0)*2*R/mub,rhob*V0^2*2*R/sigmab)*...
    pi/4*mub*R*V0;
y0=[h10;h20;p10;p20;zS0;tauv0;X0;V0;Ff0;Fd0;Fa0];
% Initial time derivatives
h1p0=zeros(size(r));
h2p0=-V0*ones(size(r));
p1p0=zeros(size(r));
p2p0=zeros(size(r));
zSp0=zeros(size(r));
tauvp0=zeros(size(r));
Xp0=-V0;
if strcmpi(V0type,"terminal")
    Vp0=0;
elseif strcmpi(V0type,"nonterminal")
    Vp0=2*g;
end
Ffp0=0;
Fdp0=0;
Fap0=0;
yp0=[h1p0;h2p0;p1p0;p2p0;zSp0;tauvp0;Xp0;Vp0;Ffp0;Fdp0;Fap0];
% Set absolute tolerances - [unit] tolerance
hAbsTol=1E-6*ones(2*length(r),1); % [mm] 1 nm
pAbsTol=1E-11*ones(2*length(r),1); % [GPa] 10 mPa
zSAbsTol=1E-6*ones(size(r)); % [mm] 1 nm
tauvAbsTol=1E-11*ones(length(r),1); % [GPa] 10 mPa
XAbsTol=1E-6; % [mm] 1 nm
VAbsTol=1E-6; % [m/s] 1 um/s
FAbsTol=1E-9*ones(3,1); % [kN] 1 uN
AbsTol=[hAbsTol;pAbsTol;zSAbsTol;tauvAbsTol;XAbsTol;VAbsTol;FAbsTol];
% Set options
options=odeset('Mass',@(t,y) mass(t,y,r,dr,rhob,rhot,mut,sigmai,...
    sigmaprime,sigmabar,g,H10),'InitialSlope',yp0,'MassSingular',...
    'yes','MStateDependence','strong','Events',...
    @(t,y) eventfun(t,y,r),'MaxStep',maxstep,'AbsTol',AbsTol);
% Get consistent initial conditions if needed
implicitODE=@(t,y,yp) mass(t,y,r,dr,rhob,rhot,mut,sigmai,sigmaprime,...
    sigmabar,g,H10)*yp-
fun(t,y,R,dr,r,rhob,mub,sigmab,rhot,mut,sigmat,...
    sigmai,sigmabar,sigmaprime,g,H10,SimpCoeff,Cm);
if sum(abs(implicitODE(tspan(1),y0,yp0))>AbsTol)>0
    [y0_new,yp0_new]=decic(implicitODE,tspan(1),y0,[],yp0,[],options);
    y0=y0_new;
```

```
    options=odeset(options,'InitialSlope',yp0_new);
end
% y is a system of ODEs s.t. y=[h1;h2;p1;p2;zS;tauv;X;V;Ff;Fd;Fa]
[t,y]=ode15s(@(t,y) fun(t,y,R,dr,r,rhob,mub,sigmab,rhot,mut,sigmat,...
    sigmai,sigmabar,sigmaprime,g,H10,SimpCoeff,Cm),tspan,y0,options);
h1=y(:,1:length(r)); % top film thickness
h2=y(:,length(r)+1:2*length(r)); % bottom film thickness
p1=y(:,2*length(r)+1:3*length(r)); % top film pressure
p2=y(:,3*length(r)+1:4*length(r)); % bottom film pressure
zS=y(:,4*length(r)+1:5*length(r)); % surface shape
zI=zS-h1; % interface shape
zb=zI-h2; % bubble surface shape
tauv=y(:,5*length(r)+1:6*length(r)); % viscous stress
X=y(:,6*length(r)+1);  % bubble center trajectory
V=y(:,6*length(r)+2);  % bubble center velocity
Ff=y(:,6*length(r)+3); % film force
Fd=y(:,6*length(r)+4); % drag force
Fa=y(:,6*length(r)+5); % added mass force
Fb=-4/3*pi*R^3*rhob*g*ones(length(t),1); % buoyancy force

function f=fun(~,y,R,dr,r,rhob,mub,sigmab,rhot,mut,sigmat,sigmai,...
        sigmabar,sigmaprime,g,H10,SimpCoeff,Cm)
    f=zeros(size(y));
    % Temporary variables for easier calculations
    h1temp=y(1:length(r));
    h2temp=y(length(r)+1:2*length(r));
    p1temp=y(2*length(r)+1:3*length(r));
    p2temp=y(3*length(r)+1:4*length(r));
    zStemp=y(4*length(r)+1:5*length(r));
    tauvtemp=y(5*length(r)+1:6*length(r));
    Vtemp=y(6*length(r)+2);
    % Get spatial derivatives, all second order
    [dh1dr,d2h1dr2]=getDerivatives(h1temp,dr);
    [dp1dr,d2p1dr2]=getDerivatives(p1temp,dr);
    [dh2dr,d2h2dr2]=getDerivatives(h2temp,dr);
    [dp2dr,d2p2dr2]=getDerivatives(p2temp,dr);
    [dzSdr,d2zSdr2]=getDerivatives(zStemp,dr);
    % Get Cd and Cm
    CdRe=getLothCdRe(rhob*abs(Vtemp)*2*R/mub,rhob*Vtemp^2*2*R/sigmab);
    for i = 1:length(f)
        if i==1 % dh1dt at r=0
            f(i)=2*y(i)^3/(3*mut)*d2p1dr2(i);
        elseif i>1 && i<length(r) % dh1dt
            f(i)=y(i)^3/(3*mut*r(i))*dp1dr(i)+y(i)^2/(mut)*...
                dh1dr(i)*dp1dr(i)+y(i)^3/(3*mut)*d2p1dr2(i);
        elseif i==length(r) % dh1dt at r=rm
            f(i)=-y(i)+H10+dr/3*sum(SimpCoeff.*r.*p1temp)/sigmat...
                *besselk(0,r(end)/sqrt(sigmat/(rhot*g)))-...
                dr/3*sum(SimpCoeff.*r.*(p2temp-p1temp-tauvtemp))/...
                sigmai*besselk(0,r(end)/sqrt(sigmai/((rhob-rhot)*g)));
        elseif i==length(r)+1 % dh2dt at r=0
            f(i)=2*y(i)^3/(3*mub)*d2p2dr2(i-length(r));
        elseif i>length(r)+1 && i<2*length(r) % dh2dt
            f(i)=y(i)^3/(3*mub*r(i-length(r)))*dp2dr(i-length(r))+...
                y(i)^2/mub*dh2dr(i-length(r))*dp2dr(i-length(r))+...
                y(i)^3/(3*mub)*d2p2dr2(i-length(r));
        elseif i==2*length(r) % dh2dt at r=rm
```

```
            f(i)=-Vtemp;
        elseif i==2*length(r)+1 % dp1dt at r=0
            f(i)=-y(i)+sigmaprime/sigmai*p2temp(i-2*length(r))+...
                sigmaprime/sigmat*rhot*g*zStemp(i-2*length(r))-...
                sigmaprime/sigmai*(rhob-rhot)*g*(H10+...
                zStemp(i-2*length(r))-h1temp(i-2*length(r)))-...
                2*sigmaprime*d2h1dr2(i-2*length(r));
        elseif i>2*length(r)+1 && i<3*length(r) % dp1dt
            f(i)=-y(i)+sigmaprime/sigmai*p2temp(i-2*length(r))+...
                sigmaprime/sigmat*rhot*g*zStemp(i-2*length(r))-...
                sigmaprime/sigmai*(rhob-rhot)*g*(H10+...
                zStemp(i-2*length(r))-h1temp(i-2*length(r)))-...
                sigmaprime/r(i-2*length(r))*dh1dr(i-2*length(r))-...
                sigmaprime*d2h1dr2(i-2*length(r));
        elseif i==3*length(r) % dp1dt at r=rm
            f(i)=y(i);
        elseif i==3*length(r)+1 % dp2dt at r=0
            f(i)=-y(i)+sigmabar/sigmai*p1temp(i-3*length(r))+...
                2*sigmabar/R+sigmabar/sigmai*(rhob-rhot)*g*(H10+...
                zStemp(i-3*length(r))-h1temp(i-3*length(r)))-...
                2*sigmabar*d2h2dr2(i-3*length(r));
        elseif i>3*length(r)+1 && i<4*length(r) % dp2dt
            f(i)=-y(i)+sigmabar/sigmai*p1temp(i-3*length(r))+...
                2*sigmabar/R+sigmabar/sigmai*(rhob-rhot)*g*(H10+...
                zStemp(i-3*length(r))-h1temp(i-3*length(r)))-...
                sigmabar/r(i-3*length(r))*dh2dr(i-3*length(r))-...
                sigmabar*d2h2dr2(i-3*length(r));
        elseif i==4*length(r) % dp2dt at r=rm
            f(i)=y(i);
        elseif i==4*length(r)+1 % dzSdt at r=0
            f(i)=rhot*g*y(i)-p1temp(i-4*length(r))-...
                2*sigmat*d2zSdr2(i-4*length(r));
        elseif i>4*length(r)+1 && i<5*length(r) % dzSdt
            f(i)=rhot*g*y(i)-p1temp(i-4*length(r))-...
                sigmat/r(i-4*length(r))*dzSdr(i-4*length(r))-...
                sigmat*d2zSdr2(i-4*length(r));
        elseif i==5*length(r) % dzSdt at r=rm
            f(i)=y(i)-dr/3*sum(SimpCoeff.*r.*p1temp)/sigmat*...
                besselk(0,r(end)/sqrt(sigmat/(rhot*g)));
        elseif i>=5*length(r)+1 && i<=6*length(r) % dtauvdt
            f(i)=y(i);
        elseif i==6*length(r)+1 % dXdt
            f(i)=-Vtemp;
        elseif i==6*length(r)+2 % dVdt
            f(i)=(4/3*pi*R^3*rhob*g-CdRe*pi/4*mub*R*y(i)-...
                2*pi*dr/3*sum(SimpCoeff.*r.*p2temp))/...
                (4/3*pi*R^3*rhob*Cm);
        elseif i==6*length(r)+3 % dFfdt
            f(i)=y(i)-2*pi*dr/3*sum(SimpCoeff.*r.*p2temp);
        elseif i==6*length(r)+4 % dFddt
            f(i)=y(i)-CdRe*pi/4*mub*R*Vtemp;
        elseif i==6*length(r)+5 % dFadt
            f(i)=y(i)-4/3*pi*R^3*rhob*Cm*f(6*length(r)+2);
        end
    end
end
```

```
function M = mass(~,y,r,dr,rhob,rhot,mut,sigmai,sigmaprime,...
        sigmabar,g,H10)
    % Set tauv coefficient, tauv=-4*mut*abs(d2zIdr2)*dh1dt
    zItemp=H10+y(4*length(r)+1:5*length(r))-y(1:length(r));
    [~,d2zIdr2]=getDerivatives(zItemp,dr);
    tauvcoeff=-4*mut*abs(d2zIdr2);
    % Set mass matrix
    M=zeros(length(y));
    for j=1:length(y)
        if j>=1 && j<length(r) % dh1dt
            M(j,j)=1;
        elseif j==length(r) % dh1dt at r=rm
            M(j,j)=-tauvcoeff(j)/((rhob-rhot)*g);
        elseif j>=length(r)+1 && j<2*length(r) % dh2dt
            M(j,j)=1;
        elseif j==2*length(r) % dh2dt at r=rm
            M(j,j)=1;
            M(j,j+3*length(r))=-1;
            M(j,j-length(r))=1;
        elseif j>=2*length(r)+1 && j<3*length(r) % p1dt
            M(j,j-2*length(r))=sigmaprime/sigmai*...
                tauvcoeff(j-2*length(r));
        elseif j==3*length(r) % dp1dt at r=rm
            M(j,j)=0;
        elseif j>=3*length(r)+1 && j<4*length(r) % p2dt
            M(j,j-3*length(r))=-sigmabar/sigmai*...
                tauvcoeff(j-3*length(r));
        elseif j==4*length(r) % dp2dt at r=rm
            M(j,j)=0;
        elseif j>=4*length(r)+1 && j<=5*length(r) % dzSdt
            M(j,j)=0;
        elseif j>=5*length(r)+1 && j<=6*length(r) % dtauvdt
            M(j,j-5*length(r))=tauvcoeff(j-5*length(r));
        elseif j==6*length(r)+1 % dXdt
            M(j,j)=1;
        elseif j==6*length(r)+2 % dVdt
            M(j,j)=1;
        elseif j==6*length(r)+3 % dFfdt
            M(j,j)=0;
        elseif j==6*length(r)+4 % dFddt
            M(j,j)=0;
        elseif j==6*length(r)+5 % dFadt
            M(j,j)=0;
        end
    end
end

function [value,isterminal,direction] = eventfun(~,y,r)
    % Stop solver if film thickness goes to zero
    value=min(y(1:2*length(r)));
    isterminal = 1;
    direction = 0;
end

end
```

### 7.3.8 Drag Coefficient Function

```
function CdRe=getLothCdRe(Re,We)
% Travis S. Emery
% Determines drag coefficient for a clean bubble based on Reynolds and
% Weber number
% Based on Loth, 2008, Quasi-Steady Shape and Drag of
% Deformable Bubbles and Drops
if Re==0
    CdRe=0;
else
    f=2/3+(12./Re+0.75*(1+3.315./sqrt(Re))).^-1;
    CdWe0=24*f./Re;
    CdWeInf=8/3+16./Re;
    if Re<100
        Cd=tanh(0.021*We.^1.6).*(CdWeInf-CdWe0)+CdWe0;
    else
        if We<3
            Emin=0.25+0.55*exp(-0.09*Re);
            cE=0.165+0.55*exp(-0.3*Re);
            E=1-(1-Emin).*tanh(cE.*We);
            XLoth=1./E;
            K=0.0195*XLoth.^4-0.2134*XLoth.^3+1.7026*XLoth.^2-...
                2.1461*XLoth-1.5732;
            G=1/3*XLoth.^(4/3).*(XLoth.^2-1).^1.5.*...
                (sqrt(XLoth.^2-1)-(2-XLoth.^2).*asec(XLoth))./...
                (XLoth.^2.*asec(XLoth)-sqrt(XLoth.^2-1)).^2;
            Cd=48./Re.*G.*(1+K./sqrt(Re));
        elseif We>5
            Cd=(2.5*tanh(0.2*We)-1.5).*(CdWeInf-CdWe0)+CdWe0;
        else
            Emin=0.25+0.55*exp(-0.09*Re);
            cE=0.165+0.55*exp(-0.3*Re);
            E=1-(1-Emin).*tanh(cE.*We);
            XLoth=1./E;
            K=0.0195*XLoth.^4-0.2134*XLoth.^3+1.7026*XLoth.^2-...
                2.1461*XLoth-1.5732;
            G=1/3*XLoth.^(4/3).*(XLoth.^2-1).^1.5.*...
                (sqrt(XLoth.^2-1)-(2-XLoth.^2).*asec(XLoth))./...
                (XLoth.^2.*asec(XLoth)-sqrt(XLoth.^2-1)).^2;
            CdMoore=48./Re.*G.*(1+K./sqrt(Re));
            CdSep=(2.5*tanh(0.2*We)-1.5).*(CdWeInf-CdWe0)+CdWe0;
            Cd=max(CdMoore,CdSep);
        end
    end
    CdRe=Cd.*Re;
end
end
```

### 7.3.9 Derivative Function

```
function [dydx,d2ydx2]=getDerivatives(y,dx)
% Travis S. Emery
% Function to get derivatives using second order finite difference
% scheme using central or backwards differences
% Assumes axisymmetric at y(1) which enables use of central difference
```

```
% scheme at this location for second derivatice
dydx=zeros(length(y),1);
d2ydx2=zeros(length(y),1);
for i=1:length(y)
    if i==1
        dydx(i)=0;
        d2ydx2(i)=(-2*y(i)+2*y(i+1))/dx^2;
    elseif i==length(y)
        dydx(i)=(3/2*y(i)-2*y(i-1)+1/2*y(i-2))/dx;
        d2ydx2(i)=(2*y(i)-5*y(i-1)+4*y(i-2)-y(i-3))/dx^2;
    else
        dydx(i)=(-y(i-1)+y(i+1))/(2*dx);
        d2ydx2(i)=(y(i-1)-2*y(i)+y(i+1))/dx^2;
    end
end
end
```

### *7.3.10 Integration Coefficient Function*

```
function SimpCoeff=getSimpCoeff(n)
% Travis S. Emery
% Function to get coefficeints used for integration by Simpson's rule
% Standard form only works for odd n, combine with Simpson's 3/8 rule
% for even n
SimpCoeff=ones(n,1);
if mod(n,2)~=0
    for k=2:n-1
        if mod(k,2)==0
            SimpCoeff(k)=4;
        else
            SimpCoeff(k)=2;
        end
    end
else
    for k=2:n-4
        if mod(k,2)==0
            SimpCoeff(k)=4;
        else
            SimpCoeff(k)=2;
        end
    end
    SimpCoeff(end-3)=17/8;
    SimpCoeff(end-2)=27/8;
    SimpCoeff(end-1)=27/8;
    SimpCoeff(end)=9/8;
end
end
```